Charge correlations in quantum simulation of mixed-dimensional Hubbard systems

Dominik Bourgund

München 2024

Charge correlations in quantum simulation of mixed-dimensional Hubbard systems

Dominik Bourgund

Dissertation
an der Fakultät für Physik
der Ludwig–Maximilians–Universität
München

vorgelegt von
DOMINIK BOURGUND
aus Landsberg (Lech)

München, den 12.03.2024

Erstgutachter: Prof. Dr. Immanuel Bloch
Zweitgutachter: Prof. Dr. Christian Groß
Tag der mündlichen Prüfung: 23.04.2024

Zusammenfassung

Stark korrelierte Systeme, insbesondere im Zusammenhang mit Hochtemperatursupraleitung, stellen eine Herausforderung sowohl für theoretische als auch experimentelle Studien dar. Mit der Entstehung des Felds der Quantensimulation sind neue Werkzeuge zur präzisen Untersuchung quantenmechanischer Systeme entstanden. Ultrakalte Atome in optischen Gittern bilden eine herausragende Plattform für Studien solch stark korrelierter Phänomene mittels des minimalen Fermi-Hubbard Modells. Ausgehend von einem antiferromagnetisch geordneten Zustand wird vermutet, dass das komplexe Zusammenspiel zwischen Spin- und Ladungsfreiheitsgraden in dotierten Systemen im Mittelpunkt kollektiver Effekte wie gepaarter Fermionen steht. Allerdings ist im Moment der Konsens, dass der Grundzustand des einfachen Fermi-Hubbard Modells nicht supraleitend ist, sondern stattdessen eine Ladungsdichtewelle bildet, die als Streifenphase bezeichnet wird.

In dieser Arbeit nutzen wir einen hochauflösenden Quantensimulator mit ultrakalten Fermionen, um die Bildung von Streifen im Fermi-Hubbard-Modell zu untersuchen. Unter normalen Bedingungen liegen die Temperaturskalen für Streifenphasen weit unter dem derzeitigen Stand der Technik für Quantensimulatoren. Daher wählen wir eine spezifische Konfiguration, bei der Tunnelkopplungen nur entlang einer Richtung vorhanden sind, während der Spin-Austausch entlang beider Richtungen erfolgt, was die Temperatur, bei der Streifen beginnen aufzutreten, auf etwa die Spinwechselwirkungsenergie erhöht. Mittels der Spin- und Dichteauflösung bis zu einzelnen Gitterplätzen messen wir ausgedehnte, fluktuierende Ladungsstrukturen, die auf die Anwesenheit eines Streifens hindeuten. Darüber hinaus sind Signaturen im Spinsektor konsistent mit lokalen antiferromagnetischen Domänen, die über Streifen hinweg ihr Vorzeichen ändern.

Um auf dieses Kopplungsregime zugreifen zu können, haben wir ein neues, hochstabiles optisches Übergitter entworfen, implementiert und charakterisiert. Durch die Kombination eines bichromatischen Ansatzes mit verbesserter Entkopplung von der Umgebung mittels Evakuierung und spezifischen Materialien erreichen wir eine herausragende Phasenstabilität. Zusätzlich wird eine schnelle und breite Abstimmbarkeit der relativen Übergitterphase via zweier komplementärer Methoden erzielt. Wir charakterisieren den Aufbau mittels Ein- und Zwei-Teilchen-Quantenspaziergängen, Rabi-Oszillationen sowie Spin-Korrelationen.

Mit diesen Verbesserungen haben wir die Grundlagen für weitere Studien zu Details der Streifenphase sowie anderer exotischer Tieftemperaturphasen des Fermi-Hubbard-Modells gelegt. Neben der Relevanz für die Quantensimulation stellt dies außerdem einen Schritt hin zu einer zukünftigen fermionischen Quantencomputer-Architektur dar.

Abstract

The complex nature of strongly correlated materials, as the high-temperature superconducting cuprates, has proven to be a challenge in both theoretical and experimental studies for decades. With the advent of quantum simulation, new tools have emerged for the investigation of quantum systems on a microscopic level. Ultracold atoms confined in optical lattices offer an excellent platform for exploring strongly correlated phenomena in the minimal Fermi-Hubbard model. Starting from an antiferromagnetically ordered state, the intricate interplay between spin and charge degrees of freedoms in doped systems is supposed to be at the centre of collective effects such as paired states. Nevertheless, the ground state of the plain Fermi-Hubbard model is currently suspected to not be superconducting, instead favouring the formation of a charge density wave known as a stripe phase.

In this thesis, we leverage the capabilities of a quantum simulator with ultracold fermions to investigate the formation of stripes in the Fermi-Hubbard model. Under normal conditions, the temperature scales associated with stripe phases fall well beyond the limits of current state-of-the-art quantum simulators. Therefore, we adopt a specific mixed-dimensional setting, where tunnel couplings are restricted to one direction, while spin exchange coupling persists along both, thereby elevating the onset temperature of stripes to approximately the superexchange energy. Using single-site spin and charge resolution, we observe extended, fluctuating charge structures in the system, indicative of the presence of stripes. Moreover, signatures in the spin sector are consistent with local antiferromagnetic domains that change sign across stripes.

To access this mixed-dimensional regime, we designed, implemented and characterised a novel, highly-stable optical superlattice. By combining a bichromatic approach and enhanced environmental decoupling via evacuation and utilising appropriate materials, we achieve cutting-edge phase stability. Furthermore, we attain fast and wide tunability of the relative superlattice phase using two complementary methods. We characterise the setup using single and two-particle quantum walks, Rabi oscillations as well as spin correlations.

These results establish the groundwork for further investigations into the nuances of the stripe phase and other exotic low-temperature phases of the Fermi-Hubbard model. Finally, beyond its implications for quantum simulation, this endeavour signifies a stride towards a future fermionic quantum computing platform.

Contents

1 Introduction **1**

2 Quantum simulation of the Hubbard model in optical lattices **7**
2.1 Quantum simulation and quantum gas microscopy 7
2.2 Fermi-Hubbard model 9
2.2.1 Definition and properties 9
2.2.2 Simplified models: $t - J$ and Heisenberg Hamiltonian 10
2.2.3 Fermi-Hubbard phase diagram 11
2.3 Optical lattice potentials 12
2.4 Experimental setup 16
2.4.1 Properties of ^{6}Li 16
2.4.2 Preparation of ultracold samples 17
2.4.3 Spin-resolved, single-site detection 21
2.5 Topological phases in fermionic ladders 25

3 Design and characterisation of high-stability optical superlattices **29**
3.1 Optical lattice geometries and realisations 29
3.1.1 Static optical lattices 29
3.1.2 Tunable optical lattices 30
3.2 Requirements on optical superlattices 32
3.3 Bichromatic superlattice design 34
3.3.1 General features 34
3.3.2 Optical design 36
3.3.3 Mechanical design 39
3.3.4 Tunability 43
3.4 Characterisation 47
3.4.1 Preparation and temperature 47
3.4.2 Stability 48
3.4.3 Quantum walks 53
3.4.4 Double-well Rabi oscillations 59
3.4.5 Engineering Fermi-Hubbard couplings in ladder systems 64
3.5 Summary 66

4 Signatures of stripe formation in a mixed-dimensional system **69**
4.1 Stripe phases in context . . . 69
4.1.1 Low-temperature phases of the doped Fermi-Hubbard model . 69
4.1.2 Stripe phase definition and signatures . . . 71
4.1.3 Stripes and superconductivity . . . 76
4.1.4 Perspective from quantum simulation with ultracold atoms . . 77
4.2 Charge order in mixed-dimensional systems . . . 79
4.2.1 Theoretical mixD studies . . . 80
4.2.2 Experimental studies . . . 81
4.3 Preparation of mixD systems . . . 82
4.3.1 Model and parameter regime . . . 82
4.3.2 Lattice ramps . . . 85
4.3.3 Calibration . . . 86
4.4 Results in the charge sector . . . 89
4.4.1 Correlation functions . . . 89
4.4.2 Hole-hole correlations . . . 90
4.4.3 Multi-point charge correlations . . . 94
4.4.4 Stripe identification . . . 96
4.5 Results in the spin sector . . . 100
4.5.1 Spin-charge correlations . . . 100
4.5.2 String correlators . . . 102
4.6 Discussion . . . 104

5 Conclusion **107**

Bibliography **109**

Acknowledgments **136**

Chapter 1

Introduction

Computational capabilities have undergone remarkable improvements over the past decades, yet they remain constrained by the underlying physical principles of classical computing. The emergence of quantum computation has ignited hope for the development of a uniquely powerful platform capable of providing vastly enhanced computational power [1–4]. While theoretical advantages have been established, potentially promising exponential speed-ups in computations [5, 6], the practical implementation has encountered formidable technical challenges [7]. Various approaches leveraging trapped ions [8–10], superconducting circuits [11–14], quantum dots [15–18], photons [19–21] or nitrogen-vacancy centres [22] have been developed but struggle to attain the qubit numbers and gate fidelities necessary for full, error-corrected computations [23]. Despite recent progress [21, 24, 25] pushing towards the so-called noisy, intermediate-scale quantum (NISQ) regime [26] where quantum computers could provide advantages over classical computers, applications to non-tailored questions remain pending [27].

One particular problem exceeding the capabilities of classical computers concerns the study of strongly-correlated many-body quantum systems [28]. Numerically addressing such problems poses significant challenges due to the poorly scaling Hilbert space and the intrinsic sign problem for fermionic particles [29]. Meanwhile, conventional studies in solid-state physics encounter limitations regarding accessible parameter ranges, preparation fidelity and available observables in detection [30]. Although universal quantum computers currently remain out of reach [26], *quantum simulation* has emerged as a promising complementary approach [31, 32]. Rooted in Feynman's concept of simulating a complex quantum system in a more manageable manner [33], implementations utilising ultracold atoms have proven to be a potent tool for investigating a broad spectrum of otherwise elusive problems [31, 34]. Upon laser cooling atoms down close to absolute zero [35–38], quantum properties of atoms start to dominate. Consequently, Bose-Einstein condensates [39–41] and degenerate Fermi gases [42] have been realised early on. Advancements in cooling and trapping techniques [43, 44] have facilitated the study of atoms arranged in precise manners using optical lattices or tweezers [36, 45–47]. This high level of control enables the exploration of a wide range of parameter regimes that are otherwise experimentally

inaccessible. However, many – especially fermionic – systems are so far still limited in terms of their system size and temperature range. Nonetheless, experiments have demonstrated the realisation of Bose- [48] and Fermi-Hubbard models [49–51] and explored, for instance, artificial gauge fields [52, 53] and thermalisation [54, 55].

Studies in ultracold atoms have access to unique sets of observables. While initially limited to momentum space and low-resolution real space measurements, nowadays, single-site resolved imaging techniques in quantum gas microscopes [56] allow for the calculation of arbitrary real-space correlation functions, in contrast to conventional material investigations. These correlators play a pivotal role in enhancing the microscopic understanding of various physical phenomena. For example, site-resolved studies have delved into Mott insulators in bosonic [57–59] and fermionic [60–63] systems. Additionally, fermionic investigations have explored antiferromagnetic correlations [64, 65], spin and charge structure factors [64, 66], spectroscopic signatures [67], transport properties [68, 69], Pauli blocking [60, 70] and fermionic pairing [71, 72] among numerous other aspects.

The phase diagram of the cuprates has eluded a full microscopic understanding despite extensive studies since the groundbreaking discovery of unconventional superconductivity by Bednorz and Müller [73]. Emerging from an antiferromagnetically ordered undoped state, the precise relationship to other doped phases continues to be a subject of active inquiry [74]. Pseudogap phenomena observed at intermediate doping levels [75], characterised by a suppression of spectral weight in certain parts of the Fermi surface [76], may be related to precursors of collective effects at lower temperatures [77]. Similarly, anomalous, strange metallic transport properties – where resistivity increases linearly with temperature – eludes full theoretical understanding [78, 79]. The Fermi-Hubbard model [80], serving as a possible minimal theory, captures numerous features observed in cuprates, suggesting that studies of this model could shed light onto the fundamental elements contributing to the emergence of collective phases. Current numerical findings suggest that the optimally doped ground state may not be superconducting [81], but instead host a *stripe phase* [82, 83], potentially competing with the emergence of superconductivity [84]. This phase is characterised by micro-phase separation where dopants line up to minimise their overall impact on the antiferromagnetic spin background [74]. While both phases have been separately established in materials [30] as well as numerical [85, 86] studies, their complex relationship is numerically challenging to unravel due to small energy gaps and possible finite size effects [87]. Meanwhile, in direct studies on cuprates, differing ground states in only marginally varying materials complicate the resolution to this challenging problem [30].

In this work, we use a state-of-the-art quantum simulator with fermionic ^{6}Li to investigate the low-temperature phases of the Fermi-Hubbard model. Equipped with

single-site spin and density resolution capabilities, we are able to calculate any high-order correlators of real-space spin and charge operators. Via potential shaping to redistribute entropy from the main system to a metallic reservoir, we prepare systems at temperatures down to $0.25\,t$, consistent with the lowest temperatures achieved in Fermi-Hubbard quantum simulators to date. We implemented a new set of high-stability, bichromatic superlattices, which can be leveraged both for quantum simulation purposes, as well as opening up access to new perspectives in quantum computation. The phase stability of the lattices is characterised and shown to be, to our knowledge, the highest realised for superlattices so far. In this thesis, our primary focus lies in leveraging these superlattices to prepare mixed-dimensional quantum systems, which have drastically increased temperature scales for collective phases compared to conventional two-dimensional systems. Thereby, we are able to access the regime of hole-hole attraction and for the first time observe initial indications of extended stripe formation in such systems. Through the application of multi-point charge and spin correlators, we manage to identify aspects of stripe phases in our data. With further improvements in temperature, full studies of collective phenomena and pseudogap physics may be approached, improving the microscopic understanding of high-temperature superconducting materials.

Outline

This thesis describes the progress in understanding low-temperature phases of the Fermi-Hubbard model using ultracold atoms with a quantum gas microscope. It is structured as follows:

In Chapter 2, an overview of the physical principles underlying this thesis as well as the overall experimental setup are presented. The basics of the Fermi-Hubbard model and how optical lattices can be used to simulate it using ultracold atoms are discussed. The procedure to prepare an ultracold atomic sample of ^{6}Li in a single plane of three-dimensional optical lattice is detailed, and the unique single-site and spin resolved detection method is explained. We briefly discuss one application in the study of the topological Haldane phase in Fermi-Hubbard ladders.

In Chapter 3, we describe the new high-stability optical superlattice setup that was designed and implemented in the course of this thesis. Different superlattice geometries are discussed and the advantages of a bichromatic approach shown. The detailed optical and mechanical design of the new lattices are described and then characterised using single-particle and many-body methods.

The main result of this thesis is shown in Chapter 4, where we focus on the low-temperature stripe phase of the Fermi-Hubbard model. A review of the phase diagram of the Fermi-Hubbard model is given with a specific focus on stripe phases and unconventional superconductivity. It is then shown how engineered mixed-dimensional systems can provide a new pathway to increase critical temperatures for the emergence of bound dopants in antiferromagnets. Our superlattices allowed for the realisation of a mixed-dimensional system that is used to study the formation of stripe order. Using multi-point correlators, numerous pieces of evidence are provided for the presence of stripes in both charge and spin sector.

Publication list

The following papers were submitted and published in the course of this PhD thesis.

- **Optical superlattice for engineering Hubbard couplings in quantum simulation.**
  T. Chalopin, P. Bojović, D. Bourgund, S. Wang, T. Franz, I. Bloch and T. A. Hilker.
  arXiv.2405.19322 (2024).

- **Formation of stripes in a mixed-dimensional cold-atom Fermi-Hubbard system.**
  D. Bourgund, T. Chalopin, P. Bojović, H. Schlömer, S. Wang, T. Franz, S. Hirthe, A. Bohrdt, F. Grusdt, I. Bloch and T. A. Hilker.
  arXiv.2312.14156 (2023).

- **Magnetically mediated hole pairing in fermionic ladders of ultracold atoms.**
  S. Hirthe, T. Chalopin, D. Bourgund, P. Bojović, A. Bohrdt, E. Demler, F. Grusdt, I. Bloch and T. A. Hilker.
  Nature 613, 463-467 (2023).

- **Realizing the symmetry-protected Haldane phase in Fermi-Hubbard ladders.**
  P. Sompet*, S. Hirthe*, D. Bourgund*, T. Chalopin, J. Bibo, J. Koepsell, P. Bojović, R. Verresen, F. Pollmann, G. Salomon, C. Gross, T. A. Hilker and I. Bloch.
  Nature 606, 484-488 (2022).
  * These authors contributed equally.

- **Microscopic evolution of doped Mott insulators from polaronic metal to Fermi liquid.**
  J. Koepsell, D. Bourgund, P. Sompet, S. Hirthe, A. Bohrdt, Y. Wang, F. Grusdt, E. Demler, G. Salomon, C. Gross and I. Bloch.
  Science 374, 6563 (2021).

- **Robust bilayer charge pumping for spin- and density-resolved quantum gas microscopy.**
  J. Koepsell, S. Hirthe, D. Bourgund, P. Sompet, J. Vijayan, G. Salomon, C. Gross and I. Bloch.
  Physical Review Letters 125, 010403 (2020).

Chapter 2

Quantum simulation of the Hubbard model in optical lattices

In this chapter, we give an overview of the basics of quantum simulation, specifically the Fermi-Hubbard model as well as optical lattices. Furthermore, we describe the experimental setup at the centre of this thesis with more details on specific elements added in the following chapter.

2.1 Quantum simulation and quantum gas microscopy

Quantum simulation promises to solve fundamental questions in solid-state physics. Investigating quantum phenomena in materials is usually not limited by the available energy scales but instead suffers from difficult preparation, material-specific properties as well as limited detection capabilities [30]. By cooling neutral atoms to close to absolute zero temperature, quantum systems can be prepared with a high degree of precision and control over model parameters. Thereby, in analog quantum simulation of Hubbard models with neutral atoms, a correspondence between electrons in a solid state material to atoms in an optical lattice is established [47, 88–91]. The energy scales in materials are much higher due to the atomic spacing on the order of few ångström [92] compared to lattice spacings around $0.5 - 1\,\mu m$ in quantum simulation [88, 93]. This severely changes the temperatures necessary to reveal quantum effects and study order in the system, making it directly accessible for ultracold quantum gases. One example is the Néel temperature (see section 2.2.3), which can be as high as several hundred kelvin in materials [94], while for ultracold atoms it is usually on the order of few nK [95]. This emphasises the need for efficient cooling techniques relying on laser cooling and evaporative cooling. Meanwhile, one major difference to real materials remains as, for the most part, no phonons are included in cold atom simulators. However, a wide range of models can be realised using arbitrary potential shaping, optical lattice with varying geometries [59, 96–98], as well as the implementation of real and artificial fields [53]. Furthermore, the increased length scales allow for superior resolution useful for both addressing and detection.

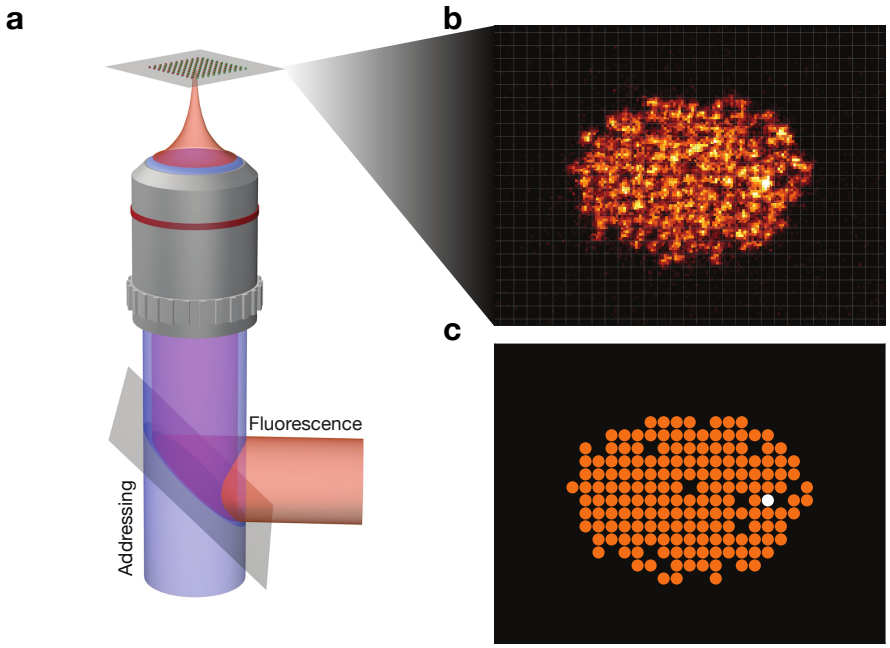

Figure 2.1: Quantum gas microscopy. **a**, Using a high-NA objective, single-site readout and addressing is achievable. The resulting atomic distribution obtained through fluorescence imaging is shown in **b**, from which the occupation as shown in **c** can be reconstructed using deconvolution techniques.

With the development of quantum gas microscopy [56, 99, 100], single-site readout and manipulation became invaluable tools in quantum simulation (see Fig. 2.1). Using high-NA microscope objectives, the fluorescence emitted from single planes (or bilayer systems [101, 102]) is captured on a camera and allows for the reconstruction of the occupation on individual lattices. By employing optical pushout [103, 104] or Stern-Gerlach techniques [65, 105], this can be extended to additionally achieve microscopic spin resolution, which reveals the pseudospin on each site as well. The microscopic resolution expands the available observables to real-space measurements and high-order correlation functions [66, 106–111] while retaining the high degree of control over model parameters. As the detection occurs via projective measurements, many realisations of the same experiment are necessary to extract correlation functions or reconstruct key features of the quantum state. This requires sufficient long-term stability of the experiments due to the slow repetition rates currently achievable. While a majority of experiments require more than 20 s for a single realisation [60, 100], more recent setups managed to reduce this to few seconds [112, 113]. Using these techniques, a continuously growing number of bosonic [113–121] and fermionic [60–63, 68, 98, 122] quantum gas microscopes has been demonstrated.

2.2 Fermi-Hubbard model

With the lack of exact microscopic models to describe low-temperature phases in strongly correlated materials, minimal models are essential for numerical studies as well as experimental investigations in ultracold atoms. The Fermi-Hubbard model is such a toy model, reducing the complex structure of real materials to spinful fermions moving on a lattice. It simplifies the non-local, multi-orbital, multi-layered physics of solid-states to a basic, single-orbital model, which nevertheless manages to encompass many of the properties of actual materials.

2.2.1 Definition and properties

The behaviour of strongly correlated electrons in solid state materials can be approximated by the Fermi-Hubbard model [80, 123, 124]. It describes fermions in a periodic lattice potential and is in its simplest form defined as

$$\hat{\mathcal{H}}_{FH} = -\sum_{\langle i,j\rangle,\sigma} t_{ij}\left(\hat{c}^{\dagger}_{i,\sigma}\hat{c}_{j,\sigma} + \text{h.c.}\right) + \sum_{i,\sigma\neq\sigma'} U_{\sigma,\sigma'}\hat{n}_{i,\sigma}\hat{n}_{i,\sigma'} + \sum_{i,\sigma}\Delta_{i,\sigma}\hat{n}_{i,\sigma}. \tag{2.1}$$

where $\hat{c}^{\dagger}_{i,\sigma}$ ($\hat{c}_{i,\sigma}$) is the creation (annihilation) operator for a fermion on site i with spin σ. The on-site number operator is then defined as $\hat{n}_{i,\sigma} = \hat{c}^{\dagger}_{i,\sigma}\hat{c}_{i,\sigma}$. The model parameters are the tunnel coupling t_{ij} between sites at position i and j, the on-site interactions between fermions in different spin states $U_{\sigma,\sigma'}$, and the on-site potential $\Delta_{i,\sigma}$ (which we will neglect for most of the following discussion) (see Fig. 2.2). The first term represents the kinetic energy of the fermions, making delocalisation favourable. Depending on the parameters, this can be opposed by their interactions. For our purpose, we will restrict our discussion to the spin-1/2 Hubbard model due to its connection to electrons in solid state materials. We note that this model does

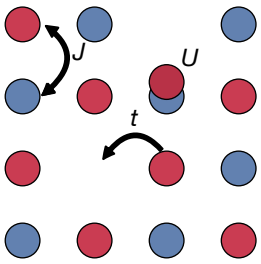

Figure 2.2: Fermi-Hubbard model. Spin-1/2 fermions in a lattice potential with spin up (red) and down (blue) are shown with tunnel coupling t, interaction energy U and superexchange coupling J.

not include any long-range interactions, such as Coulomb-type interactions, but only relies on on-site contact interactions. Due to screening effects, this is often a good approximation, but there is still an ongoing discussion whether beyond on-site interactions are relevant for low-temperature phases [125]. Furthermore, we only consider short-ranged tunnel coupling and usually restrict ourselves to nearest-neighbour, or in some cases next-nearest-neighbour hopping. Finally, the effect of higher-bands is neglected, which vastly simplifies the model.

The Fermi-Hubbard model hosts several important symmetries that map different parameters spaces onto each other. In addition to the trivial symmetries of spatial translation and parity, there is a global spin $SU(2)$ symmetry due to the spin isotropy, as well as a global $U(1)$ symmetry due to particle number conservation. More interesting to consider is the particle-hole symmetry. For a transformation of $\hat{c}_{i,\sigma} \rightarrow \eta_i \hat{c}^\dagger_{i,\sigma}$ with $\eta = \pm 1$, we find that the repulsive and attractive side of the phase diagram are mapped onto each other [126]. This explains the symmetry of the phase diagram at half-filling as seen in Fig. 2.3. Away from half-filling for $U > 0$, this leads to a spin-imbalanced system for $U < 0$. By making use of this symmetry, studies on either attractive or repulsive models (depending on which side may be easier to approach experimentally) can yield insights relevant for the whole phase diagram. We note that this symmetry only holds for bipartite lattices. Therefore, next-nearest-neighbour (diagonal) hopping terms break this symmetry [127].

2.2.2 Simplified models: $t - J$ and Heisenberg Hamiltonian

In the limit of strong interactions $U/t \gg 1$, we can expand the Fermi-Hubbard model in orders of t/U up to second order for [128]

$$\begin{aligned}\hat{\mathcal{H}} = &- \sum_{\langle i,j\rangle,\sigma=\uparrow,\downarrow} \hat{\mathcal{P}} \left(t_{ij} \hat{c}^\dagger_{i,\sigma} \hat{c}_{j,\sigma} + \text{h.c.} \right) \hat{\mathcal{P}} + \sum_{\langle i,j\rangle} J_{ij} \left(\hat{\mathbf{S}}_i \cdot \hat{\mathbf{S}}_j - \frac{\hat{n}_i \hat{n}_j}{4} \right) \\ &- \sum_{i,j,k}^{i\neq k} \hat{\mathcal{P}} \left[\frac{t_{ij} t_{jk}}{2U} \left(\hat{c}^\dagger_{i,\uparrow} \hat{c}^\dagger_{j,\downarrow} + \hat{c}^\dagger_{j,\uparrow} \hat{c}^\dagger_{i,\downarrow} \right) \left(\hat{c}_{j,\uparrow} \hat{c}_{k,\downarrow} + \hat{c}_{k,\uparrow} \hat{c}_{j,\downarrow} \right) \right] \hat{\mathcal{P}} + \mathcal{O}\left(\frac{t^3}{U^2} \right). \end{aligned} \tag{2.2}$$

This expression includes a kinetic energy term, a spin-exchange term on neighbouring sites with the second-order superexchange coupling $J = \frac{4t^2}{U}$, and a next-nearest-neighbour density-assisted hopping term, also scaling as t^2/U. The model is projected onto the subspace without double occupancies using projectors $\hat{\mathcal{P}}$. The density-assisted hopping term, representing hopping of holes within the same sublattice, is commonly omitted as it is much smaller than t [129]. With this, we arrive at the $t - J$

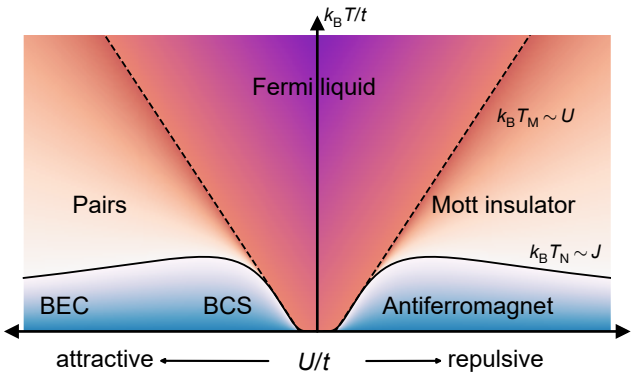

Figure 2.3: Fermi-Hubbard phase diagram. Three-dimensional phase diagram at half-filling, $\langle \hat{n} \rangle = 1$, as a function of interactions and temperature. For repulsive interactions, the system is insulating and exhibits antiferromagnetic ordering at low temperatures. For attractive interactions, superfluid and paired phases appear. Adapted from [91].

model defined as

$$\hat{\mathcal{H}}_{t-J} = -\sum_{\langle i,j\rangle,\sigma=\uparrow,\downarrow} \hat{\mathcal{P}} \left(t_{ij} \hat{c}^{\dagger}_{i,\sigma} \hat{c}_{j,\sigma} + \text{h.c.} \right) \hat{\mathcal{P}} + \sum_{\langle i,j\rangle} J_{ij} \left(\hat{\mathbf{S}}_i \cdot \hat{\mathbf{S}}_j - \frac{\hat{n}_i \hat{n}_j}{4} \right). \tag{2.3}$$

Due to its relative simplicity, while offering a versatile glimpse into complex many-body systems, it is popular for theoretical investigations. For $J < t$, it can be a good approximation of the Hubbard model. In the limit of half-filling, i.e. $\langle \hat{n}_i \rangle = 1 \, \forall i$, the kinetic energy term vanishes and the Hamiltonian reduces to a simple spin system, the Heisenberg model given by

$$\hat{\mathcal{H}}_H = \sum_{\langle i,j\rangle} J_{ij} \hat{\mathbf{S}}_i \cdot \hat{\mathbf{S}}_j. \tag{2.4}$$

2.2.3 Fermi-Hubbard phase diagram

The phase diagram of the Fermi-Hubbard model as a function of interactions and temperature exhibits both charge- and spin-ordered phases (see Fig. 2.3). In this work, we will focus on repulsive interactions at temperatures around the superexchange energy J, where dopants in an antiferromagnetic background lead to interesting new phases (see section 4.1.1). Here, we provide a brief overview of the rest of the phase diagram. For very high temperatures, the system behaves metallic with Fermi-liquid like behaviour, independent of the interactions [130]. When lowering the temperature below the energy scale given by the interactions, on the repulsive side, charge fluctuations are reduced and the system becomes an incompressible Mott insulator. On the

attractive side, this corresponds to the onset of pairing. Upon further cooling below the Néel temperature T_N [131], second-order superexchange coupling leads to antiferromagnetic spin order for repulsive interactions. According to the Mermin-Wagner theorem, this is only a long-range ordered state in three dimensional systems, while for 2d, true long-range order is only reached at $T = 0$ (and in 1d there is no long-range order at all) [132]. The Néel temperature is highest at around $U/t = 8$, which is close to physically relevant parameters. Correspondingly, in the attractive regime, there is a transition to a superfluid state where a crossover from a Bose-Einstein condensate (BEC) to a Bardeen-Cooper-Schrieffer (BCS) superfluid occurs. [89, 91]

2.3 Optical lattice potentials

Optical dipole potentials are a valuable tool, allowing to trap laser-cooled atoms in various internal states while offering versatile trapping geometries [93]. The fast oscillating electric field of the driving laser induces an electric dipole moment in the atom, enabling the manipulation of the atom without any actual excitation. This makes use of the AC Stark shift given (for two-level systems) by $\Delta E = \hbar\Omega^2/(4\Delta)$ with Rabi frequency Ω and detuning Δ [133]. For far-detuned Gaussian beams with intensity profile $I(\boldsymbol{r})$, this leads to a dipole potential of [93]

$$V(\boldsymbol{r}) = \frac{3\pi c^2}{2\omega_0{}^3}\frac{\Gamma}{\Delta}I(\boldsymbol{r}) \tag{2.5}$$

with beam waist w_0, excited state decay rate Γ and detuning Δ. Note, that we can generate attractive potentials by using negative detunings, i.e. red-detuned beams. Comparing this to the off-resonant scattering rate given by

$$\Gamma_{\mathrm{sc}}(\boldsymbol{r}) = \frac{3\pi c^2}{2\hbar w_0{}^3}\left(\frac{\Gamma}{\Delta}\right)^2 I(\boldsymbol{r}) \tag{2.6}$$

we can deduce that minimised off-resonant scattering can be achieved for far-detuned optical dipole traps.

Multiple beams can be interfered with each other to generate an optical lattice. For a single beam with electric field $E(\boldsymbol{r}) = E_0 e^{-i\boldsymbol{k}\cdot\boldsymbol{r}-i\omega t}$ and wave vector $\boldsymbol{k}$, we define the lattice potential as

$$V(\mathbf{r}) \propto |E_1(\mathbf{r}) + E_2(\mathbf{r})|^2 = V_0 \sin^2\left(\frac{1}{2}\Delta\boldsymbol{k}\cdot\boldsymbol{r}\right) \tag{2.7}$$

Depending on the interference angle, the corresponding lattice constant is

$$a = \frac{\lambda}{2\sin\alpha} \tag{2.8}$$

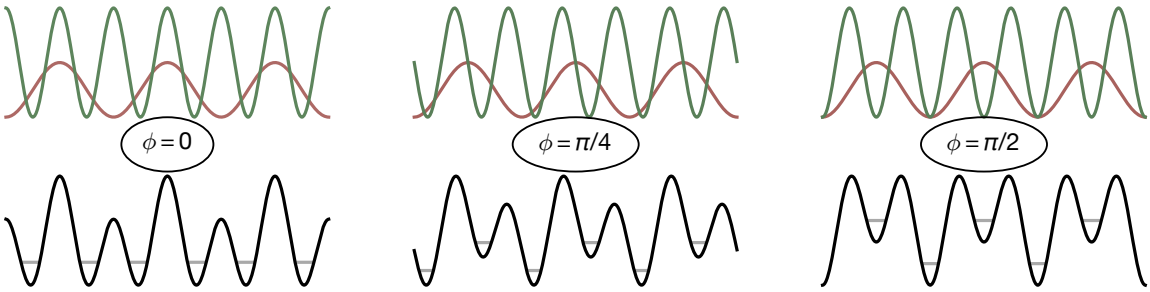

Figure 2.4: Superlattice potentials. By adding two lattice potentials with commensurate lattice constant, different geometries can be realised. For relative phase $\phi = 0$, a series of double-wells is created, while for $\phi \neq 0$, increasing offsets develop.

where λ is the wavelength and α the half-opening angle. The energy scales are then given by the recoil energy

$$E_R = \frac{h^2}{8ma^2} \tag{2.9}$$

where m is the atomic mass. The depth of the lattice is typically expressed in units of the recoil energy. Depending on the geometry of the lattice beams, a wide range of optical lattice potentials can be achieved (see section 3.1). Here, we consider superlattice potentials where two separate lattices with a fixed relation between their lattice constants are overlapped. The resulting (one-dimensional) potential is given by

$$V(x) = V_L \sin^2(k_L x + \phi) + V_{SL} \sin^2(k_{SL} x) \tag{2.10}$$

where $k_L = 2k_{SL}$ and the relative phase ϕ. This relative superlattice phase is crucial as it determines the precise potential shape. It is given by

$$\phi = \phi_L - 2\phi_{SL}. \tag{2.11}$$

For $\phi = 0$, the resulting potential is a series of symmetric double-wells, while for $\phi = \pi/2$, a fully imbalanced, antisymmetric potential is reached. In addition to this relative phase, we have omitted the absolute phase from Eq. (2.10) as it only corresponds to a global translation of the potential and therefore initially does not impact any system parameters. It is given by

$$\phi_{abs} = \frac{1}{2}\left(\phi_L + 2\phi_{SL}\right). \tag{2.12}$$

The Gaussian shape of the lattice beams leads to an additional global potential envelope which limits the achievable system size. For red-detuned beams, there is a confining contribution, due to the varying intensity of the Gaussian beam, which can

be expressed as

$$\omega_c = \sqrt{\frac{4V_0}{mw_0^2}}. \tag{2.13}$$

This contribution mostly acts along the radial direction as the axial intensity variation scales with the Rayleigh length $z_R = \frac{\pi w_0^2}{\lambda} \gg w_0$. Additionally, there is an anticonfining contribution as the zero-point energy of the local harmonic oscillators varies across the system. This contribution can be approximated by

$$\omega_{ac} = \frac{h}{2maw_0}\left(\frac{V_0}{E_R}\right)^{1/4}. \tag{2.14}$$

For blue-detuned lattices, the confining term vanishes as the atoms sit at the position of potential minima, while the anticonfining term remains. This term is usually smaller than the confining part, making blue-detuned lattices advantageous.

For depths of $V \gtrsim 5E_R$, the tight-binding limit is reached, where a description in terms of Wannier functions $w(\mathbf{r})$, i.e. wave functions localised on individual lattice sites, is valid. In this limit, the potential allows for the simulation of Bose- and Fermi-Hubbard models. By calculating the overlap of the wave functions on neighbouring lattice sites, we can identify the tunnelling rate of Eq. (2.1) as [88]

$$\frac{t}{E_R} \simeq \frac{4}{\sqrt{\pi}}\left(\frac{V_0}{E_R}\right)^{3/4} e^{-2\sqrt{\frac{V_0}{E_R}}}. \tag{2.15}$$

For sufficiently deep lattices, it can also be simply related to the bandwidth as $W = 4tD$ with dimensionality D and bandwidth W [134].

On the other hand, in neutral atom quantum simulators, the interactions are no longer mediated by Coulomb interactions but instead only by contact, i.e. on-site interactions [135]. The ultracold regime is reached as soon as only the lowest partial waves contribute to the scattering process. In these cases, we can describe the interactions by a single parameter, the scattering length a_{sc}. The corresponding contact interactions are then given by [88]

$$U = \frac{4\pi a_{sc}}{m}\int d^3r\, |w(\mathbf{r})|^4 \tag{2.16}$$

which we can simplify, again for sufficiently deep lattice potentials, to

$$\frac{U}{E_R} \simeq \sqrt{8\pi}\frac{a_{sc}}{a}\left(\frac{V_0}{E_R}\right)^{3/4}. \tag{2.17}$$

We can vary the scattering length using Feshbach resonances [136–139], i.e. by applying a magnetic field. The availability of appropriate resonances is an important factor when choosing the atomic species. We note that for fermions, the s-wave scattering rate of fermions in identical spin states vanishes due to the Pauli blockade such that they are effectively non-interacting.

2.4 Experimental setup

In this section, an overview of the experimental apparatus to produce ultracold atomic ensembles of ^{6}Li in a 3d optical lattice is provided. More details on the newly designed lattices along x and y are given in the following chapter. For further information on the experimental setup, see [140–142].

2.4.1 Properties of ^{6}Li

We use fermionic ^{6}Li in our experiment due to its numerous favourable features for quantum simulation of the Fermi-Hubbard model. Being an alkali metal atom, its properties are hydrogen-like with a single electron in the $2S_{1/2}$ state. This makes laser cooling and imaging comparably easy. The most important transitions are around 671 nm with the D_1 and D_2 transition to the $2P_{1/2}$ and $2P_{3/2}$ state respectively, only being separated by about 10 GHz. These transitions are relatively broad with a linewidth of $5.87 \times 2\pi$ MHz [143]. Therefore, spin-dependent potentials using vector light shifts are not feasible due to excessive off-resonant scattering. Furthermore, the D_2 excited state hyperfine structure is unresolved due to its small splitting of $1 - 2$ MHz. On the other hand, the ground state hyperfine splitting between the $F = 1/2$ and $F = 3/2$ state is 228.2 MHz [143], which can easily be bridged using acousto-optic modulators (AOM). We label the individual m_F states of these two hyperfine levels by $|1\rangle$ to $|6\rangle$, motivated by the energetic ordering from lowest to highest energy state in the Paschen-Back regime. Experimentally, we mostly operate with the states $|1\rangle$ ($F = 1/2$, $m_F = -1/2$) and $|2\rangle$ ($F = 1/2$, $m_F = 1/2$). Finally, the transition to the $3P_{1/2}$ and $3P_{3/2}$ state at around 323 nm is significantly narrower with a linewidth of $\Gamma_{3P} = 159 \times 2\pi$ kHz, corresponding to a smaller Doppler temperature of 18 µK [144].

The relatively small ground state hyperfine splitting leads to a decoupling of nuclear spin and orbital momentum at small magnetic fields, such that for ca 100 G the Paschen-Back regime is already reached. We show the dependence of the sublevel energies on magnetic field in Fig. 2.5b. Note that for the three lowest lying states, the slope of the Zeeman shift is close to identical and therefore applied gradients mostly spin-independent.

Finally, the scattering length a_{sc} as a function of magnetic field between the three lowest hyperfine states is depicted in Fig. 2.5c. All three combinations feature a broad Feshbach resonance. Most relevant for our purpose, the $|1\rangle - |2\rangle$ mixture has a vanishing background scattering length and a broad Feshbach resonance at 834 G [139]. For magnetic fields up to this value, we can therefore reach any scattering lengths above $-290a_B$. We can use the additional narrow resonance at 543 G (with a width of $\sim$ 100mG) to calibrate our magnetic field.

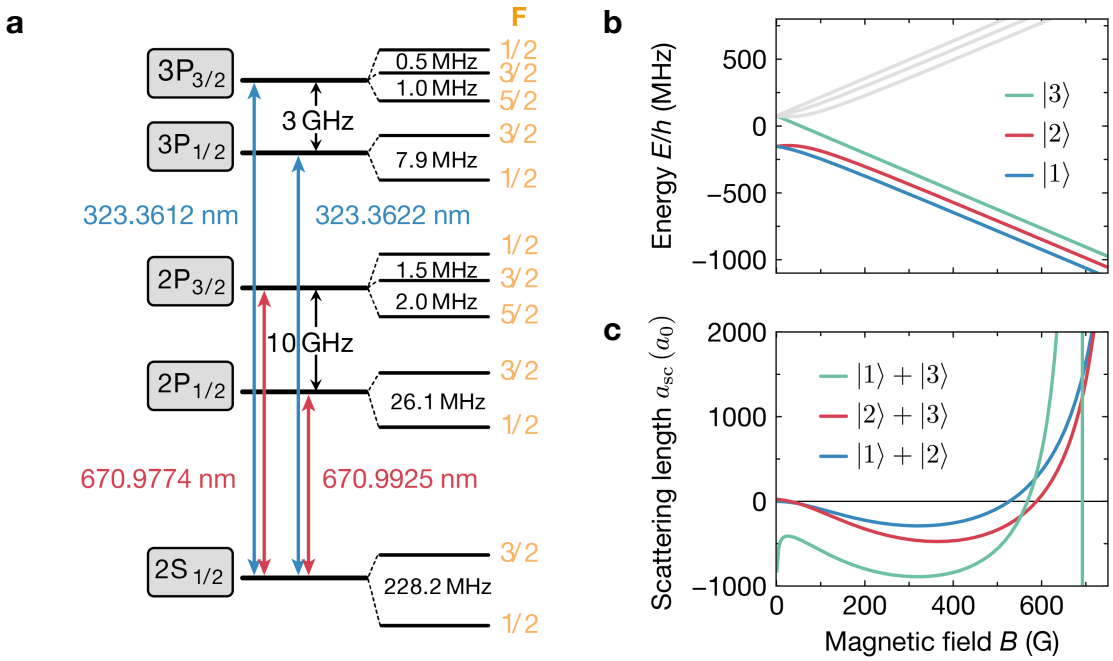

Figure 2.5: Properties of ^{6}Li. **a**, Energy level diagram of ^{6}Li. For laser cooling and detection we use the transitions around 671 nm and 323 nm. **b**, Breit-Rabi diagram for ^{6}Li in a magnetic field. In the low-field regime, the $|1\rangle$ and $|2\rangle$ states have opposite magnetic moments. **c**, Scattering length for atoms in the three lowest hyperfine states with data from [145]. We work in the $|1\rangle$ and $|2\rangle$ states below the Feshbach resonance at 834 G [139]. The figure is adapted from [142].

2.4.2 Preparation of ultracold samples

Initial laser cooling and trapping

In our experiment, we prepare a cold ensemble of ~ 500 atoms in a single plane of a 3d optical lattice. A single realisation, including detection, takes about 20 s. We start with lithium heated in an oven to about 300 °C. This source is set in an ultra-high vacuum steel chamber evacuated to $\sim 5 \times 10^{-10}$ mbar (with pressures further away from the oven going down to $\sim 4 \times 10^{-11}$ mbar). After exiting the oven chamber, the atomic beam is collimated using a 10 mm aperture and travels through a Zeeman slower for 35 cm. During this stage, a counter-propagating beam that is 100 MHz detuned from the D_2 cooling transition ($|2S_{1/2}, F = 3/2\rangle \rightarrow |2P_{3/2}, F = F'\rangle$) in addition to a gradient of $\sim$ 15G/cm slows the atoms down to prepare them for subsequent trapping. This happens in a magneto-optical trap (MOT) in a steel octagon chamber. Three retro-reflected MOT beams address the atoms for both cooling ($|2S_{1/2}, F = 3/2\rangle \rightarrow |2P_{3/2}, F = F'\rangle$) and repumping ($|2S_{1/2}, F = 1/2\rangle \rightarrow |2P_{3/2}, F = F'\rangle$), each detuned

by $\sim 8\Gamma_{2P}$. We load the MOT for 5 s before compressing it within 10 ms. This then leads to a cloud of $\sim 5 - 10 \times 10^7$ atoms at a temperature of 300 µK, on the order of the Doppler limit of 140 µK. This loading procedure takes up a significant portion of our cycle time, and is currently limited by available power in the Zeeman and MOT beams as well as the flux of the atomic beam due to comparably low oven temperatures. By exchanging the oven part of the vacuum setup with a newly developed design, the flux could be improved significantly.

For the next step, we make use of the much smaller linewidth of the UV transitions to the $3P_{1/2}$ state. We briefly load from the red MOT into a UV MOT at 323 nm, where we are able to reduce the temperature within 13 ms to about 50 µK. We end up with $\sim 1.5 - 3 \times 10^7$ atoms. By turning the repumping beam off 500 µs earlier, we optically pump the atoms into a balanced mixture of $|1\rangle$ and $|2\rangle$ state. Currently, we are using a system of sum-frequency generation and doubling in a cavity to generate the required UV light (see [140] for more details). By increasing the available power, higher capture rates would be possible. Alternatively, sub-Doppler cooling using grey molasses would allow for simplified setups without the need for UV light [146–149].

From this UV MOT, we then load into an optical dipole trap. This is facilitated as the UV transition has a magic wavelength at 1069 nm where the polarisability of the ground and excited states match. We use a broadband source at 1070 nm[1] to load into a 90 W beam focussed into the UV MOT. We transfer about $1 - 2 \times 10^6$ atoms at a temperature of 30 µK.

The main part of the experiment is executed in a rectangular glass cell for improved optical access. We transport the atoms into that glass cell by loading into a separate transport beam at 1064 nm by mechanically moving the focus by 28.84 cm from the initial MOT chamber into the science chamber[2]. Starting with about 3×10^5 atoms in the MOT chamber, we transport up to 80% into the glass cell with minimal heating.

Single-plane loading and evaporation

After having transported the atoms into the glass cell, the next goal is to load these into a single plane of our vertical lattice. This is a requirement for quantum gas microscopes to minimise background artefacts during imaging. For this purpose, we first transfer the atoms into a vertically crossed dipole trap projected through our high-NA objective. To achieve a tighter focus along the vertical direction, we then load into a strongly elliptical light sheet[3] with a focus of $w_0 = 2.1\,\mu\text{m}$ ($w_0 = 30\,\mu\text{m}$) along the

[1] YLR-200-LP by IPG Photonics
[2] ABL1500 by Aerotech
[3] $\lambda = 780$ nm, using a DFB diode

vertical (horizontal) direction. We prepare about 2×10^4 atoms at a temperature of 3 µK in this light sheet. To further reduce the temperature and lower the chance of loading atoms in wrong planes of the optical lattice, we evaporate in this dimple trap by lowering its depth from 5 µK down to 1 µK before ramping back up. This lowers the temperature down to $\sim$ 1µK with approximately 2500 atoms.

Loading into a vertical lattice can be facilitated by using a larger lattice constant. We use a bichromatic superlattice with lattice constants of $a_{\mathrm{L}} = 3\,\mu\mathrm{m}$ ($a_{\mathrm{SL}} = 6\,\mu\mathrm{m}$) for the lattice and superlattice respectively. We achieve a high-degree of relative phase stability, crucial for our detection scheme (see following section). For the initial loading, we make use of the large superlattice separation which allows for direct loading from the light sheet without the need for radio-frequency slicing. We are able to load all atoms from the light sheet without any measurable loss or heating into the lattice. Slow changes in the absolute phase of the lattice can lead to multiple planes being populated. We implement a slow feedback procedure that negates this effect. Further details on the design and implementation of this vertical lattice were described in [101, 142, 150], with the general principle also being detailed in the next chapter. After loading the atoms into this deep superlattice ($V_z^{\mathrm{SL}} = 120\,E_{\mathrm{R}}$), we add the short lattice ($V_z = 50\,E_{\mathrm{R}}$) in the antisymmetric phase ($\phi = \pi/2$) to achieve a stronger confinement of 14 kHz. Then, we apply a magnetic gradient along the y-direction while setting the interactions to $353\,a_{\mathrm{B}}$. By slowly increasing the strength of the magnetic gradient over the course of 5 s, we perform a forced evaporation to achieve temperatures as low as $T/T_F = 0.1$. Due to the sufficiently high magnetic fields, we are deep in the Paschen-Back regime and therefore preserve the balanced spin mixture as both components are addressed equally. We end our evaporation with about $400 - 500$ atoms which can be easily varied using the evaporation parameters.

Final loading into optical lattices

Starting with this 2d cloud, we now want to prepare the atoms in the horizontal lattices for the final physical parameters. For this purpose, we first load from the vertical crossed dipole trap into a shaped potential using a digital micromirror device (DMD)[4]. We refer to [151] for further details on the setup. We improved on the setup since then by exchanging the source from a superluminescent diode[5] running at 650 nm to a high-power source by combining four diodes at 638 nm[6] for a total output power of 2 W after fibre coupling to the DMD. By using a combination of a spectrally broadband source and a (square) multimode fibre, we get a spatially incoherent source to minimise interference speckles [152]. This allows us to apply po-

[4] DLP V-7000 VIS by Vialux
[5] EXS210030-03 by Exalos
[6] HL63623HD by Ushio

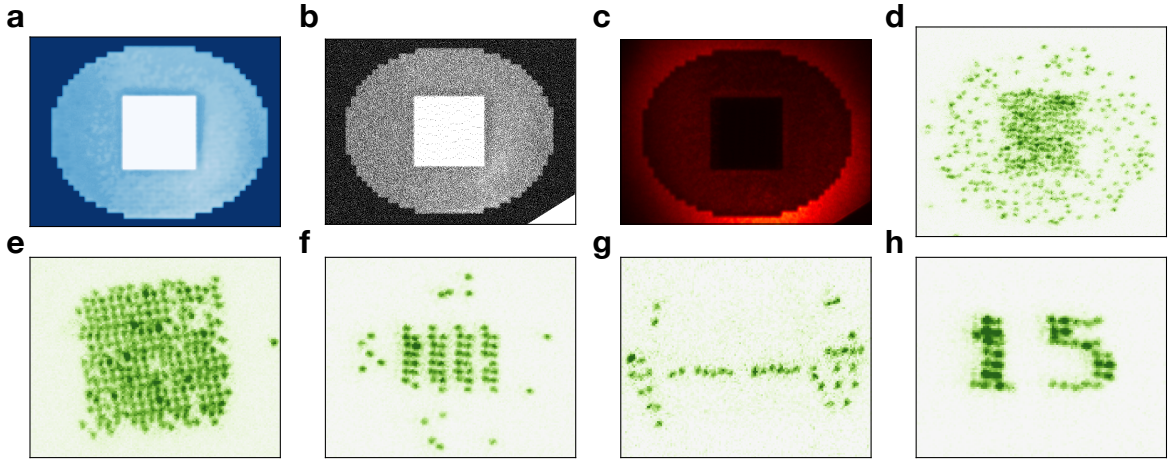

Figure 2.6: Arbitrary potential shaping using a DMD. Starting from the desired potential shape (**a**), we apply a dithering algorithm to get the position of every individual micromirror (**b**), which results in a beam shape on a camera as seen in **c**. A single realisation with this potential is shown in **d**. A selection of different patterns is applied in **e-h** to showcase the wide range of possible potentials.

tential offsets of up to 15 kHz per lattice site, which is several times larger than our normal interaction strengths of $\sim$ 4 kHz. With 15.5×15.5 DMD mirrors per lattice site, we are able to address individual sites and arbitrarily shape our optical potential. In Fig. 2.6 we show exemplified DMD patterns, how they translate to the optical potential as well as the resulting fluorescence images (see also the following section for details on the detection). We rely on a dithering algorithm to set the position of the individual mirrors on the DMD within a lattice site to achieve the desired overall depth [153, 154].

For most of our experiments, the DMD potential is a flat disk, surrounded by a reservoir at higher potential and a high barrier. This geometry allows for transfer of entropy between the (close to) Mott insulating central region and a low-filling, metallic reservoir which effectively cools down the main system in the centre [64, 154, 155]. From this DMD potential we then load into our optical lattice at our final parameters (see also section 3.4.1 for more details on preparation). We work with lattices with a lattice constant of $a = 1.15\,\mu$m which, due to lithium's light mass, still has large couplings while making single-site detection easier. For details on the previous lattice setup we refer to [141] while we describe the changes to the lattice setup during the course of this thesis in the next chapter in detail. By changing the depth of the optical lattice as well as the magnetic field, we can realise Fermi-Hubbard systems with almost arbitrary values U/t. We usually set our system size to be between $100 - 250$ sites, with an additional surrounding reservoir.

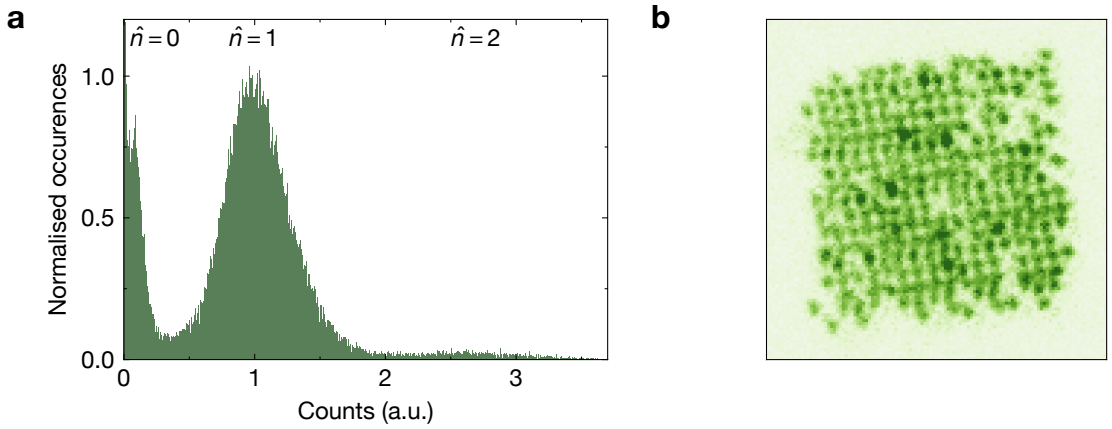

Figure 2.7: Single-site detection. **a**, Histogram of counts per lattice site for reconstruction. The peak at occupation 1 is clearly separated from empty sites. We also have a few doubly occupied sites that can be identified at higher counts. **b**, Single site-resolved image of atoms in a 2d lattice set in a box potential.

2.4.3 Spin-resolved, single-site detection

Density readout

We detect the state of the prepared ensemble by performing fluorescence imaging with single-site resolution [60]. This allows for the readout of the occupation and spin state on each individual lattice site. For lithium, very deep lattices are needed to achieve high-fidelity readout which leads to high requirements on the available laser power. Our lattices are optimised for low harmonic confinement, large spacings and their superlattice capabilities which in turn makes imaging in these lattices not feasible. For this reason, we implement another set of lattices solely for imaging. After the desired physical system has been prepared, we freeze the dynamics by ramping the lattices to $45\,E_\mathrm{R}$ within 1.5 ms. Then we transfer into a set of retro-reflected lattices at 1064 nm[7] within 20 ms at a depth of more than $1000\,E_\mathrm{R}$ each. This leads to on-site trap frequencies of up to 2 MHz, allowing us to apply Raman sideband cooling during detection. With a pair of Raman lasers, we couple the $|2S_{1/2}, F = 1/2, n = n'\rangle$ and $|2S_{1/2}, F = 3/2, n = n' + 1\rangle$ states to transfer atoms to lower vibrational sublevels n. Adding a repumping beam on the $|2S_{1/2}, F = 1/2\rangle \rightarrow |2P_{1/2}, F = 3/2\rangle$ transition, leads to a fluorescence signal that we pick up using a microscope objective[8] with a numerical aperture of 0.5. We estimate our imaging fidelity during the 1 s exposure time to be 98% (by comparing the occupation in subsequent images of the same sam-

[7] Generated using fibre amplifiers ALS-IR-1064-50A-CC by Azurlight Systems
[8] Custom design, Special Optics

ple), limited by the lattice depth and thus available laser power. Another important feature gained by the separation of physics and detection lattices is the avoidance of parity projection [57, 156–158]. While most quantum gas microscopes are thus limited to measuring the parity of the occupation (such that doubly occupied sites appear as holes), our detection lattices oversample the physics lattice by a factor of ~ 8. By applying strongly repulsive interactions during the transfer, doubly occupied sites in the physics lattice are split into separate sites in the detection lattice and thus are not lost during imaging, giving us access to full-counting statistics. Using simple deconvolution algorithms, we can extract the total fluorescence counts on each lattice site and use the resulting histogram of counts to assign the occupation. We achieve reconstruction fidelities of about 99.4% [142]. We show a single realisation of a 2d Mott insulator as well as the corresponding histogram in Fig. 2.7.

Spin readout

Imaging the spin state of atoms on individual lattice sites is crucial for the investigation of the spin order of Fermi-Hubbard systems. For this purpose, quantum gas microscopes either rely on selective spin removal techniques [103] or spin-dependent spatial separation [65, 101, 105]. Here, we use our vertical bichromatic superlattice to locally resolve the atoms' spin state. Further details of this procedure can be found in [101, 142].

We begin by loading the sample from the short vertical lattice into the superlattice. At this point, dynamics along x and y are frozen using the in-plane lattices. Subsequently, we apply a magnetic gradient of $45\,\mathrm{G/cm}$ along the vertical direction. We make sure that the overall magnetic field is close to zero, such that the magnetic moments of the two spin states have opposite signs. This biases the potential in opposite directions. We then ramp the short lattice back up in the symmetric phase configuration $\phi = 0$, such that a symmetric double-well is formed. Depending on their spin state, atoms will end up in different double-wells and are therefore separated by $3\,\mu\mathrm{m}$. For our highly-stable system, this procedure is very robust and insensitive to the precise phase. We check this by varying the phase at which the lattice is ramped up and measuring the occupation in the two double-wells (see next paragraph for further details). We show the results of this measurement in Fig. 2.8. For a wide regime of about 350 mrad, we split the atomic cloud in half, while for larger phase offsets, all atoms end up in one part of the double-well as the double-well detuning dominates over the magnetic gradient.

Charge pumping

The Stern-Gerlach sequence described above spatially separates the atoms by $3\,\mu\mathrm{m}$, which is not much larger than the depth of focus of our objective. Therefore, when

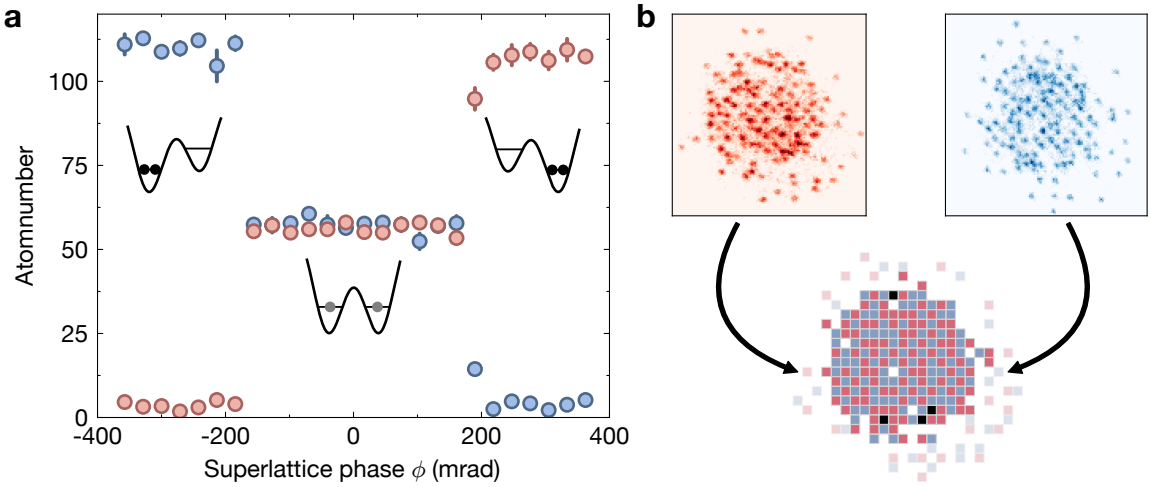

Figure 2.8: Spin-resolved imaging. a, Stern-Gerlach sequence with varying superlattice phase ϕ. In red, blue we show the atom number in both parts of a double-well after applying a magnetic gradient and loading into a superlattice potential at phase ϕ. For a broad range of ~ 350 mrad, the applied magnetic gradient splits the two spin states in separate parts of the double-well. Once the detuning is larger than the offset due to the gradient, no spin-dependent splitting occurs but all atoms are prepared in a single well. Detection occurs after charge pumping to increase the separation to 21 µm. **b**, Single fluorescence images of spin-up and spin-down atoms in separate planes. The reconstructed occupation from the two planes exhibits antiferromagnetic correlations.

trying to image either plane, a substantial background to the image will be present, which makes high-fidelity reconstruction impossible. To circumvent this problem, we make use of the topological properties of our vertical superlattice to increase the distances between the two planes. As pioneered in [159, 160], by performing a sequence of adiabatic passages, atoms initialised in different parts of a double-well will be transported in opposite directions. This procedure, similar to a topological Thouless pump [161, 162], works due to the different Chern numbers of the ground and excited band in a tilted double-well potential. The precise sequence is as follows (see also Fig. 2.9a): we start with atoms in a double-well of a deep lattice and superlattice ($V_z = 50\,E_\mathrm{R}$, $V_z^\mathrm{SL} = 130\,E_\mathrm{R}$) with a symmetric phase $\phi = 0$. We then change the phase such that the atoms are coupled to different double-wells, close to their symmetric phase. After lowering the lattice depth to $V_z = 11\,E_\mathrm{R}$, we perform a slow adiabatic sweep of the phase across the symmetric phase to transfer the atoms to the other well, before ramping the lattice back up. We can repeat this sequence to increase the distance between the atoms by 6 µm per iteration. We show absorption images from the side in Fig. 2.9b, which showcase the stepwise separation of initially neigh-

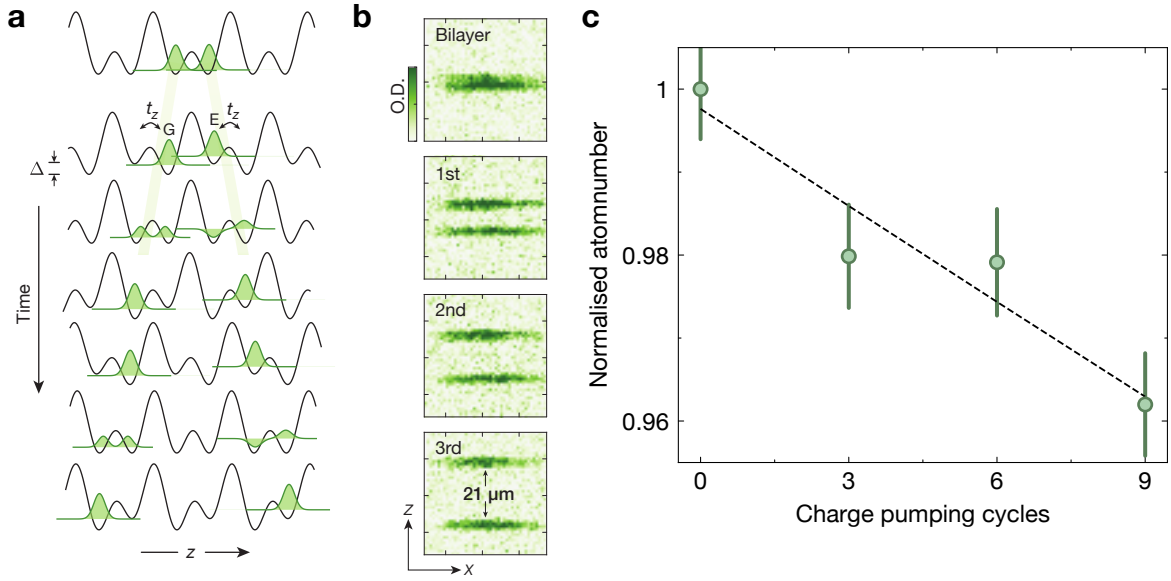

Figure 2.9: Charge pumping in an optical superlattice. **a**, Sequence for topological charge pumping. Applying a series of adiabatic passages using the relative superlattice phase moves atoms in different bands in opposite directions. **b**, Absorption imaging of 2d planes at different distances from the side. **c**, Charge pumping efficiency as a function of applied cycles. We extract a fidelity of 99.61(9)% per cycle.

boured planes. We extract the fidelity of this procedure using a fit in Fig. 2.9c yielding 99.61(9)% per cycle. For our purposes, we choose three iterations, i.e. a separation of 21 µm, where the imaging background is sufficiently small. We show fluorescence images of two planes in 21 µm distance in Fig. 2.8c. The background from the other plane is small and can be further suppressed using image processing techniques [163].

Bilayer readout

In order to image spin states in two separate planes, two different methods can be applied: first, we can take two subsequent images where we move the focus of our microscope objective in between. This method was first used when implementing the bilayer imaging procedure [101] but suffered from a lack of stability of the objective. We would find small, not reproducible deviations in horizontal position which added additional challenges to our reconstruction. For this reason, an alternative method was considered, where we use two separate imaging paths. We use a polarising beamsplitter to split the fluorescence signal before then sending one part through a 1:1 telescope. Afterwards, we recombine the two paths on another polarising beamsplitter and send both to the EMCCD camera. By slightly adjusting the focus of the telescope, we can precisely change the focus of this second imaging path with respect

to the first one. This allows for simultaneous imaging of two focal planes on the same camera (see [151] for more information).

2.5 Topological phases in fermionic ladders

The described experimental setup has been used for a wide variety of studies on the Fermi-Hubbard model. Single-site resolved measurements of the occupation and spin [60, 65, 101] allowed for investigations into doped systems, directly imaging magnetic polarons [106] and their evolution with doping [66]. Using our potential shaping capabilities, we are also able to study topological effects in ladder systems, which we will briefly describe in the following. These results are published in [164] with some details also given in [151]. Numerical calculations were performed by Ruben Verresen and Julian Bibo.

The intriguing properties of topological phases of matter have sparked increasing interest in recent years. One paradigmatic model is the symmetry-protected topological Haldane spin-1 chain [165, 166], which hosts hidden spin order as well localised spin-1/2 edge states [167, 168]. Quantum simulation can provide a complementary perspective on previous neutron scattering [169, 170] and electron resonance studies [171, 172], which have found evidence for topological properties despite not probing the system microscopically. It has been shown, that there is a direct mapping from a spin-1 chain to a ladder system of spin-1/2 fermions via the AKLT model [173–175]. Therefore, we can use our fermionic system to study the topology of a spin-1 chain, making use of our microscopic resolution.

We prepare 2-leg ladder systems with 14 sites at $U/t_\perp = 12.5(6)$, $J_\perp/J_\parallel = 1.3(2)$. We use potential shaping to load into ladders with two different edge configurations (see Fig. 2.10a, b). Depending on the edges, we realise either a 'trivial' or a 'topological' configuration. For an infinite system, these two configurations would be indistinguishable. By choosing a specific unit cell which can either be vertical or diagonal, we map the system on a spin-1 or spin-0 chain. In our finite size system, we configure the edges to match a specific unit cell to distinguish the two regimes. This does, however, not change the bulk properties itself.

To analyse our ladder system as it maps onto a spin-1 chain, we measure observables on unit cells, i.e. using $\hat{\mathbf{S}}_k = \hat{\mathbf{S}}_{k,0} + \hat{\mathbf{S}}_{k,1}$ in unit cell k. To then reveal the topological features of the system, we use a string correlator. Spin-spin correlations (between unit cells) are short-ranged and decay quickly. By taking into account the spin order between the endpoints, specifically how many spin-0 components are present, we can correct the sign of the correlator (see Fig. 2.10c, d). To be precise, we can define the

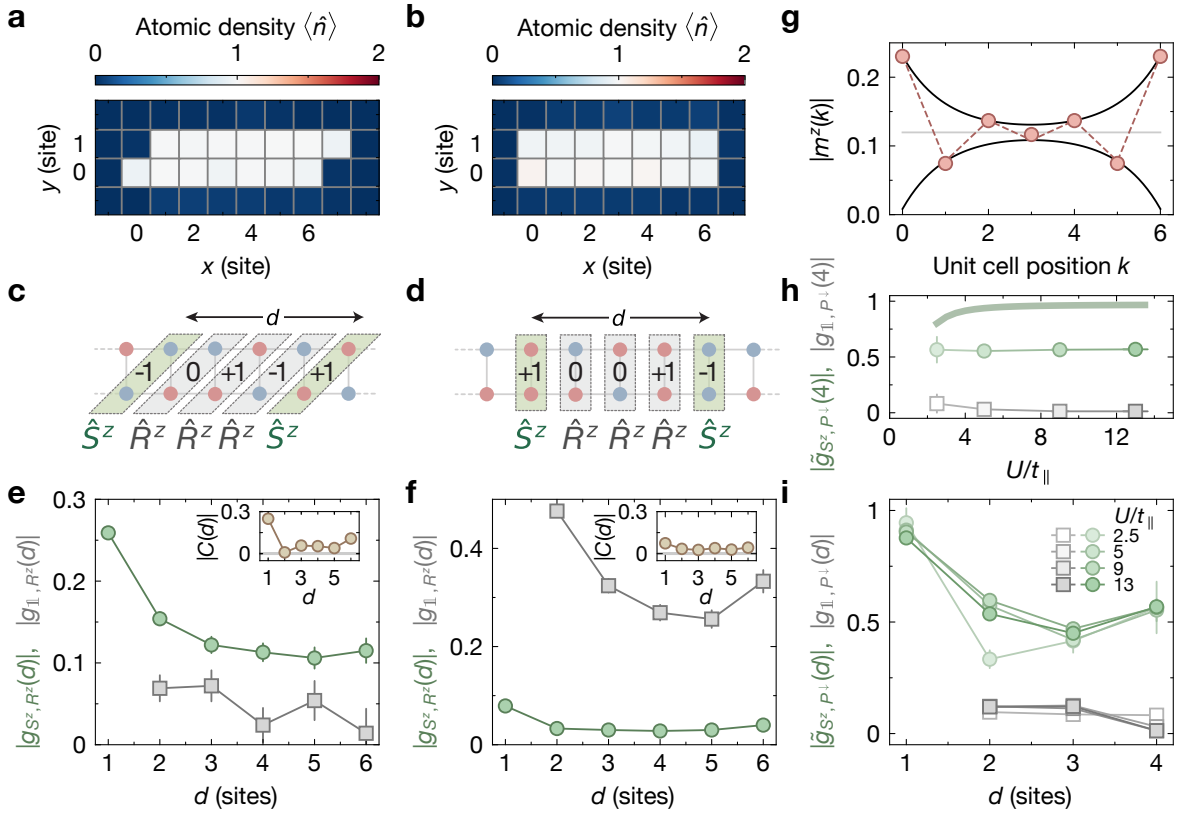

Figure 2.10: Haldane phase signatures in Fermi-Hubbard ladders. **a** (**b**), Prepared density profile in the topological (trivial) configuration. We identify the corresponding unit cell in **c** (**d**) with total magnetisation per unit cell of 0, ± 1. We calculate the string correlator with endpoint operators S^z ($\mathbb{1}$) in green (grey) for the two configurations in **e** and **f**. We observe long-range correlations for g_{S^z,R^z} ($g_{\mathbb{1},R^z}$) in the topological (trivial) configuration. Meanwhile, without the string (i.e. $\hat{U}_l = \mathbb{1}$), correlations are short ranged (see insets). **g**, Magnetisation per unit-cell for $M^z = \pm 1$, where the excess magnetisation is localised at the edges. **h**, Robustness to charge fluctuations. The correlator $\tilde{g}_{S^z,P^\downarrow}$ stays constant when lowering $U/t_\parallel$. We show the full correlator in **i**. DMRG results in **h** at $T = 0$ in the thermodynamic limit are qualitatively similar.

string correlator as [167, 176]

$$g_{\mathcal{O},U}(d) = \left\langle \hat{\mathcal{O}}_k \left(\prod_{l=k+1}^{k+d-1} \hat{U}_l \right) \hat{\mathcal{O}}_{k+d} \right\rangle \tag{2.18}$$

where $\hat{U}_l$ is an on-site symmetry and $\hat{\mathcal{O}}_k$ the endpoint operator in unit cell l with distance d. By using $\hat{U}_l = \hat{R}^z_l \equiv \exp\left(i\pi \hat{S}^z_l\right)$, we probe the bulk $SO(3)$ symmetry of a spin-1 chain. Choosing endpoint operators $\hat{\mathcal{O}}_k = \hat{S}^z_l$ recovers the long-range order

within the system. Therefore, we can identify the presence of the topological Haldane phase via finite values of this correlator at large distances. Meanwhile, we expect the opposite correlator with endpoint operators $\hat{\mathcal{O}}_k = \mathbb{1}$ to be consistent with zero. Both correlators behave exactly inverted in the trivial, non-topological phase, i.e. g_{S^z,R^z} is zero while $g_{\mathbb{1},R^z}$ remains finite.

We study the behaviour of these correlators in Fig. 2.10e, f. We filter our data to have exactly 14 atoms, even atom number within the string of the correlator as well as total magnetisation $M^z = 0$. For diagonal unit cells, we observe a finite value of g_{S^z,R^z} across the system, consistent with the expected topological behaviour. For vertical unit cells, the correlators trade place indicating trivial topology. In either case, the spin-spin correlator with $\hat{U}_l = \mathbb{1}$, however, decays quickly (see insets). We can also use this data to identify edge states by considering the local magnetisation per unit cell. For a total magnetisation of $M^z = \pm 1$, the excess value is mostly localised at the edges with only some decay into the bulk (see Fig. 2.10g).

Finally, the versatility of our approach allows us to leave the Heisenberg regime of strong interactions and consider the weakly interacting Fermi-Hubbard regime, where charge fluctuations are increasingly present. This changes the symmetry of the bulk state from $SO(3)$ to $SU(2)$, such that the bulk and edges cannot be distinguished as easily any more [177, 178]. However, due to the presence of the sublattice and parity symmetry of spin-down particles, $\hat{P}_l^{\downarrow} \equiv \exp\left[i\pi\left(\hat{n}_{l,A}^{\downarrow} + \hat{n}_{l,B}^{\downarrow}\right)\right]$, we can define a new correlator $g_{S^z,P^{\downarrow}}$ which still reveals the hidden order within the system [179]. We lower the interactions down to $U/t_{\parallel} = 2.5$, where we still find finite values for this correlator at the largest distance (see Fig. 2.10h, i). This exemplifies the robustness of the topological order due to the inherent symmetries, despite our finite temperature.

Chapter 3

Design and characterisation of high-stability optical superlattices

This chapter focuses on the details of tunable optical lattices, specifically superlattices. We describe the requirements, design and implementation of high-stability, bichromatic superlattices in our experiment. Following a similar approach to our recently added superlattice along the vertical direction [101], we show how we improved on that design for our in-plane lattices. We characterise the stability and tunability of the lattices in detail using both single-particle and many-body measurements. Some results on the superlattice characterisation in this chapter are contained in [180]. Quantum Monte Carlo calculations for temperature estimations were performed by Zhenjiu Wang.

3.1 Optical lattice geometries and realisations

Interfering a set number of optical lattice beams offers a tremendous amount of versatility in creating numerous potential geometries such as square [181], hexagonal [182], triangular [97], Kagome [183] or Lieb lattices [184]. Depending on the desired application, different ways of generating the individual potential may be beneficial. In the following discussion, for simplicity we will limit ourselves to 2d optical lattice geometries, though the extension to 3d lattices is in many cases trivial.

3.1.1 Static optical lattices

The simplest possible lattice potentials are achieved by interfering pairs of beams with opposite wave vector to realise a square optical lattice with a lattice constant equal to half the wavelength. Similarly, by interfering the beams under a half-angle α (i.e. not directly retro-reflected), lattices with larger lattice constant $a = \lambda/(2\sin\alpha)$ may be created. Finally, three interfering beams can create e.g. honeycomb lattices. In general, these lattices are inherently stable up to global phase factors. This can be shown for any lattice involving at most $d+1$ beams in d dimensions [185]. In this manner, a

variety of different optical lattice geometries without the additional need for active phase stabilisation can be engineered. In addition to the aforementioned lattices, bow-tie lattices are a useful tool to achieve the same kind of stability. Interfering a single-beam four times with itself by folding it back onto itself, allows for phase stable 2d lattices using only a single beam.

3.1.2 Tunable optical lattices

For many applications, static lattices may not be enough, such that additional degrees of freedom for further tunability are desirable. In recent years, a growing number of tunable lattices has been realised, each focussing on different aspects. In the following, we will provide a short overview of past realisations as context for our superlattice described in detail later on (see Fig. 3.1).

First, adding additional frequency components to three interfering beams creates different sets of overlapping optical lattices (see Fig. 3.1a). By tuning the phase between the added frequency sidebands, the geometry may be dynamically tuned from honeycomb ($\beta = 0$) via boron-nitride ($\beta = \pi/3$) to triangular lattices ($\beta = \pi$) [186]. The stability of the lattice geometry is thus reduced to the stability of the frequency source generating the sidebands, which can easily fulfil the necessary requirements.

An alternative method involves changing the polarisation vectors of the individual beams (see Fig. 3.1b). Rotation of the polarisation of each beam by θ continuously changes the geometry from a state-independent honeycomb lattice ($\theta = 0$) via a constant-intensity 'polarisation lattice' ($\theta = \pi/4$) to a (possibly state-dependent) triangular lattice at $\theta = \pi/2$. This offers complementary applications to the fully state-independent multi-frequency approach described above. [187]

A folded bow-tie lattice only uses a single beam to create a 2d lattice. This allows for more beams while still preserving passive stability. As shown in Fig. 3.1c and [59, 109, 188], by adding a 1d, non-interfering optical lattice on top of a bow-tie lattice, a variety of geometries from a square lattice ($A_1/A_0 = 0$) to triangular lattices ($A_1/A_0 \sim 2$) and eventually one dimensional tubes/dimerised lattices can be realised.

Dynamic tunability can also preserve the overall geometry of the lattice while still varying spatial parameters significantly by changing the lattice constant. The so-called 'accordion' lattice [189–191], remains a square lattice throughout, but changes the lattice constant along one or more directions. This is typically achieved by varying the interference angle of the lattice beams, e.g. via galvanometric control [192]. Applications can, amongst others, be found in facilitated single-site imaging [113] or loading into single 2d planes [192, 193].

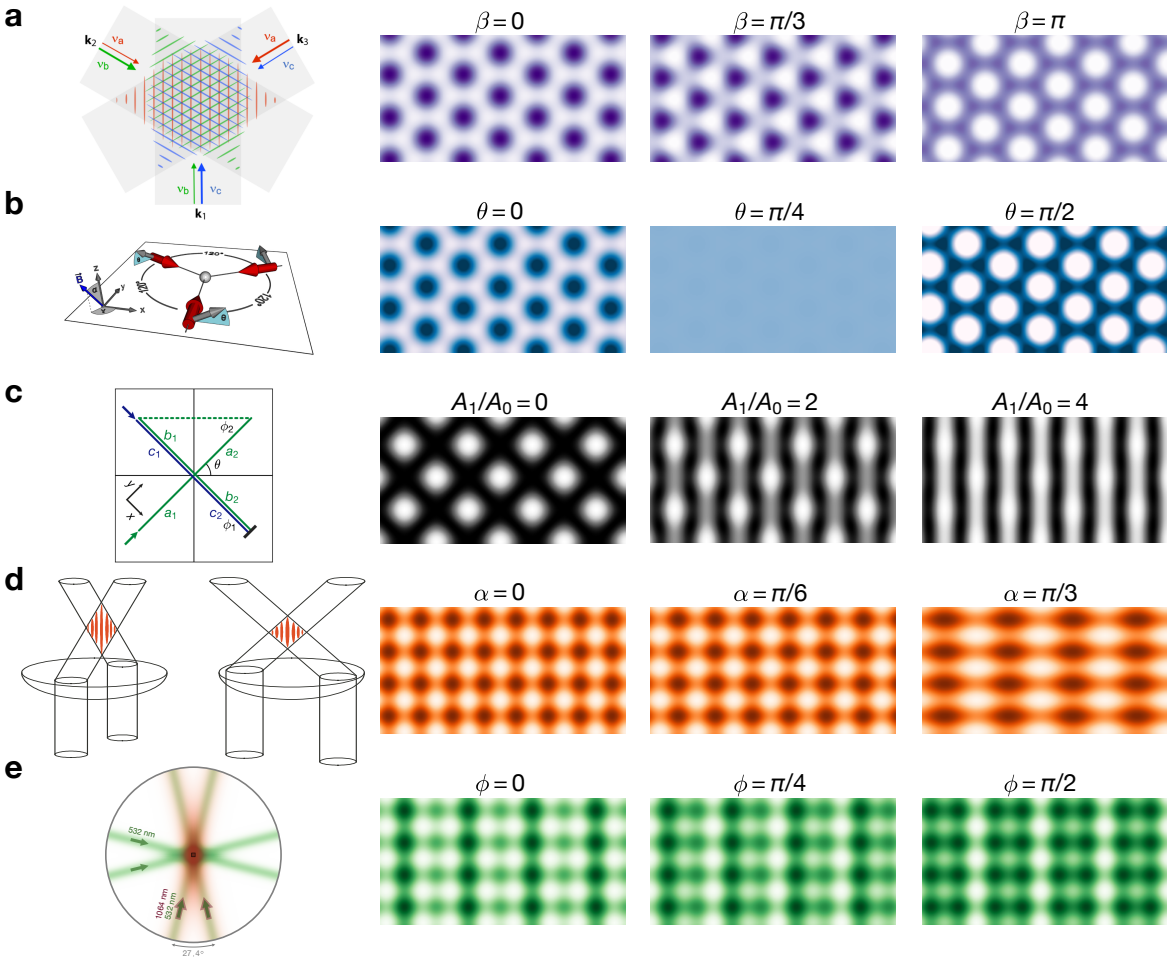

Figure 3.1: Lattices with tunable geometries. **a**, Multi-frequency lattice as demonstrated in [186], realising hexagonal, boron-nitride and triangular lattices. **b**, Polarisation lattice, shown in [187]. Similarly, the potential can be tuned from hexagonal to state-dependent polarisation or triangular lattices. **c**, Bow-tie lattice with additional 1d lattice [188]. Continuous tuning between square, triangular and dimerised lattices is possible. **d**, 'Accordion' lattices allow for smooth changes of the lattice constant [189]. **e**, Superlattices lead to symmetric or imbalanced double-well potentials.

Finally, the method most relevant to this thesis, is an optical superlattice. In this case, another lattice is superimposed onto the first lattice with a fixed relation between their lattice constants. The capability to realise symmetric ($\phi = 0$) as well as imbalanced double-well lattices ($\phi \neq 0$) and fully staggered lattices ($\phi = \pi/2$) by adjusting local detunings on different sublattices, allows for a wide range of applications in preparation, detection and coupling control. In that manner, interferometric measure-

ments [194, 195], double-well oscillations [196, 197], topological effects [159] as well as antiferromagnetic correlations [51] have been studied. It also enabled single-site spin-resolved detection in quantum gas microscopes [65, 106]. Finally, preparation of low-entropy states using controlled coupling has been demonstrated [198]. However, a challenge arises due to the fact that this configuration is *not* inherently stable in contrast to many of the previous setups. Due to the high sensitivity to environmental factors such as temperature, pressure or humidity, either active stabilisation or passive isolation has to be implemented. Because of the severe technical difficulties and ultimate limitations associated with active phase stabilisation [51], we focus here on a passively stable method.

3.2 Requirements on optical superlattices

The design of an optical lattice for an ultracold atoms experiment is subject to numerous constraints, depending on the precise application as well as the rest of the experimental setup. In the following, we briefly summarise common requirements and how these affect design considerations, especially in the context of fermionic quantum simulators.

One important design choice is the lattice constant of the optical lattice. For experiments relying on any kind of (short-ranged) coupling between lattice sites, this determines the experimental time scales. In order to keep these time scales sufficiently small (to minimise the effect of technical noise), choosing small lattice constants is beneficial. This becomes even more crucial the heavier the species of atom chosen. We show the tunnelling rates at a typical lattice depth of $V^{\mathrm{L}} = 6\,E_{\mathrm{R}}$ as a function of lattice constant for ^{6}Li, ^{40}K and ^{87}Rb in Fig. 3.2a. Typical tunnel couplings are on the order of $100 - 1000\,\mathrm{Hz}$. However, on the other hand, exceedingly small lattice constants pose a technical problem for detection. While not necessarily required, read-out of atoms on the scale of individual lattice sites is highly beneficial and allows access to many otherwise hard or impossible to measure observables. Similarly, addressing of individual lattice sites is also a requirement for many experiments. Therefore, the resolution of the imaging system has to be sufficiently high compared to the lattice constant. A common limit is given by the diffraction limit $\lambda/(2NA)$, such that for numerical apertures (NA) of $0.7 - 0.8$, a resolution on the order of 500 nm is possible (where details depend on the species and thus the imaging wavelength). In recent years, methods have been developed to bypass this limit which rely e.g. on machine-learning assisted reconstruction [121] or expanding the quantum system before imaging [199]. However, so far, most experiments still remain above this threshold in lattice constant.

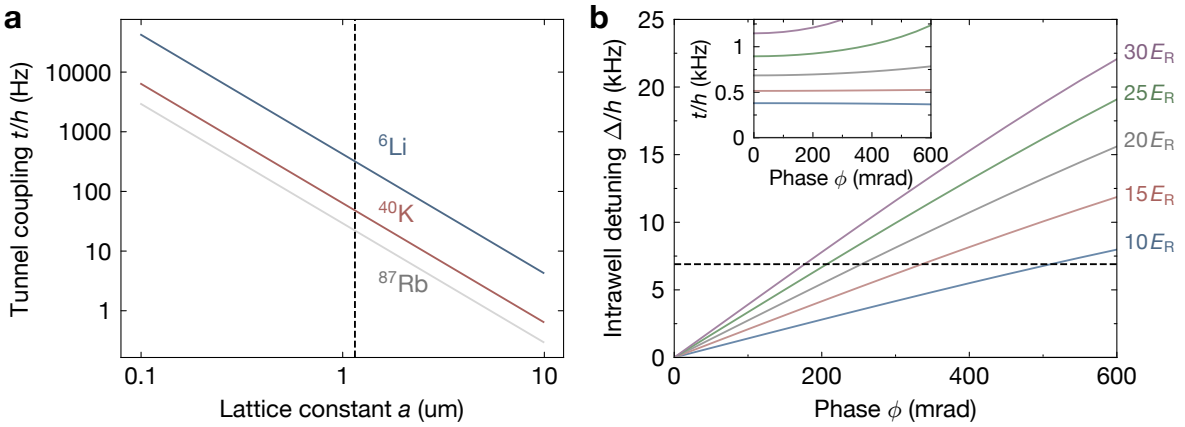

Figure 3.2: Tunnel coupling in superlattices. **a**, Tunnel coupling t in a lattice at $V^{\mathrm{L}} = 6\,E_{\mathrm{R}}$ with variable lattice constant a_{L} for ^{6}Li (blue) [143], ^{40}K (red) [200] and ^{87}Rb (grey) [201]. Energy scales are significantly higher for the light ^{6}Li. The dashed line marks the lattice constant chosen in our experiment. **b**, Intrawell detuning Δ as a function of superlattice phase ϕ for a different superlattice depths ($V^{\mathrm{SL}} = 10, 15, 20, 25, 30\,E_{\mathrm{R}}$) and lattice depth $V^{\mathrm{L}} = 8\,E_{\mathrm{R}}$ for $a_{\mathrm{L}} = 1.15\,\mu$m. The dashed line corresponds to the detuning our gradient can provide. The inset shows the corresponding intrawell tunnelling values.

Optical lattice experiments are often limited by the amount of available laser power[1]. This is caused by the inherent competition between lowering the harmonic confinement by increasing the waist and requiring sufficient power to freeze the dynamics of the system for detection. Harmonic confinement scales inversely proportional to the waist of the lattice beams while the depth scales as $1/w_0^2$. Most experiments image the atomic distribution in the same lattices where the physical investigation occurred. In that case, for most setups, lattice depths on the order of $\sim 1000 E_{\mathrm{R}}$ need to be achieved to minimise detection errors. One possibility to circumvent this requirement is by adding an additional set of lattices solely for imaging with a smaller waist as harmonic confinement does not matter as much any more at this point. This is tremendously helpful as the harmonic confinement during preparation ultimately sets the maximum system size that can be achieved. While in recent years increasingly high-power laser sources have become available, system sizes are still set by power availability. One possible solution to this issue is by using cavity enhancement to increase the lattice depth [202, 203].

Finally, the stability of optical lattices is a crucial question in their design. As mentioned in the previous section, depending on the design strategy, tunable geome-

[1] for a given laser detuning. Higher depths for the same power can be achieved by going closer to resonance, which, however, leads to unwanted off-resonant heating.

tries may either be inherently stable or require active or passive stabilisation methods. Focussing on superlattices, the relative superlattice phase stability determines the possible applications. First, performing local Stern-Gerlach separation of the spin components into separate parts of the double-well potential for spin detection is a common goal. The stability required depends on the feasible magnetic gradient. In our experiment, we can apply a gradient of at most 6 kHz/µm. For high-fidelity spin detection, we require a phase stability of ~ 200 mrad which is reasonably easy to realise (see Fig. 3.2b). For further double-well (or bilayer) physics, requirements may be far higher, especially in the context of fermionic quantum computation. We discuss the consequences of phase noise on the coherence in section 3.4.4. Finally, a high degree of both pointing and absolute phase stability is also crucial in any optical lattice experiment.

3.3 Bichromatic superlattice design

In the following, we describe the specific design of our newly implemented bichromatic superlattices. The general idea follows the design previously used in our vertical superlattice shown in [101, 150] and is briefly summarised in the following. Many improvements in terms of tunability and mechanical design are discussed subsequently.

3.3.1 General features

To realise an optical superlattice[2], i.e. two lattices with commensurate lattice constants where $a_{SL} = 2a_L$, we interfere two pairs of beams at wavelengths of 532 nm and 1064 nm under a half-angle of 13.37 °, resulting in lattice constants of $a_L = 1.15$ µm and $a_{SL} = 2.3$ µm. We improve the stability of the setup by spatially overlapping the beams of the lattice and superlattice such that disturbances affect both lattices equally. Both lattices originate from the same source, where we implement single-pass second-harmonic-generation for the lattice. We use a combination of a delay line in one lattice arm with frequency shifting of the lattice beams using broadband acousto-optic deflectors (AODs) to tune the relative superlattice phase fast and precisely. Furthermore, rotatable glass plates allows for coarse changes of the lattice phase. Finally, in order to improve the stability of the setup, the most sensitive parts are both evacuated and thermally isolated from the environment

The most crucial components of this design are related to the phase stability of the lattice. As stated in the previous section, a highly stable relative superlattice phase is

[2] In the following, we will refer to both the long lattice as well as the full potential as a superlattice and to the short lattice as simply lattice.

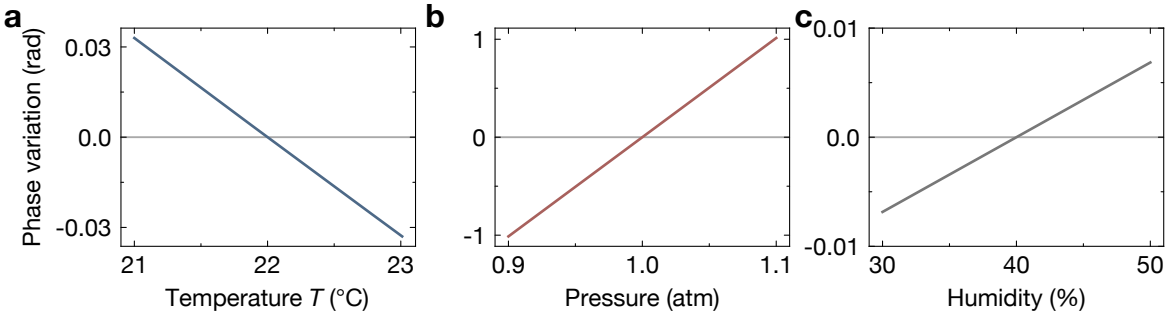

Figure 3.3: Phase change with environmental fluctuations. Relative superlattice phase change for varying conditions compared to normal conditions of $T = 22\,^{\circ}\mathrm{C}$, $p = 1\,\mathrm{atm}$, $H = 40\,\%$ for a delay line of 41.6 cm and $\lambda_\mathrm{L} = 532\,\mathrm{nm}$.

required for many applications while posing a significant technical challenge. Here, we use a passively stable implementation without any need for active feedback. This both allows for high overall stability and simplifies the setup itself. The central idea is based on using two different, commensurate wavelengths for the lattice and superlattice. While traversing a distance L, a single beam with wavelength λ can pick up phase noise $\delta\phi$ via a fluctuating refractive index of the air δn due to either changes in temperature, pressure or humidity

$$\delta\phi = \delta k L = \frac{\pi \delta n L}{\lambda}. \tag{3.1}$$

When now considering the relative superlattice phase for a bichromatic lattice as defined in Eq. (2.11), the total phase fluctuations are

$$\delta\phi = \delta k_\mathrm{L} L - 2\delta k_\mathrm{SL} L = \pi L\left(\frac{\delta n_\mathrm{L}}{\lambda_\mathrm{L}} - 2\frac{\delta n_\mathrm{SL}}{\lambda_\mathrm{SL}}\right) = \frac{\pi L}{\lambda_\mathrm{L}}(\delta n_\mathrm{L} - \delta n_\mathrm{SL}). \tag{3.2}$$

From this it follows, that as long as the dependence of the refractive index on wavelength is weak, i.e. $\delta n_\mathrm{L} \approx \delta n_\mathrm{SL} \approx \delta n$, phase fluctuations in the lattice and superlattice cancel and the relative superlattice phase is inherently stable. This relation holds very well in typical parameter regimes around standard conditions. Following empirical equations for changes of the refractive index of air with temperature, pressure and humidity [204, 205], we can show that residual phase fluctuations due to environmental changes in normal lab conditions are negligible (see Fig. 3.3). This is only the case for bichromatic superlattices, as opposed to monochromatic superlattices, which then require active phase stabilisation. We note that this only holds for the *relative* superlattice phase, while the *absolute* phase still fluctuates as $\delta\phi_\mathrm{abs} = \frac{\pi L}{2\lambda_\mathrm{L}}(\delta n_\mathrm{L} + 2\delta n_\mathrm{SL}) \neq 0$ which is non-zero both for monochromatic and bichromatic superlattices. Therefore, a stable absolute phase either requires active feedback (as e.g. implemented for our

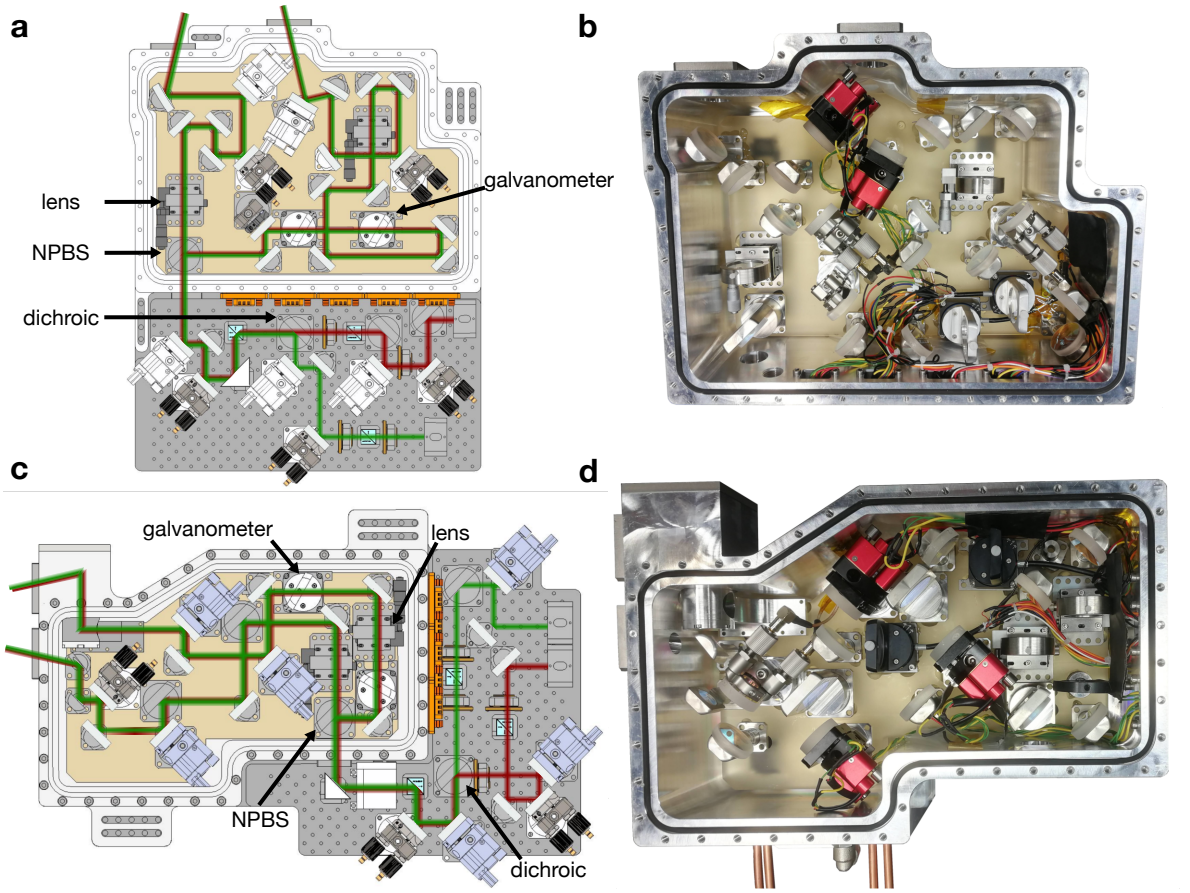

Figure 3.4: Lattice setups. Sketches (**a**, **c**) and images (**b**, **d**) of the evacuated lattice setups along y (**a**, **b**) and x (**c**, **d**).

vertical superlattice, see [142]) or passive isolation from the environment, which is the approach we decided on here, see the following sections for details.

We show the final design of the lattice setups along x and y in Fig. 3.4. The general setup is very similar, however only the y-lattice has a delay line due to lack of space in the experimental setup. Tuning of the relative superlattice phase is however still possible using rotatable glass plates, that are implemented in both lattices.

3.3.2 Optical design

The full optical setup is divided in three parts: the seed laser and amplification, frequency shifting using AODs and the final lattice setup directed at the atoms. For details on the AOD setups we refer to our previous work in [150].

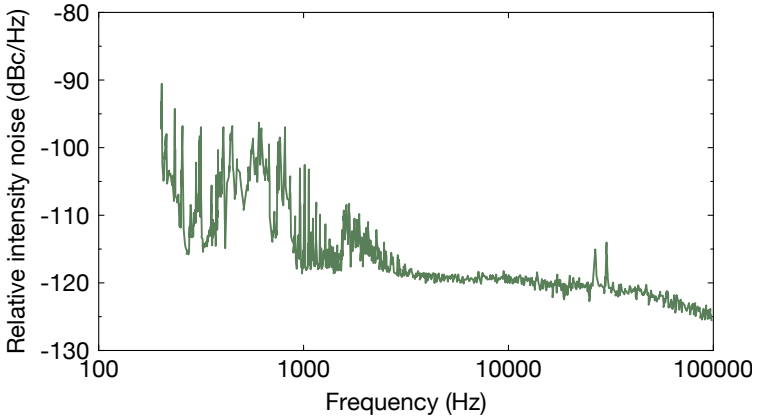

Figure 3.5: Relative intensity noise. Measured noise spectrum for a free-running laser at a wavelength of 532 nm.

We use a 40 W solid-state laser amplifier[3] at a wavelength of 1064 nm as a seed for both the lattice and the superlattice. This seed has excellent linewidth ($\sim$ 1 kHz) and intensity noise (<-120 dBc/Hz) properties and provides enough power for both the x- and y-superlattice. We also split off small fractions that are then either first frequency shifted using AODs (y-lattice) or directly sent to another 45 W amplifier[4] before being used for second-harmonic generation. Following our earlier setup described in [206], we use single-pass doubling in periodically-poled magnesium-doped stoichiometric $LiTaO_3$[5] to achieve a maximum of 14 W of 532 nm light. After intensity stabilisation using an AOM[6] and fibre coupling into a photonic crystal fibre[7], we end up with up to 8 W at the setup that goes to the atoms. In this way, we achieve a high-power, fibre coupled source of 532 nm light with narrow linewidth, low intensity noise (see Fig. 3.5) as well as tunable power and frequency.

In the final setup, the green beam is outcoupled using an high-power collimation lens with $f = 30$ mm[8] while the infrared light comes directly from the initial source using a high-power fibre[9] and is collimated with a $f = 8$ mm doublet lens[10]. The two beams are then overlapped on a dichroic mirror before being sent to an evacuated aluminium box (see next section). Here, the beams are split on a 50:50 non-polarising

[3] Mephisto MOPA 42 W by Coherent
[4] ALS-IR-1064-50-A-CC by Azurlight Systems
[5] PPMgSLT by Oxide
[6] I-M110-2C10B6-3-GH26 by Gooch&Housego
[7] LMA-PM-15 by ALPhANOV
[8] HFTLSQ-20-30PY2 by Optosigma
[9] PMC-E-980-10.5-NA009-3-APC.EC-500-P by Schäfter-Kirchhoff
[10] 60FC-SF-4-M8-08 by Schäfter-Kirchhoff

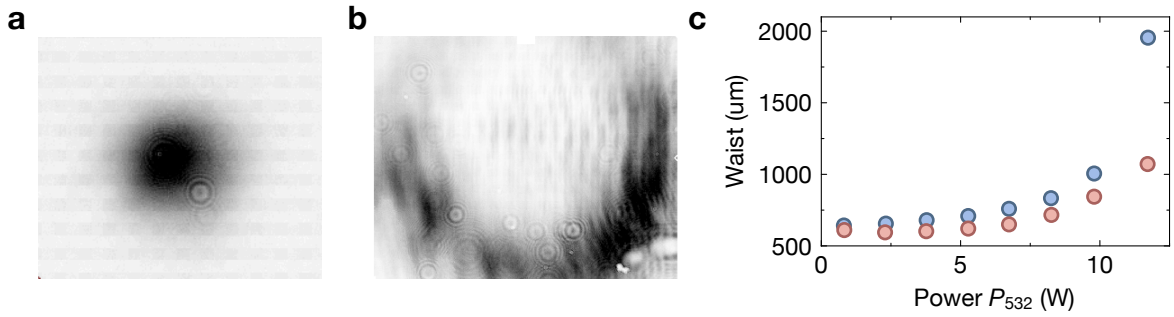

Figure 3.6: SHG beam degradation. **a** (**b**), Exemplary green beam profiles at low (high power). The waist as a function of power along the horizontal (blue) and vertical (red) direction is shown in **c**. Strong thermal lensing deteriorates the beam, mainly along the horizontal direction.

beam splitter[11]. One beam then travels through a delay line of 41.6 cm in the y-lattice as well as passes two glass plates[12] mounted on miniaturised rotation stages (galvanometers)[13]. In the end, both beams are focussed using $f = 500\,\mathrm{mm}$ lenses to achieve a waist of $w_0^{532} = 110\,\mu\mathrm{m}$ ($w_0^{1064} = 350\,\mu\mathrm{m}$). The beams interfere under a half-angle of 13.37° and enter the glass cell under an angle of 12.5° (25° for the x-lattice) from below to allow for further optical access in the plane of the atoms. All elements in the beam path are strictly UV-grade fused silica to avoid thermal lensing. To facilitate alignment, we have motorised mirrors[14] in both beams before the atoms as well as for overlap in both arms and right in front of the evacuated boxes.

Considering the waist at the position of the atoms, we can achieve lattice depths of up to $50\,E_\mathrm{R}$, which is enough to slow down tunnelling dynamics to below 0.1 Hz (where further suppression can be achieved using the superlattices). For a waist of $w_0^{532} = 110\,\mu\mathrm{m}$, we expect a harmonic deconfinement of $68 \times 2\pi\mathrm{Hz}$ for reasonable experimental parameters of $7\,E_\mathrm{R}$. Increasing the waist would require higher power to still achieve the same maximum depths. In our current setup this is limited by the second-harmonic generation and seems to be quite consistent between different setups and in the literature [207–209]. The main limitation are thermal problems within the doubling crystal. In addition to the significant absorption of the crystal at 532 nm, green-induced infrared absorption leads to heating of the crystal and therefore a change in refractive index. As the power of the 532 nm beam increases throughout the crystal, so does the thermal load. Therefore, the phase matching condition cannot be fulfilled at every point within the crystal. While this limits the power

[11] custom coating by Layertec
[12] $d = 3\,\mathrm{mm}$ by Laser Components
[13] U-624.03 by Physik Instrumente
[14] 8885 Piezo mirror mount by Newport and POLARIS-K05P2 by Thorlabs

that can be achieved, it turns out the first effect is a strong degradation of the outgoing beam profile from a very high-quality Gaussian profile, to a 'donut' shape, which makes high-efficiency fibre coupling impossible (see Fig. 3.6). This problem becomes more severe for longer crystals and highly depends on the precise design on the oven responsible for temperature stabilisation [210, 211]. In our case of a crystal with dimensions of $L \times W \times H = 30 \times 2 \times 0.5\,\mathrm{mm}$ as well as an oven surrounding the crystals on all sides, we have observed good beam profiles up to 14 W with most stable configurations running at around $10 - 11\,\mathrm{W}$. There are proposals that might allow for higher powers, even at lower fundamental power, by operating the system in a double-pass configuration [212]. Alternatively, coherent combination of multiple sources has been shown to realise higher powers as well [213]. For now, the available power in the simplified setup is enough for our current purposes.

An alternative pathway to minimise the harmonic confinement may be achieved by using elliptical beams. As evidenced in our vertical superlattice [150], increasing the waist along the relevant axis while decreasing it along less crucial directions allows for effectively lower harmonic confinement. For lattices along x and y, the vertical axis is less relevant as it does not contribute to the physical system[15]. While this is a valid approach, the bichromatic nature of the lattice makes a precise alignment of the focus along both directions non-trivial (in addition to the greater space requirements associated with further optical elements). For these reasons, we decided against elliptical beams in this design.

3.3.3 Mechanical design

General considerations

The mechanical design of the lattice setup is dedicated to achieve maximal stability, both in terms of pointing as well as absolute and relative phase stability. The beam path starting with the non-polarising beam splitter is encased in an evacuated aluminium box. In this manner, the residual fluctuations of the relative superlattice phase due to environmental changes in the delay line are minimised as only $\sim 15\,\mathrm{cm}$ are between the lattice box and the glass cell. Evacuation is achieved using a membrane pump[16]. We operate the pump continuously to avoid any drifts due to changing pressure, but make sure no vibrations from the pump are transferred via the tubes. To avoid drifts between the optics before and after the beam splitter, the evacuated box is mounted on a large aluminium base, that also contains the optics outside the box.

[15] The vertical confinement does however have an effect on our subsequent charge pumping for detection. After exchanging the lattices along x and y, we observe an increase in charge pumping fidelity compared to before due to the reduced vertical harmonic confinement.

[16] MP101V by Pfeiffer Vacuum

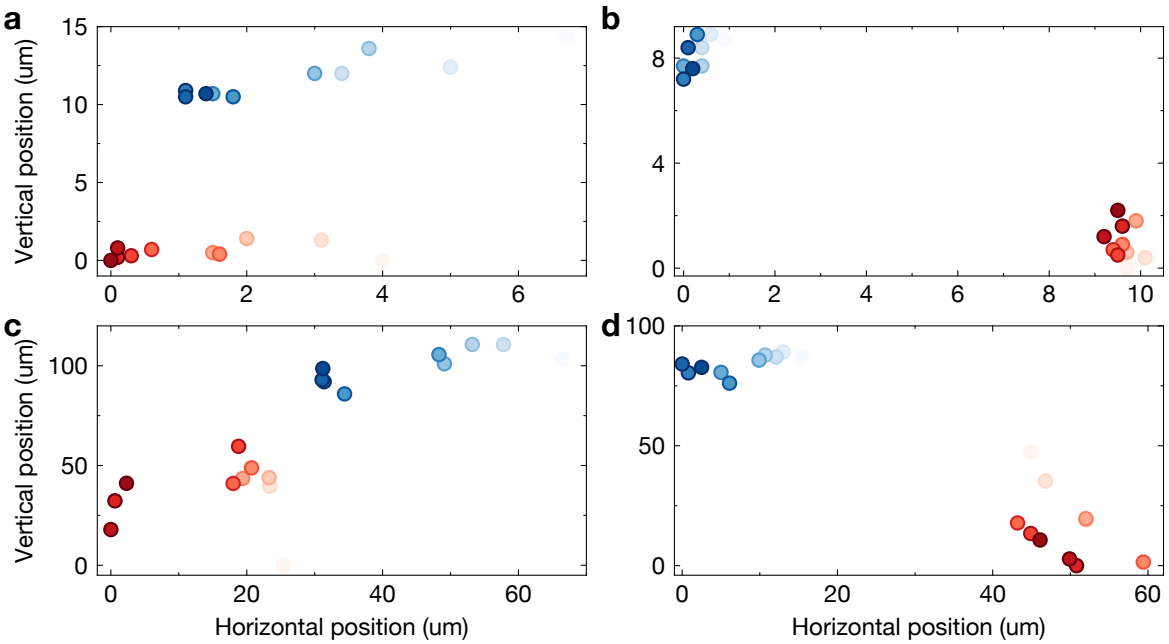

Figure 3.7: Misalignment due to evacuation. Beam movement due to repeated evacuation in x-lattice (**a**, **b**, two lattice beams respectively) and y-lattice (**c**, **d**, long and short arm respectively). Red markers are evacuated, blue markers are in atmosphere with similar shadings corresponding to subsequent iterations. The larger y-lattice box has stronger beam movement.

Both the base and the evacuated box have copper pipes inserted into the bottom which allow for the possibility of water cooling for improved temperature stability. Finally, for further stability, we minimise the number of optical elements and make sure that the only movable elements are motorised mirrors while all others are directly glued on their respective mount. Despite all this, misalignment of the lattices is possible. For fast and easy realignment after large movements, we place multiple reference cameras. As our glass cell is not anti-reflection coated, we can use this reflection and pick it up easily. After splitting on a dichroic mirror, the infrared and green beam are both sent onto a camera and their position noted. We placed the camera as far away as possible while still easily fitting the beams onto the camera chip.

Evacuation

During evacuation down to ~ 3.4 mbar, a misalignment of the setup is to be expected. We measure the repeatability and magnitude of this misalignment by monitoring the beam on a camera at the position of the atoms. We show the results in Fig. 3.7. It can be seen that the direction and magnitude of the shift is rather repeatable. The

magnitude is significantly larger for the y-lattice, as expected due to its longer beam path. In either case, the observed shifts on the order of $10 - 100\,\mu m$ can easily be compensated for with the motorised mirrors in the setup.

As mentioned before, both lattice setups sit below the height of the atoms such that the beams are angling upwards in the end. This allows for additional optical access in the atomic plane. Some optical elements are then placed directly on the lid of the box. To avoid huge changes when evacuating the boxes due to bending of the lid, it is made out of stainless steel. This allows evacuation with only minimal movement. Remaining misalignment is mitigated by appropriately placed reference cameras.

Absolute phase stability using Zerodur®

In the similarly designed vertical lattice, we found the absolute phase stability to be a significant challenge due to large drifts over short time scales caused by thermal changes. To avoid this issue, we attempted to isolate the crucial parts of the setup even more from the environment. While the evacuation already helps to reduce the impact from the surrounding air, the large linear thermal expansion coefficient of aluminium of $\alpha = 23.6 \times 10^{-6} \frac{1}{K}$ [214] still couples the system with the environment. This is only relevant in the delay line, where we are sensitive on lengths scales around the wavelength, i.e. on the sub-micron level. There are two ways to possibly circumvent this issue: we can either attempt to stabilise the temperature of the setup to a very high precision, or try to passively isolate it better from the surroundings. We again chose the passive solution to this problem. In this case, it means that aluminium is not the most suitable material to mount optics on. Other possibilities include stainless steel $\left(\alpha = 17.2 \times 10^{-6} \frac{1}{K}\right)$ [214], titanium $\left(\alpha = 8.6 \times 10^{-6} \frac{1}{K}\right)$ [214], Macor $\left(\alpha = 9.3 \times 10^{-6} \frac{1}{K}\right)$ [215], Invar $\left(\alpha = 1.2 \times 10^{-6} \frac{1}{K}\right)$ [216] and Zerodur® $\left(\alpha = 0 \pm 0.1 \times 10^{-6} \frac{1}{K}\right)$ [217]. We decide to use Zerodur® (as patented by Schott AG), which is a glass ceramic material that has a thermal expansion coefficient consistent with zero. It is commonly used as a substrate in high-precision lithography or as a mirror material in large astronomical telescopes [218]. It has also been successfully used for full optical setups in cold atomic experiments on the international space station [219, 220]. One disadvantage compared to e.g. aluminium is the more limited machining options. For our application, we do not design every individual mount and element out of Zerodur®, but instead only prepare a Zerodur® base where the individual aluminium mounts are mounted on. This already serves our purpose as the Zerodur® serves as an insulating, non-expanding layer between the aluminium box and the optical setup, such that the precise delay line length stays constant.

To test this application, we directly compare a Zerodur® with an aluminium test setup (see Fig. 3.8a). We use a Michelson interferometer and create interference fringes on a camera using a 1064 nm laser. A sketch of the setup and the resulting fringes is

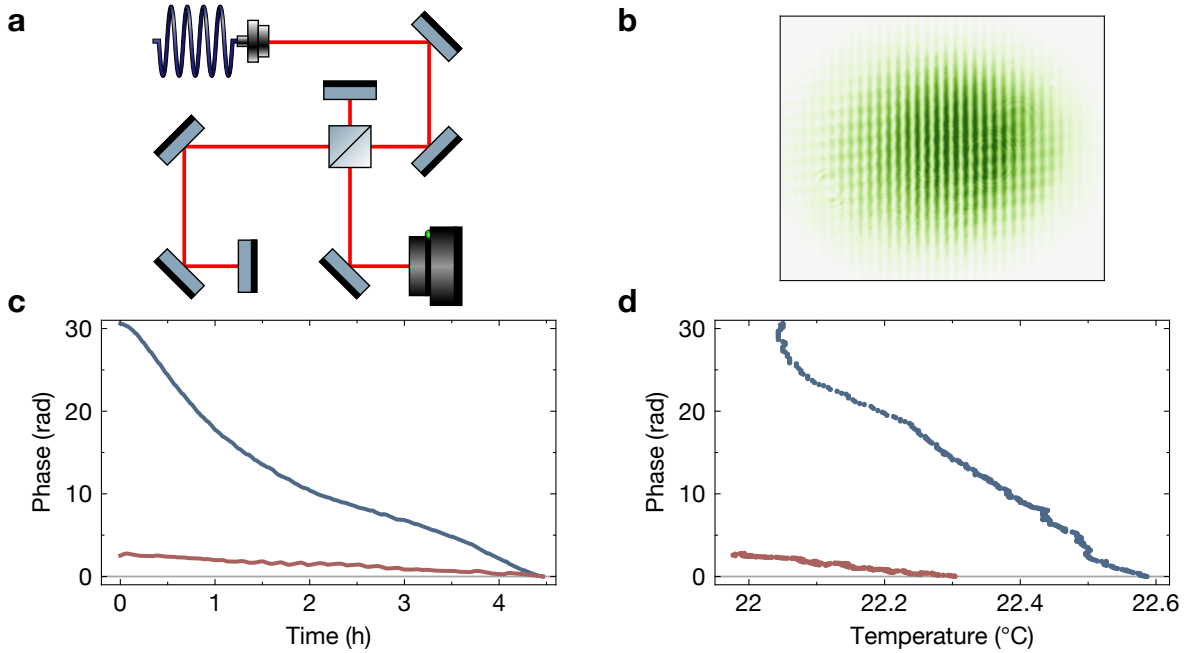

Figure 3.8: Interferometric phase for different materials. **a**, Schematic setup to compare stability of a setup built on aluminium compared to Zerodur. **b**, Measured interference fringes on camera. **c**, Measured phase over time in interferometer setup built on aluminium (blue) and Zerodur (red) base. The drift is far reduced in the Zerodur setup. The correlation between phase and temperature is shown in **d**, with both cases showing clear correlation but much stronger dependency for aluminium.

shown in Fig. 3.8b). We build two identical setups, once on aluminium and once on Zerodur®, and measure for both setups the position of the interference fringes as well as the temperature of the base. We show the resulting measurement in Fig. 3.8c, d. The observed drift is about one order of magnitude stronger for aluminium compared to Zerodur®. Furthermore, the correlation between the phase and temperature is significantly stronger for aluminium. We emphasise that the setup is not evacuated such that observed drift in the case of Zerodur® can also be attributed to changes in air temperature and pressure.

Due to the mentioned limited machinability of Zerodur®, the optical mounts cannot be fixed with screws as no threads are available. Therefore, all mounts are instead glued on the Zerodur® base. For a more detailed study of the glueing process we refer to [220]. Here, we use the UV curing optical adhesive NBA107. The main advantage of this adhesive is its fast curing properties as well as the relative ease with which components can be removed again without damaging them. To facilitate the glueing procedure, a mask was manufactured which referenced all elements with respect to

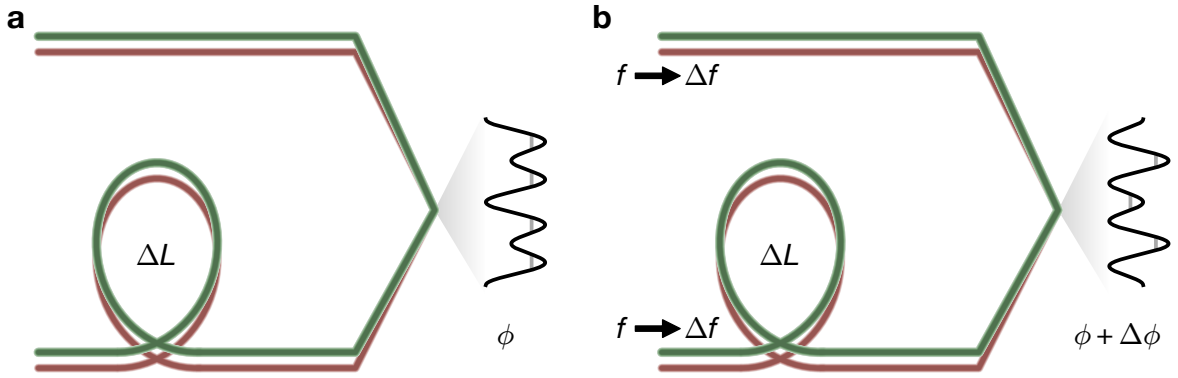

Figure 3.9: Delay line principle. Two beams are interfered under an angle to generate a superlattice. By changing the frequency of the green lattice beams by Δf, traversing through an additional delay line of length ΔL in one arm changes the relative superlattice potential by $\Delta\phi$.

the Zerodur® base. Then, glueing was performed while aligning a beam throughout the setup. Due to the limited number of degrees of freedom, this is very helpful to position elements with sufficient precision. After glueing, the mask was removed from the setup. While in our case, the stability of the components turned out to be sufficient, it is possible to add additional, vacuum-compatible slow-curing glue such as Torr Seal®. Furthermore, the Zerodur itself also cannot be fixed inside the aluminium box using screws. Instead, we use Viton® pads that are fixed on the bottom of the Zerodur plate and set into small indentations in the aluminium box.

3.3.4 Tunability

Precise tunability of the relative superlattice phase is essential in setting the desired couplings within the system. Here, we use two separate, complementary approaches: a combination of frequency shifting and a delay line is used for fast phase control while a rotatable glass plate acts as a wider range, slow phase changing element.

Frequency shifting and delay line

As described above, the frequency change occurs in the seed of the amplifier used for second-harmonic generation. We use two acousto-optic deflectors[17] in a double-pass configuration in series to realise large frequency shifts. Each AOD has a bandwidth of 130 MHz within which a deflection efficiency of above 60 % can be reached. Therefore, starting with about 400 mW of power at 1064 nm, we can ensure $30 - 50$ mW

[17] AOD 4225-2 by Gooch&Housego

as a seed for the amplifier. For more details on the setups, see also [150]. The total frequency shift of the 532 nm light is therefore $2 \times 2 \times 2 \times 130\,\mathrm{MHz} = 1.04\,\mathrm{GHz}$ where an additional factor of 2 is won due to the frequency shift happening before the second-harmonic generation.

By applying a frequency change of Δf in addition to a traversed optical path of length L, the corresponding phase shift is

$$\Delta\phi = kL = \frac{\pi n \Delta f}{c} L. \tag{3.3}$$

The desired phase range depends on the application. For most cases, the minimal range is given by the possibility to access to the full range of symmetric to antisymmetric superlattice potential, i.e. a range of $\pi/2$. In some cases, a larger range is useful as simultaneous access to two separate symmetric phase configurations may be required (e.g. in the charge pumping protocol of our vertical lattice, see section 2.4.3). In that case, at least a range of π is necessary, although that depends on the precise position of the symmetric phase configuration within the phase range. Without any further control over the relative superlattice phase, in order to be sure to have two such configurations, a phase range of 2π is needed. These values translate into the length of the delay line. In our case, we settled for a length of $L = 41.6\,\mathrm{cm}$ for the y-lattice, while for the x-lattice, the delay line is only 4.2 cm long (and thus negligible) due to lack of space in the experimental setup. This realises a total phase range of 1.4π for the y-lattice.

Electronics for phase control

With the AODs, the control of the phase of the y-lattice is effectively a change in frequency. Therefore, a fast and high-quality RF frequency source is required. First, the linewidth of the RF source has to be narrow in order to not add phase noise, which is directly transferred from frequency noise. For the numbers given above for the y-lattice, to achieve phase noise below 1 mrad, a linewidth of less than 30 kHz is needed. Furthermore, this source must never fully turn off, even when changing frequencies as this would interrupt the seed of the following amplifier. However, many commercial frequency sources are not able to provide uninterrupted output over the desired frequency range of $150 - 300\,\mathrm{MHz}$. We here use a direct digital synthesizer (DDS)[18] which fulfils our requirements. It provides RF signals up to 400 MHz at 1 GS/s with a linewidth of $< 10\,\mathrm{kHz}$. We can either directly program the desired ramps, or use the analog input to control the phase directly via our experimental control system. Using the analog input control option increases the linewidth by a factor of two, which is still narrow enough to not significantly impact the phase stability.

[18] Flex-DDS-NG by Wieserlabs

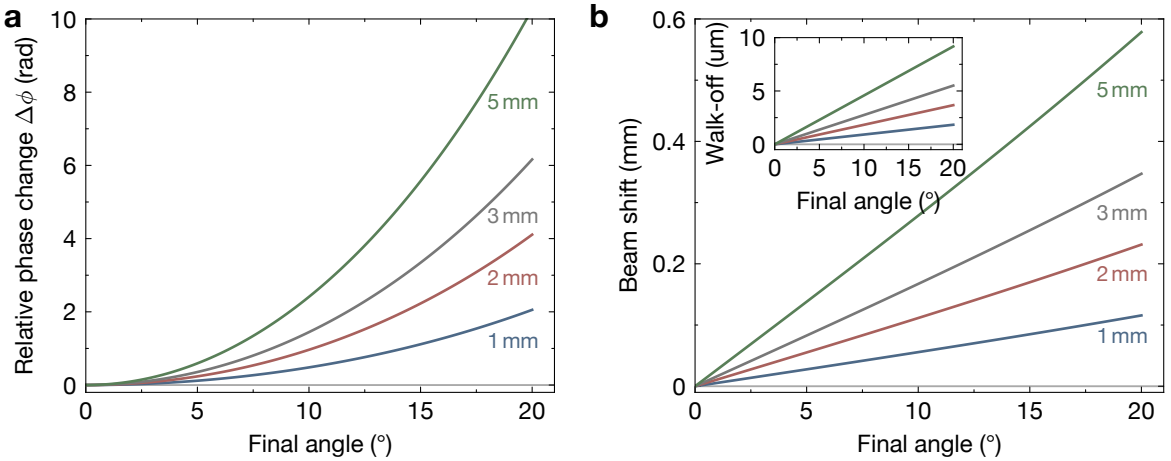

Figure 3.10: Superlattice tuning with rotatable glass plate. **a**, Change in relative phase after rotation from normal incidence to a given final angle for glass plates of thickness 1, 2, 3 and 5 mm respectively. **b**, Corresponding beam shift of a 532 nm beam as a function of final angle after rotation from normal incidence, showing the required compensation. The inset depicts the offset between the two beams.

Galvanometric phase control

In a situation, where spatial constraints do not allow for a delay line (such as for our x-lattice), alternative solutions for the control of the relative superlattice phase are required. One possibility is a rotatable glass plate inserted into the beam [221]. Due to the different refractive indices for the 532 nm and 1064 nm beam, the optical path length through the material differs. When rotating the glass plate, the path length changes for both proportionally and therefore induces a change in the relative phase of the superlattice. More specifically, for a glass plate of thickness d with refractive index n_λ and incidence angle α for both beams (with wavelengths λ_L and λ_SL), the optical path length behaves as

$$L_\lambda = d/\cos(\arcsin(\sin(\alpha)/n_\lambda)). \tag{3.4}$$

The corresponding phase shift when rotating to an angle α from normal incidence is then

$$\Delta\phi = \frac{\pi}{\lambda_\mathrm{L}}\left[n_{\lambda,\mathrm{L}}(L_{\lambda,\mathrm{L}} - d) - n_{\lambda,\mathrm{SL}}(L_{\lambda,\mathrm{SL}} - d)\right]. \tag{3.5}$$

The corresponding relative phase shift for different plate thickness d is shown in Fig. 3.10a. By appropriately choosing the initial incidence angle as well as the thickness d, the sensitivity and range can be set. However, not only the relative superlattice phase is affected, but also the position of the beam (see Fig. 3.10b). These movements are rather large and have to be compensated for. By using two glass plates that rotate

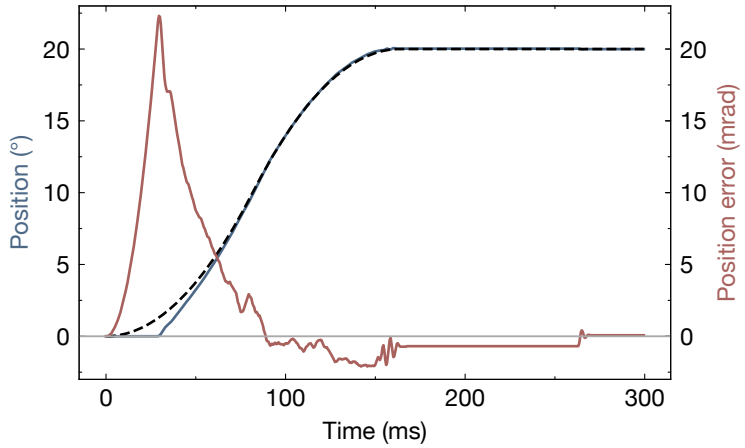

Figure 3.11: Galvanometer for coarse phase control. Positional error after galvanometer movement. The set position is shown in the dashed black line, the actual position in blue and the corresponding error in red. After movement by 20 °, it takes ca. 25 ms for it to react and in total more than 250 ms until it has finally settled.

in opposite directions, the positional shift can be compensated for, while the phase shift adds up from both elements.

For our purpose, we use glass plates with $d = 3\,\mathrm{mm}$, mounted on galvanometers by Physik Instrumente. We choose these devices based on their exceptionally small size of $30 \times 30\,\mathrm{mm}$ in conjunction with the very high precision of movement. They are able to rotate by more than 360 ° with a maximum velocity of $720\,^\circ/\mathrm{s}$. The specified sensor resolution is 35 µrad with an incremental motion of 105 µrad, while the bidirectional repeatability is specified for $\pm 210\,\mu\mathrm{rad}$. This would correspond to a precision for the relative phase of $\sim 5\,\mathrm{mrad}$. The main disadvantage of using this method for phase control is due to its slow speed on the order of 100 ms. We show the recorded movement of the galvanometer in Fig. 3.11. First, there is a significant delay of the movement with respect to the set point signal of 25 ms. However, this delay turns out to be very repeatable such that it can effectively be partially mitigated by sending the signal at an appropriate earlier time. However, the final error is usually still on the order of 175 µrad and it takes about $180 - 200\,\mathrm{ms}$ to to settle to its final position. For these reasons, this method is significantly worse than using a delay line in terms of speed and precision and prevents dynamic tuning of the phase during the experimental sequence. But, as it is able to provide arbitrarily large phase shifts with minimal size, it can be used in situations with very little available space. Ideally, using it in conjunction with a delay line allows for a shorter delay line.

3.4 Characterisation

3.4.1 Preparation and temperature

Before characterising the specific properties of the superlattice potential as it is unique to this setup, we first make sure that the general preparation scheme works at least as well as before the change in lattice. For this, the relevant observables are the on-site charge fluctuations (such that a Mott insulator is formed) and spin-spin correlations. As the new, bichromatic lattices are blue-detuned, our preparation scheme had to be adjusted to account for the different confining potentials. We start with a cold cloud in a single plane of a vertical lattice that is confined in-plane by a crossed dipole trap. At this point, we load from the harmonic dipole potential into a repulsive, box-like potential projected using a DMD. This potential is already adjusted for the final parameters we require after loading into the lattice. We hold in this potential for 1 s. Then we ramp up the lattices within 200 ms to their final parameters. The DMD potential is set up such that a flat, central region is surrounded by a reservoir with $\sim U/2$ higher chemical potential and then a barrier that is several U high. The transition between these regions is smoothed to avoid sharp edges that might introduce additional fluctuations or instabilities. The resulting density profile and on-site fluctuations are

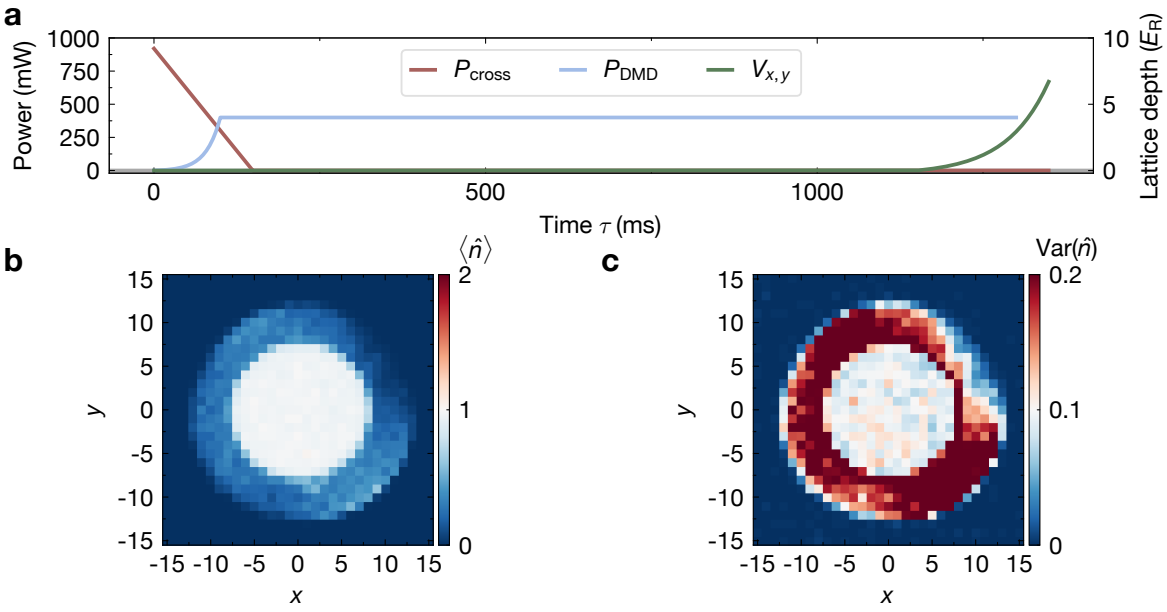

Figure 3.12: Preparation of low-entropy Mott insulators. **a**, Preparation sequence from atoms in a 2d plane into the final 2d lattices. **b**, Resulting density profile and **c**, on-site fluctuations at $U/t = 6.5(2)$.

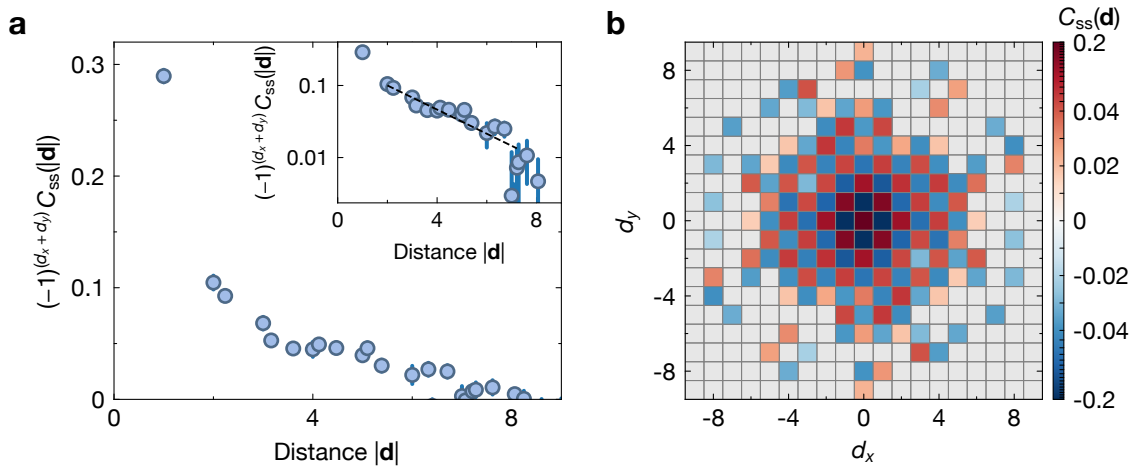

Figure 3.13: Spin-spin correlations. **a**, Sign-corrected spin-spin correlations as a function of distance $|d|$ at half filling. A fit to QMC data (solid line) reveals temperatures of $k_B T/t = 0.249(3)$. The inset shows the same data logarithmically to extract the correlation length $\xi = 2.6(3)$ (dashed line). **b**, Spin-spin correlation map showing symmetric couplings in the system. Distances where correlations are consistent with zero are not shown.

shown in Fig. 3.12 at half-filling and $U/t = 6.5(2)$. We achieve on-site fluctuations as low as 0.09. This shows the high-fidelity preparation of a Mott insulating state that is required for most of our experiments.

To ensure that there is no excessive heating present in the system, we study spin correlations at half filling at $U/t = 6.5(2)$ by performing the spin detection technique as described in Ch. 2. We define the spin correlator $C_{ss}(\boldsymbol{d})$ as

$$C_{ss}(\boldsymbol{d}) = \frac{1}{\mathcal{N}_{\boldsymbol{d}}} \sum_i \frac{\langle \hat{S}^z_{\boldsymbol{i}} \hat{S}^z_{\boldsymbol{i}+\boldsymbol{d}} \rangle - \langle \hat{S}^z_{\boldsymbol{i}} \rangle \langle \hat{S}^z_{\boldsymbol{i}+\boldsymbol{d}} \rangle}{\sigma(\hat{S}^z_{\boldsymbol{i}}) \sigma(\hat{S}^z_{\boldsymbol{i}+\boldsymbol{d}})}. \tag{3.6}$$

The resulting spin correlations are shown as a function of distance in Fig. 3.13. We find correlations extending up to 8 sites with a characteristic correlation length of $\xi = 2.6(3)$ sites. By comparing to quantum Monte Carlo simulations, we extract a temperature of $k_B T = 0.249(3)\, t = 0.405(5)\, J$, which is consistent with the lowest temperatures achieved in fermionic quantum simulators using optical lattices [64].

3.4.2 Stability

Due to the large amount of experimental realisations required to extract precise higher-order correlation functions, stability both on short as well as long timescales is of utmost important in the design of optical lattice setups. Here we will summarise the

resulting stability of beam pointing as well as the phase stability of the new bichromatic setup.

Pointing and alignment

The limited size of the lattice beams due to the available power leads to a high degree of precision required in alignment. Misalignment will increase the harmonic deconfinement and move it away from the centre of the system as defined by the DMD. Therefore, beam alignment based solely on lattice depth is not precise enough for our purpose. Instead, we prepare a large circular cloud of atoms and add only individual lattice beams (such that no lattice is formed). The anticonfinement of the individual beams forms a hole in the atomic cloud that we centre with respect to the DMD where we are sensitive on positional mismatch on the order of one lattice site. This procedure is repeated for every lattice beam and usually does not impact the overall depth of the lattice at all. Due to the available motorised mirrors, the whole alignment can be executed with high precision within about one hour. Usually, in continuous operation, alignment is conserved for several days up to one week. which allows for long, uninterrupted measurements.

Relative phase stability and tunability

One main reason for a bichromatic superlattice design is the inherent, passive stability of the setup as described in section 3.3. Here, we investigate the resulting stability of the relative superlattice phase. For this purpose, we load into isolated double-wells with $V_x = 40(2)\,E_\mathrm{R}$, $V_y = 11.0(5)\,E_\mathrm{R}$ and $V_y^\mathrm{SL} = 31(1)\,E_\mathrm{R}$ such that $t_y = h \times 518(76)\,\mathrm{Hz}$. We set the chemical potential to achieve a filling of $\langle \hat{n} \rangle \approx 0.75$, i.e. slightly above one atom per double-well. By varying the phase using the frequencies of the AODs, we are able to realise different geometries (see Fig. 3.14a): for $\phi < 0$ or $\phi > 0$, we have imbalanced double-wells, which lead to only one of the wells being populated. For $\phi = 0$, the double-well is symmetric and both wells are populated equally. We calculate the normalised imbalance between the two wells as $\mathcal{I} = (\langle \hat{n}_\mathrm{L} \rangle - \langle \hat{n}_\mathrm{R} \rangle)/(\langle \hat{n}_\mathrm{L} \rangle + \langle \hat{n}_\mathrm{R} \rangle)$, where $\hat{n}_{\mathrm{L/R}}$ is the population in the left/right part of the double-well, and plot it as a function of phase ϕ in Fig. 3.14b. Here, we postselect on a specific total population per double-well with one atom per double-well shown in blue and two atoms per double-well in red. For singly occupied double-wells, only the lower well has finite populations for $\phi \neq 0$. Only in a narrow phase regime around $\phi = 0$, both wells are equally populated. Away from the symmetric configuration, we find an average imbalance of $\mathcal{I} = 0.985(2)$ for $\phi \geq 50\,\mathrm{mrad}$. The solid line corresponds to theory calculations for a two-site Fermi-Hubbard model without free parameters. When considering double-wells with two atoms, interaction effects play a role. We set the interactions to $U = h \times 7.7\,\mathrm{kHz}$ at $\phi = 0$. As a result, the detuning between the

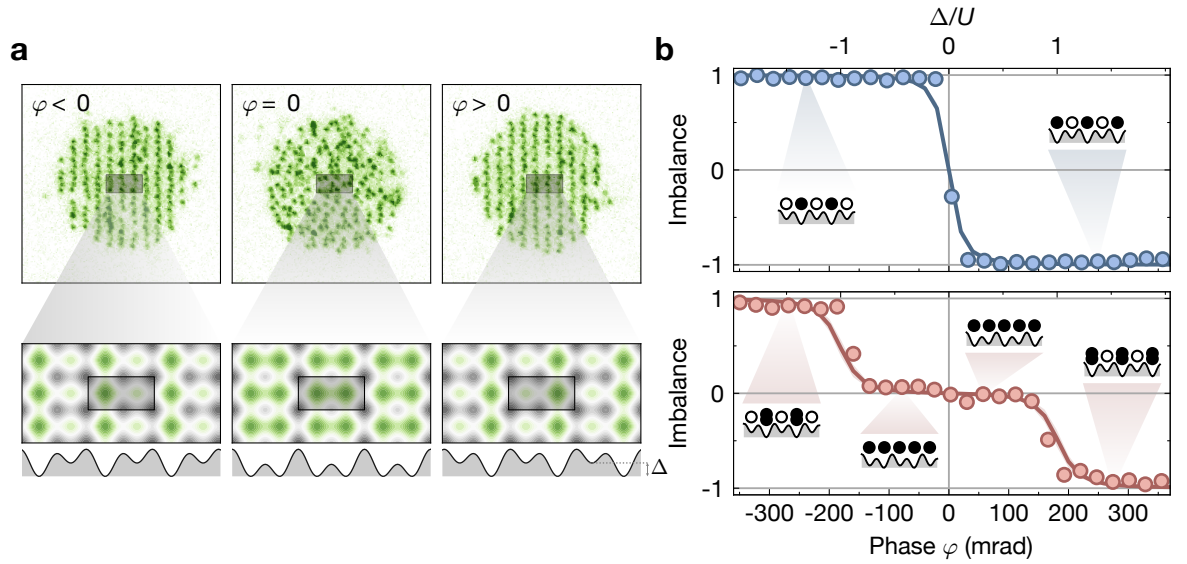

Figure 3.14: Double-well preparation using a superlattice. **a**, Single-site resolved fluorescence images for different lattice potentials. For $\phi < 0$ and $\phi > 0$, lattices are isolated on one part of the double-well with balanced occupations at $\phi = 0$. The corresponding lattice potentials are shown below. **b**, Imbalance between different parts of a double-well as a function of relative superlattice phase ϕ and thus detuning Δ/U. For one atom per double-well, there is a sharp transition around the symmetric phase, while for two atoms, there is a plateau due interaction effects. Ground state theory calculations are shown in solid lines.

wells first needs to overcome the interaction energy U before both atoms can occupy the same well. This leads to a plateau around $\phi = 0$ whose width corresponds to $\pm U$. Again, theory calculations agree well with our obtained data. We commonly use this measurement for a precise calibration of the relative superlattice phase.

We perform a long-term measurement on the relative superlattice phase to determine its stability. For this, we extract the exact symmetric phase from the measurement as stated above and track it over time (see Fig. 3.15). We find a small, slow drift of about $2.0(1)\,\mathrm{mrad/h}$, consistent over several measurement. We do not find any correlation between this drift and the table temperature, humidity or beam position, such that at this point, the exact origin of this drift is unknown. Fortunately, we can easily compensate for this drift by using this kind of measurement as a short calibration that can be executed in less than three minutes.

Finally, we investigate shot-to-shot fluctuations of the relative superlattice phase by measuring solely at $\phi = 0$ and tracking the imbalance as a function of time (see Fig. 3.16). In addition to the slow drift observed in Fig. 3.15, we observe fluctuations

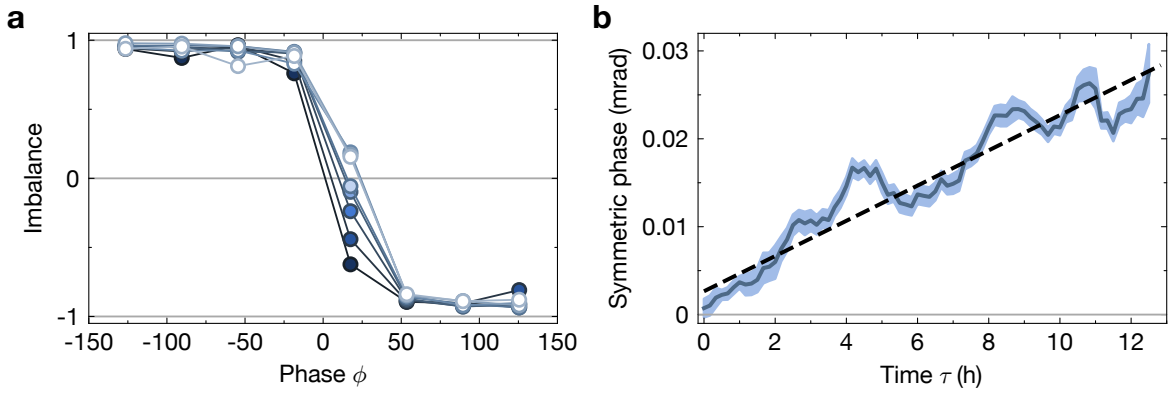

Figure 3.15: Superlattice phase drift. a, Imbalance as a function of phase for different subsequent measurement times to extract symmetric phase. **b**, Symmetric phase as a function of time as extracted from **a**. A linear fit (black dashed line) with a slope of $2.0(1)$ mrad/h is consistent with the observed drift.

in individual realisations. By comparing these imbalance fluctuations to the slope of the full phase scan, we can estimate the corresponding phase fluctuations. After subtraction of the overall drift, we estimate fluctuations of 5 mrad. This is far below the requirement for spin-resolved detection as well as many applications in double-well Fermi-Hubbard physics (see section 3.2). The superlattices in use in earlier iterations of our experiment were significantly worse with a short-term stability of $53(4)$ mrad (in addition to strong long term drifts) [141]. Similar bichromatic setups in previous experiments using retro-reflected superlattices reported relative phase stabilities of 9 mrad [222] (14 mrad [223]). More recent work for bichromatic superlattices for bosonic systems also demonstrated a stability of 9 mrad [224]. For tunable lattices in other geometries, good passive stability using a reduced number of beams has been achieved. For a folded, tunable lattice, $31(3)$ mrad have been achieved [188] while for a multi-frequency lattice, stabilities as low as 3 mrad have been reached [186].

In addition to controlling the relative superlattice phase via the frequency of the lattice beams, we can also tune it using the rotatable galvanometer glass plates. We calibrate the glass plates by performing phase scans using the AODs to determine the symmetric phase configuration and repeat this for different galvanometer angles (see Fig. 3.17). We observe the expected quadratic relation between the galvanometer angle and the symmetric phase and calibrate the absolute galvanometer angle by using only this angle as a free parameter in the fit (dashed line in Fig. 3.17b).

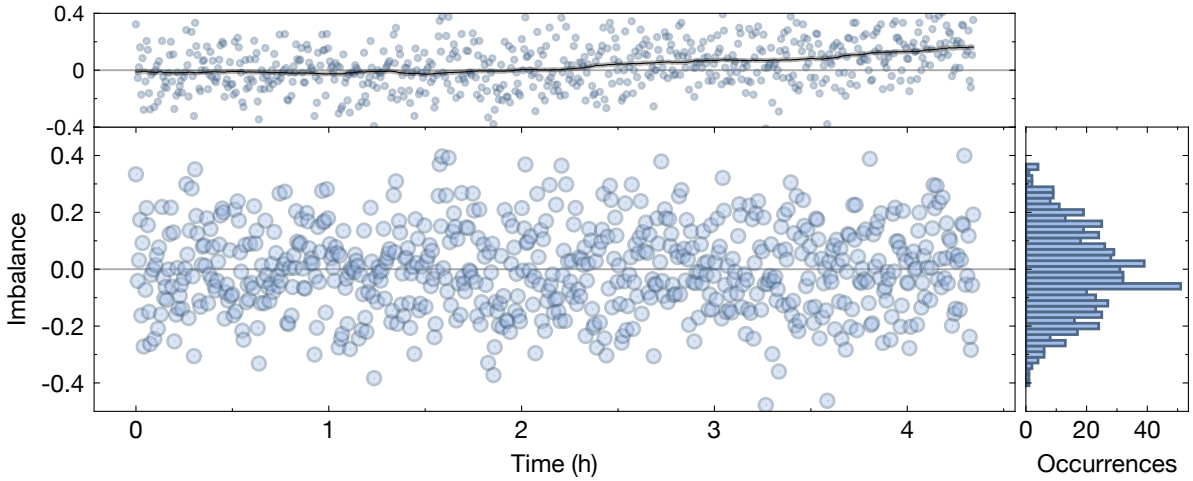

Figure 3.16: Shot-to-shot phase fluctuations. Imbalance at $\phi = 0$ as a function of time. The top plot shows the bare data with the black line indicating the running average over one hour where the overall drift is visible. We subtract this drift from the individual data points in the main part. The right bar plot shows a histogram of individual realisations where the width of the histogram is given by a standard deviation of 0.15 which corresponds to 5 mrad.

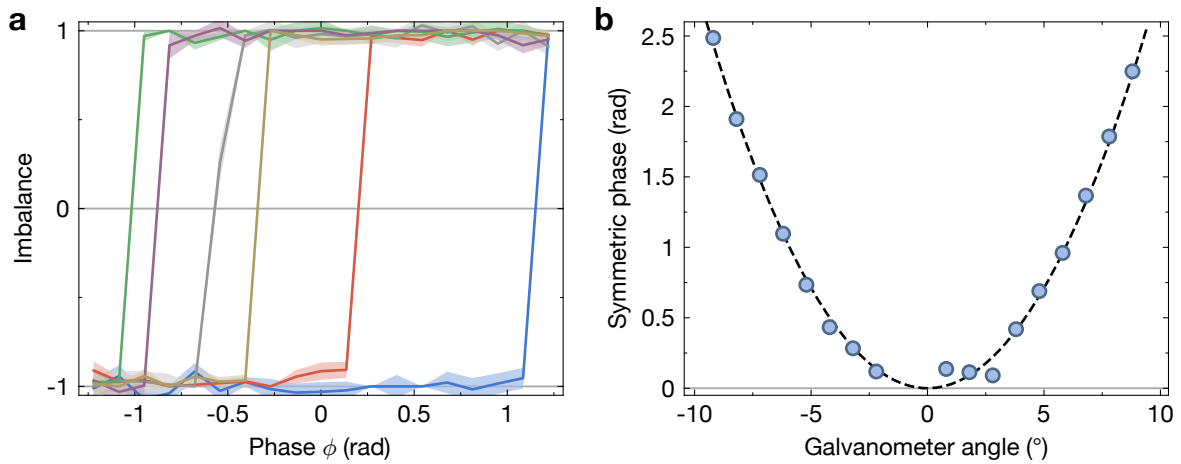

Figure 3.17: Relative phase control with galvanometer. **a**, Scans of the relative superlattice phase ϕ using the applied AOD frequency for various angles of the galvanometers. We extract the symmetric phase, where the imbalance goes to zero and show the result as a function of galvanometer angle in **b**. The dashed line is a theory prediction with only the absolute angular offset as free parameter.

Absolute phase stability

Not only the relative superlattice phase stability but also the absolute phase stability can be highly relevant for specific experiments. This is most crucial when addressing individual sites or small scale structures using the DMD. Drifts of the absolute lattice phase with respect to the DMD will then move patterns from their intended position, changing preparation or addressing procedures (as e.g. in the case of quantum walks, see section 3.4.3). We assume that drifts of the DMD are usually small as the projection via the objective grants inherent positional stability. We track the absolute phase of the lattices as a function of time in Fig. 3.18. The observed drifts occur over several hours and are below 0.2 lattice sites. This is more than precise enough to have well defined edges in most experiments where no additional small scale structures are implemented. For single-site addressing, the slow timescales of the drift make feedback procedures straightforward to implement. By tracking the absolute phase of the lattice, the position of the DMD can be adjusted continuously to follow the lattice phase.

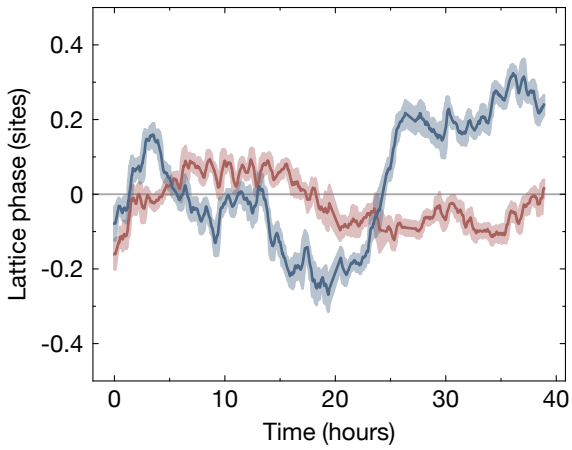

Figure 3.18: Absolute phase stability. Extracted lattice phase along x (blue) and y (red) over two days. Slow drifts are smaller than 0.2 lattice sites.

3.4.3 Quantum walks

The homogeneity of the lattice potential can have significant impact on the resulting physics as small disorder may change the preferred ground state [225]. Density measurements will only be sensitive on the of the interactions U for half-filled systems and on the order of the tunnelling energy t for doped systems. To be precise on lower energy scales, we here study time-resolved dynamics in quantum walks where we are sensitive down to the superexchange energy J.

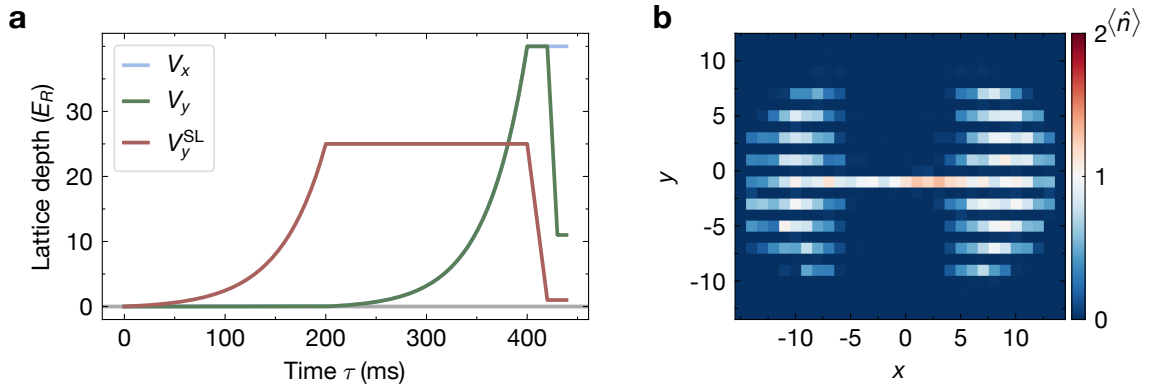

Figure 3.19: Preparation for quantum walks. **a**, Lattice ramps for quantum walk preparation with variable final superlattice power and final holding time. **b**, Resulting atomic density, with reservoirs on either end that are neglected in the analysis.

We investigate the single- and two-particle time evolution in different 1d superlattice potentials. For this purpose, we prepare a single decoupled line of atoms along x, which we will then subsequently release and observe the evolution along y. To prepare a single line of atoms with at most one atom per chain, we make use of the superlattice potential along y by loading into a deep lattice with $V_{x,y} = 40(2)\,E_\mathrm{R}$, $V_y^\mathrm{SL} = 25(1)\,E_\mathrm{R}$. We set the phase to the antisymmetric configuration $\phi = \pi/2$, where we achieve the highest nearest-neighbour potential offset for a given lattice depth. By combining this with our DMD potential, we can load into a single line of atoms with high fidelity with lower requirements on the addressing resolution of the DMD (see Fig. 3.19). Starting from this situation, we quench the lattice potential along y within 1 ms to a given final configuration at time $\tau = 0$ and observe the dynamics as a function of time.

Single-particle, flat lattice

We first consider a flat lattice, without any additional superlattice potential. By ramping to $V_y = 11.0(5)\,E_\mathrm{R}$, we arrive at a tunnelling rate of $t = h \times 98(11)\,E_\mathrm{R}$, governing the time scales of the observed dynamics. We show the resulting measurements in Fig. 3.20a where we postselect the data on a occupation of exactly one atom per chain. We compare this to theory calculations using ED in Fig. 3.20b. While for short times we observe excellent agreement with theoretical calculations, for later times the experimental density distribution becomes asymmetric with a centre of mass drift towards negative positions. This is caused by a combination of the harmonic deconfinement due to the Gaussian envelope of the individual lattice beams and an offset of this confining potential with respect to the centre of the system. The latter is dependant on the instantaneous alignment of the lattice beams and may thus be optimised. The

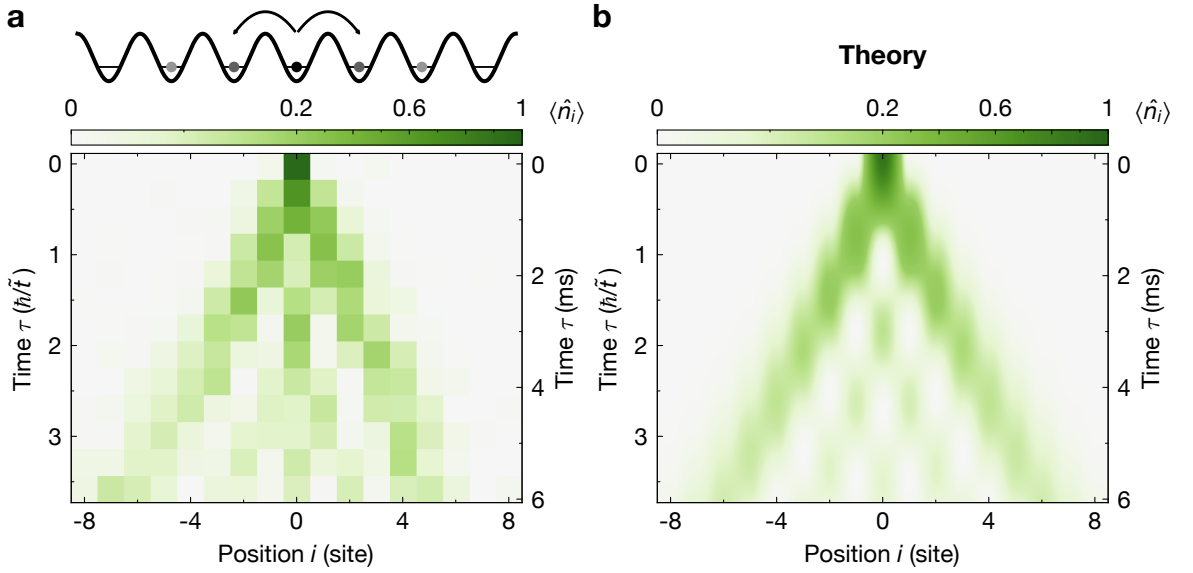

Figure 3.20: Single-particle quantum walk. **a**, Density distribution as a function of time for the evolution after initialisation of a localised state at $i = 0$ at $\tau = 0$. The delocalisation follows the timescale of the tunnel coupling $\tilde{t} = t$. We observe good agreement with ED calculation in **b**.

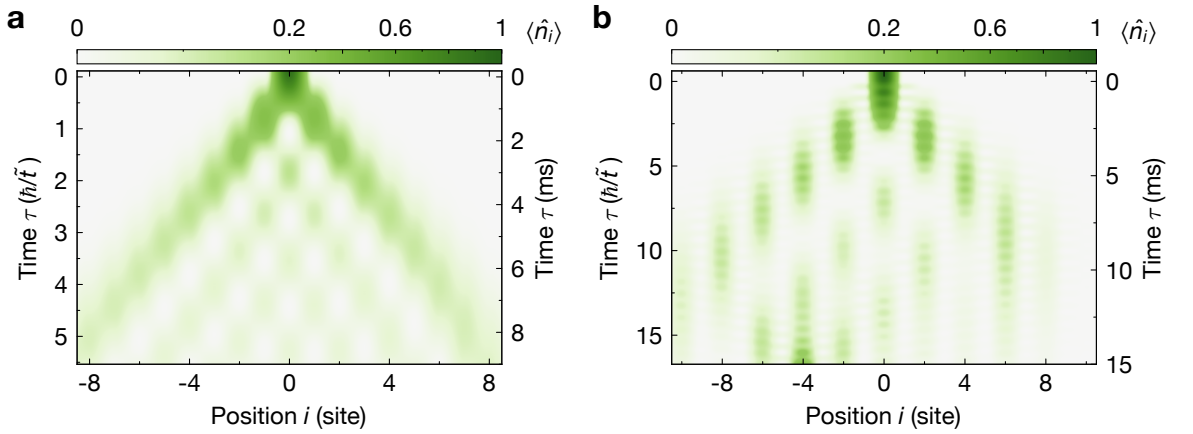

Figure 3.21: Simulated single-particle quantum walk with harmonic confinement. **a**, Calculated density distribution as a function of time for the evolution after initialisation of a localised state at $i = 0$ at $\tau = 0$ with added harmonic confinement and positional offset. **b**, Staggered quantum walk with harmonic confinement and offset.

overall harmonic confinement can be reduced by reducing the depth of the lattice and thus the confinement. We include this harmonic contribution in our calculations in

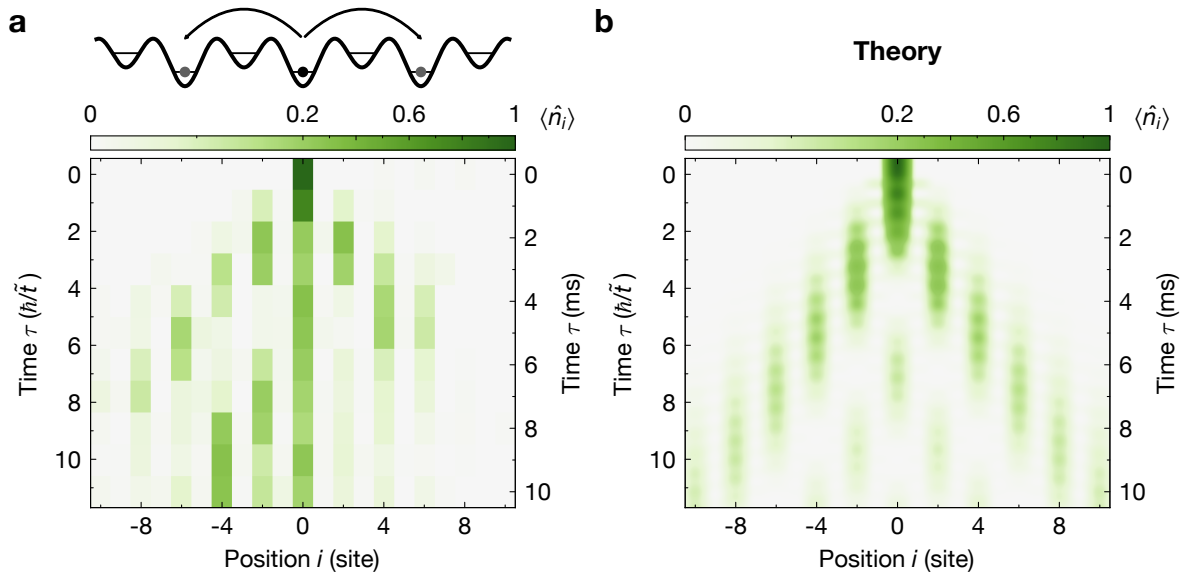

Figure 3.22: Single-particle quantum walk in staggered lattice. **a**, Density distribution as a function of time for the evolution after initialisation of a localised state at $i = 0$ at $\tau = 0$ in a staggered potential. Next-nearest-neighbour hopping allows for delocalisation despite detuning at nearest distances. We observe good agreement with ED calculation in **b**.

Fig. 3.21a. We observe qualitative agreement for a confinement of $83 \times 2\pi$ Hz and an offset of approximately two lattice site. This measurement shows that there is no local disorder on the order of t within the lattice potential and only global confinement due to the Gaussian envelope.

Single-particle, staggered lattice

We then add the staggered potential to study the evolution of of a single particle in a superlattice potential. We work in a final configuration with $V_y = 6.0(3)\, E_\mathrm{R}$, $V_y^\mathrm{SL} = 1.00(5)\, E_\mathrm{R}$. This leads to nearest-neighbour tunnelling rates of $t = h \times 327(25)$ Hz. However, the staggered potential leads to local detunings of $\Delta = h \times 1.38(14)$ kHz, such that $\Delta/t \gg 1$ and therefore nearest-neighbour hopping is far detuned and thus suppressed. Meanwhile, the site at distance 2 is again resonant with the initial site such that tunnelling via an intermediate state is possible as a second-order order process. The corresponding amplitude of this process follows $t^{(2)} = t^2/\Delta$. The effective tunnelling rate to next-nearest-neighbouring sites is then a combination of this second-order hopping effect and the direct next-nearest-neighbour tunnelling t', as a result of the residual overlap of the Wannier functions. Whether these two have the same or opposite sign depends on whether one considers the tunnelling process be-

tween sites with higher or lower energy which will then consequently either sum with identical (upper) or opposite (lower) signs. In either case, the delocalisation of the particle is restricted to a single sublattice. As we prepare our system in the lower well, the total tunnelling rate to the same sublattice is then $\tilde{t} = t^2/\Delta - t' = h \times 65(20)\,\mathrm{Hz}$.

We show the experimental results in Fig. 3.22a, with theory calculations again in b. We observe the expected delocalisation over a single sublattice across several sites. As in the case of the quantum walk in a flat lattice, delocalisation over longer times is limited due to the harmonic confinement. Most importantly, the energy scales of this process are much lower than before. Instead of the nearest-neighbour tunnelling rate t, the import energy scale is here only a bit above what would be the superexchange energy $J = 4t^2/U$ (as $U \approx 4.7\,\mathrm{kHz}$). As we observe coherent time evolution over many hopping events, another upper bound on possible local inhomogeneities is placed. We include the harmonic confinement of $72 \times 2\pi\,\mathrm{Hz}$ into the ED calculations in Fig. 3.21b, which is consistent with the result obtained before. The fast oscillations visible in theory are due to off-resonant tunnelling to the other sublattice, which is not seen in the experiment due to the lower time sampling rate.

Two-particle, staggered lattice

Finally, we can extend the quantum walks by considering the case, where more than a single particle is prepared initially. If there is no superlattice present in the system, the doublon will only delocalise as a single, bound object [226] with a reduced rate compared to the single-particle tunnelling rate. Adding a superlattice potential, however, offers up more possibilities. In general, the motion of the doublon is confined to its initial position as the delocalisation via the previous second-order hopping process would now be a fourth-order hopping and thus for our purposes negligible. We show data on the delocalisation as a function of detuning for singly and doubly occupied initial states in Fig. 3.23a, where we consider the mean distance of the atoms from the initial position after a fixed time $\tau = 4\,\mathrm{ms}$. For single particles (grey markers), we observe the continuous slow-down of the delocalisation with increasing detuning, while the particles are never fully localised at the initial position. For doubly occupied initial sites (red markers), the situation is very different, as for most detunings, no delocalisation happens and the doublon remains at its initial position (see Fig. 3.23b). Only for $\Delta/U = 0$ and $\Delta/U = 0.5$ there is substantial spreading of the atomic distribution, which is seen both in experimental data and in theoretical results (solid lines). While the spread at $\Delta/U = 0$ is explained by the second-order hopping of the doublon itself, a different effect happens at $\Delta/U = 0.5$.

We study this specific situation in Fig. 3.24. By specifically tuning the potential offset to $U/2$, we enable a resonant process by which the doublon, initially situated in a site with lower potential, breaks up into two individual atoms on the two sites

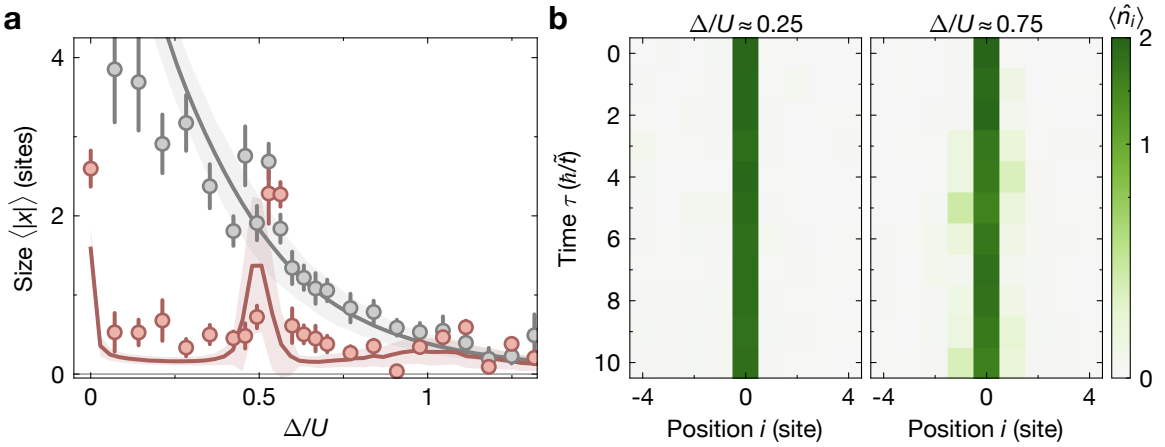

Figure 3.23: Spreading of density as a function of staggered potential. a, Mean size of density distribution after a fixed time $\tau = 4\,\mathrm{ms}$. For singly-occupied initial states (grey markers), delocalisation is increasingly suppressed with applied detuning Δ. Doubly-occupied initial states (red markers) are suppressed (see **b**), except at $\Delta = U/2$ where the doublon can split up and then delocalise. Theory predictions (solid lines) matches the experimental data well.

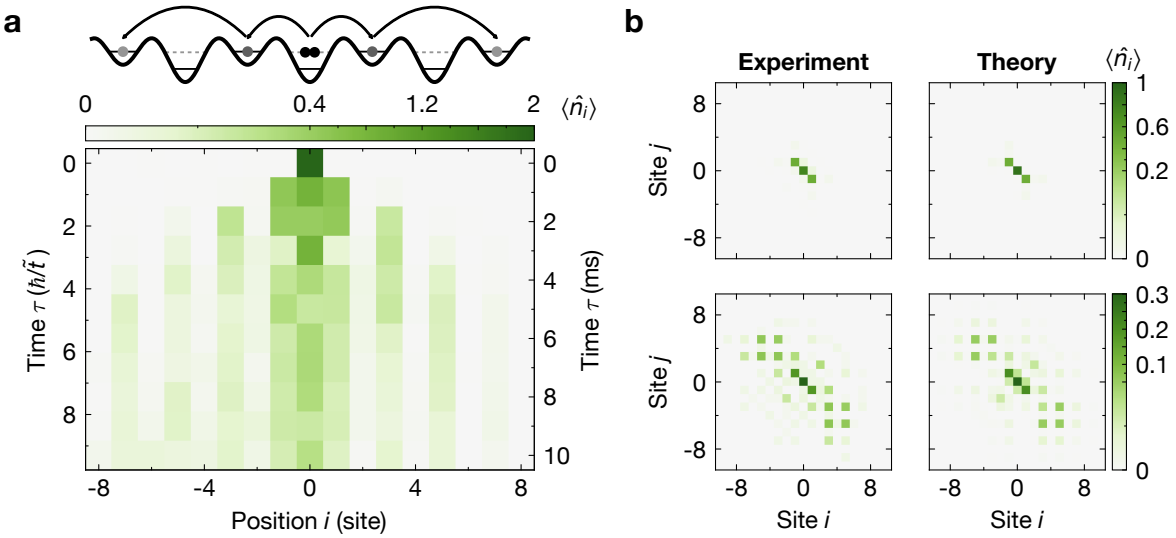

Figure 3.24: Two-particle quantum walk. a, Density distribution as a function of time after initialisation of a doubly occupied state at $i = 0$ at $\tau = 0$. After initial breaking of the doublon into two individual atoms, they delocalise with next-nearest-neighbour hopping as in Fig. 3.22. The two particles moving into opposite directions remain correlated as shown in **b**. Theory results match the experimental data.

on either side. As these two sites both are detuned by $U/2$, this exactly compensates for the interaction energy U of the doublon. After this initial breaking of the doublon, the individual atoms are then free to delocalise via resonant next-nearest neighbour hopping as in Fig. 3.22. The two atoms can then be found at spatially far separated positions, but they are not independent of each other. We also note, that a broad resonance is also expected at $\Delta = U$, as the doublon can break in a first-order process and then subsequently delocalise. The low amplitude in both theory and experiment is due to the long time scales of the subsequent single particle, next-nearest-neighbour hopping at these large detunings.

Finally, we find strong spatial correlations between the two atoms breaking due to the process at $\Delta = U/2$ as shown in Fig. 3.24b. We show two correlation maps at specific times $\tau = \hbar/\tilde{t}$ and $\tau = 3.5\hbar/\tilde{t}$ where we define $\Gamma_{ij} = \langle \hat{c}_i^\dagger \hat{c}_j^\dagger \hat{c}_j \hat{c}_i \rangle = \langle \hat{n}_i \hat{n}_j \rangle - \langle \hat{n}_i \rangle \delta_{ij}$. The agreement with theoretical calculations demonstrates the coherent, low-noise evolution of the atoms across the system.

3.4.4 Double-well Rabi oscillations

Optical superlattices allow for the preparation of atoms in double-well potentials, which may have applications as qubits with collisional gates. Here, we show single particle and many-body double-well systems, to showcase the high degree of stability and tunability of our system.

We start with single particles in a double-well system. Following a similar preparation procedure to Fig. 3.19, we load atoms into a deep lattice along x and superlattice along y in a far detuned phase, $V_x = 40(2)\,E_\mathrm{R}$, $V_y^\mathrm{SL} = 31(1)\,E_\mathrm{R}$, $V_y = 10.0(5)\,E_\mathrm{R}$, $\phi = -400\,\mathrm{mrad}$. We set the chemical potential to prepare one atom per double-well along y. We then quench the phase to the symmetric double-well configuration at $\phi = 0$ at time $\tau = 0$ within 50 µs to initiate the oscillations between the wells. After holding for a variable time, we then freeze the system for detection. The resulting occupation in one part of the double-well as a function of holding time $\langle \hat{n}_\mathrm{L}(\tau) \rangle$ is presented in Fig. 3.25 where we postselected on having a single atom per double-well. We observe coherent oscillation over tens of milliseconds. We can model our data with a damped oscillation as $\langle \hat{n}_\mathrm{L}(\tau) \rangle = \frac{1}{2}\left(1 + \cos(\omega\tau)\mathrm{e}^{-\alpha\tau}\right)$ with oscillation frequency ω and damping α and find good agreement for $\omega = 2\pi \times 1.273(1)\,\mathrm{kHz}$ and $\alpha^{-1} = 38(7)\,\mathrm{ms} = 48(9) \times 2\pi/\omega$. The frequency matches the expected value of $\omega_\mathrm{th.} = 2t_y/\hbar = 2\pi \times 1.33(20)\,\mathrm{kHz}$ from band structure calculations using the aforementioned lattice depths.

As mentioned before, it is possible to use these double-wells in quantum computation by interpreting the double-well two-state system as a qubit. A transfer from one part of the double-well to the other is then one component for a single qubit op-

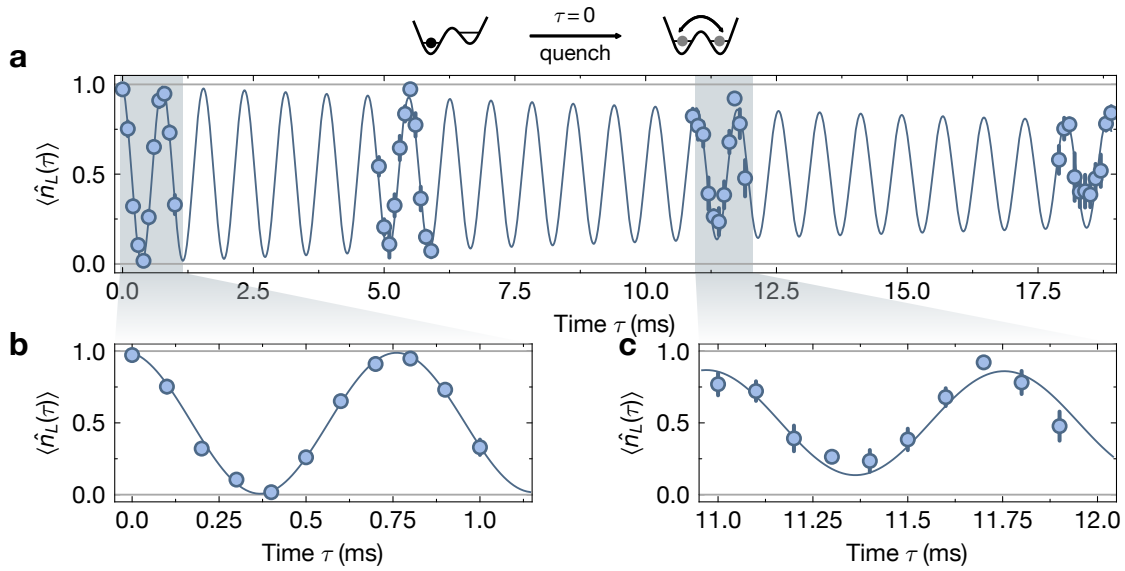

Figure 3.25: Rabi oscillations in a double-well. Evolution of a single-particle initialised in one part of a double-well after a quench to the symmetric phase. The weakly damped oscillation persists for tens of ms. We show high fidelity π-pulses in **b** and late-time oscillation in **c**. The solid line refers to a fit with decay time of $\alpha^{-1} = 38(7)$ms.

eration using a π-pulse. We achieve π-pulse fidelities of $P_\pi = 1 - \langle \hat{n}_\mathrm{L}(\tau = \pi/\omega)\rangle = 99.5(1)\,\%$ as extracted from the fit to the oscillation in Fig. 3.25. We estimate a measurement error of 0.3 % by measuring differences in occupation between subsequent fluorescence images of the same realisation. Correcting for this error, we have a fidelity of $\tilde{P}_\pi = 99.8(1)\,\%$. While these numbers are already encouraging considering the recent implementation of this type of qubit encoding, it so far cannot compete with the state-of-the-art in many other (non-fermionic) platforms (see below for more details). In the following, we will discuss possible sources and improvements to the dephasing in the system.

Spatial dephasing

One possible issue arises from the global lattice potential itself. We average over a certain spatial region where the individual double-wells may be slightly dephased with each other. On the one hand, the gradient of the harmonic confinement from the lattice beams could induce spatially varying offsets within the system. On the other hand, misalignment between the lattice and the superlattice can lead to lattice constants that are not perfectly commensurate which introduces spatially varying phases between the lattice and the superlattice. To study this effect, we measure the double-well os-

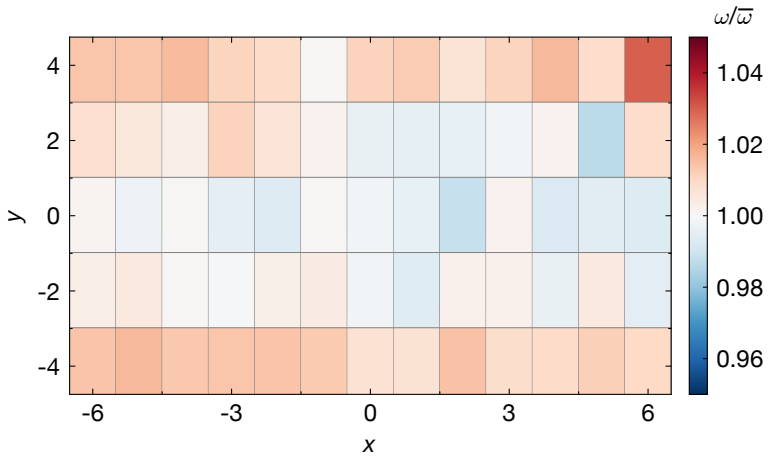

Figure 3.26: Local Rabi frequencies. Spatial map of local oscillation frequencies extracted from Rabi oscillations, normalised to the mean frequency $\bar{\omega}$.

cillation frequency as a function of position within the system as local detunings will lead to off-resonant Rabi oscillations at higher frequencies. We show the result in Fig. 3.26. We observe a small variation over the main system, dominated by the harmonic deconfinement of the lattice beams. We average over these inhomogeneities in simulated oscillations and show the result in Fig. 3.27a. For future improvements of this issue, there are several pathways: either increasing the lattice beam diameter (which is severely limited by the available power), or trying to compensate the different confinement contributions by precisely choosing lattice depths. Finally, precise compensation of this potential with a DMD is also a possibility.

Noise-induced dephasing

Several noise sources can lead to dephasing of the observed oscillations. First, we can also investigate phase noise and its impact on the decay due to varying detuning between the wells. This leads to dephased, off-resonant oscillations, leading to a change in both contrast and frequency of the oscillation. Simulated data is shown in Fig. 3.27b, where the resulting power-law decay can be seen. For this, we used the upper bound from section 3.4.2 of 5 mrad for shot-to-shot phase fluctuations (25 mrad in red). For experimentally relevant parameters, this might explain the observed decoherence in the experiment. Furthermore, the late time behaviour shows an offset from the balanced distribution around 0.5. This feature is also visible in the experimental data, but may also be an artefact of drifts as discussed in the next section.

Similarly, intensity noise on the lattice beams will transfer to frequency noise due to time-dependant couplings and thus dephased oscillations. We chose our laser

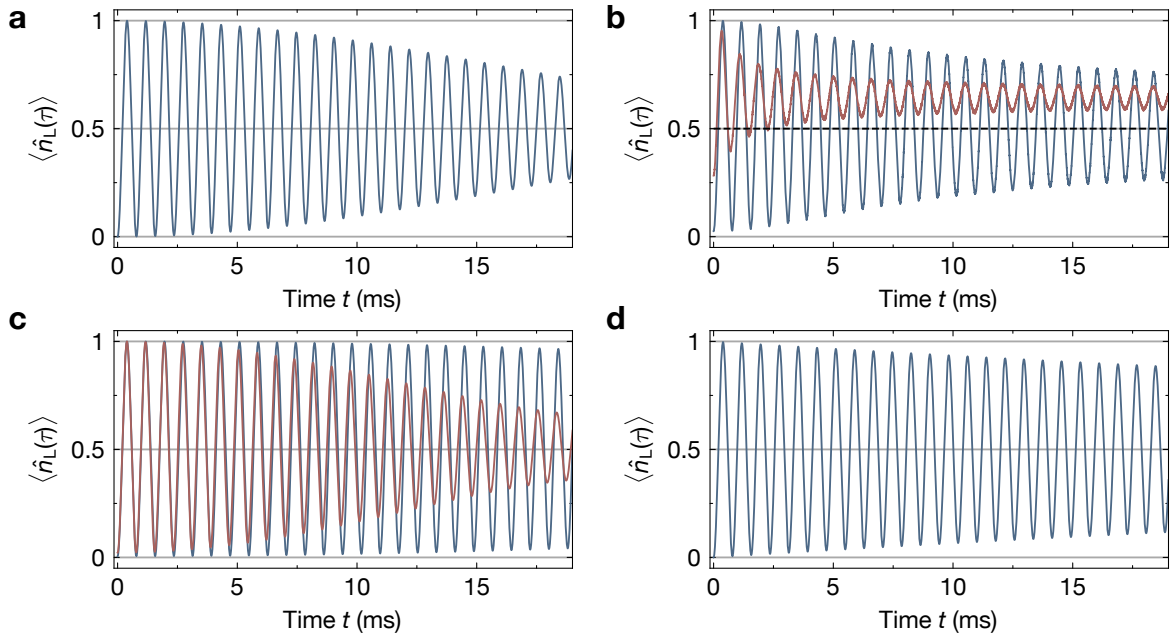

Figure 3.27: Decoherence sources. Comparison of dephasing of double-well Rabi oscillations induced by **a**, spatial inhomogeneities, **b**, phase noise (5 and 25 mrad respectively), **c**, phase drifts (over 2 and 4 h), and **d**, interwell coupling. Multiple effects possibly add up to the observed dephasing.

sources to try to minimise intensity noise and stabilise the intensity further with AOMs (see section 3.3.2) such that intensity noise should not impact the data.

Drift induced dephasing

We have previously shown that the relative phase of our superlattice is subject to slow drifts of the relative superlattice phase on the order of $\sim 2\,\mathrm{mrad/h}$. As we require several realisations of the experiment per setting, phase drifts within the measurement window are present. These drifts are especially relevant in this situation where we work close to the symmetric phase and are therefore most sensitive to small deviations. Drifts will manifest similarly to phase noise in the data, as shown in Fig. 3.27c where a linear drift of 2.0 mrad/h over measurement time of 2 (4) hours was assumed for the blue (red) line. While the exact cause of this drift is so far not known, we can mitigate it by performing regular calibration measurements. By interweaving phase scans as in Fig. 3.14 into the main measurement, we can determine the exact phase in very few realisations. This allows us to compensate for this drift without losing too much experimental statistics.

Dephasing due to interwell couplings

So far we have assumed all double-well to be closed systems and perfectly independent of each other. This is only exactly the case in the limit of infinite lattice depths along x and the superlattice along y. While the coupling along x at $V_x = 40\,E_\mathrm{R}$ is only $h \times 0.7\,\mathrm{Hz}$ and thus negligible, the superlattice is only at $V_y^\mathrm{SL} = 31(2)\,E_\mathrm{R}$. Therefore, the remaining interwell coupling is $h \times 14\,\mathrm{Hz}$. Comparing this to the intrawell coupling of $h \times 663\,\mathrm{Hz}$, it can be quite significant and lead to reduced coherence times. In principle, it is straightforward to solve this problem by adding more power to the y-superlattice. In this case, we are not limited by the available laser power as it is operated at 1064 nm. While we are at the moment restricted by technical limits, we plan to improve on this issue and thereby significantly increase the coherence time.

In summary, several of these noise sources could potentially contribute to the observed decay rate, where a more precise identification of the limiting effect requires further investigations. Further improvements in the compensation of harmonic confinement in addition to frequent recalibration of the lattice phase can reveal the origin of the dephasing and allow for significant improvements in fidelity.

Comparison to other platforms

Ultracold fermions have been proposed as a platform for quantum computation by making use of their inherent statistical properties [227, 228]. Here, single-qubit gates can be implemented using single particles in a double-well potential, as shown in the experiment above. Two-qubit gates are then in direct extension to be realised via collisions between two atoms in a double-well [229]. In that sense, a superlattice potential already forms a basic building block for a fermionic quantum processor. However, to connect different double-wells with each other, additional tweezer potentials may be used to shuttle atoms between sites. Using bosons in a superlattice potential, there has already been progress and single-qubit gate errors of 1.2×10^{-4} have been shown [119]. An alternative approach to using a superlattice potential is found in optical tweezers arrays. Building the potential in a 'bottom-up' approach [230] leads to an architecture without the need for an additional superlattice by simple 'merge' and 'shuttle' gate operations [231]. The required homogeneity for tweezers to build an optical lattice potential has also been demonstrated in 1d and 2d [105, 232].

In recent years, using optical tweezers in combination with Rydberg excitation has emerged as a powerful tool for quantum computation [233, 234]. Nuclear qubits encoded in alkaline and alkaline-earth atoms allow for precise global and local qubit manipulation. Both single- and multi-qubit gates have been implemented and error-correction codes have been demonstrated [25, 235]. Usual single-qubit error rates are on the order of $10^{-3} - 10^{-4}$ [236–242] with exceptional fidelities down to $3.0(7) \times$

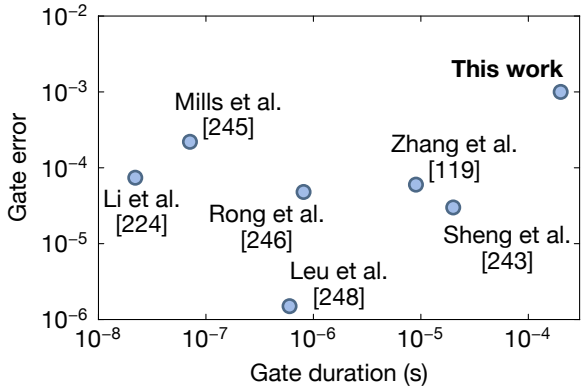

Figure 3.28: Gate performance comparison. Comparison of single-qubit gate fidelity and duration for different platforms. Highest gate fidelities have been achieved in trapped ions ([248]), while fastest performance is found in superconducting qubits ([224]).

10^{-5} having been shown [243, 244].

There are numerous other platforms which compete with ultracold atoms in achieving the highest gate fidelities with short gate durations in large systems. Prominently, superconducting qubits have been under much investigation. In this case, single-qubit gate errors down to 7.4×10^{-5} have been shown [224]. Similar fidelities are found using quantum dots (down to 4.4×10^{-4} [245]) and NV centres (4.8×10^{-5} [246]). The best gate fidelities so far have been demonstrated using trapped ions where errors down to $1.0(3) \times 10^{-6}$ have been achieved [247, 248].

We note that especially single-qubit gate fidelity is by far not the only relevant quantity to compare the performance of quantum processors. We show a comparison of these fidelities and gate durations for different platforms in Fig. 3.28. We emphasise that a more thorough optimisation of gate performance as well as more thorough testing using randomised benchmarking was not performed so far on this experiment and thus remains as a future prospect. Furthermore, despite so far lower gate performance, cold atoms have multiple advantages compared to other platform, especially due to their indistinguishability and scalability.

3.4.5 Engineering Fermi-Hubbard couplings in ladder systems

For the purposes of our experimental setup, one major application is the possibility to explore new parameter regimes of the Fermi-Hubbard Hamiltonian. The introduction of well-controlled potential offsets Δ on every other lattice site, leads to modified tunnel and spin couplings. By tuning both lattice and superlattice depths as well as the relative phase between the lattices, we can cover a wide range of different parameters.

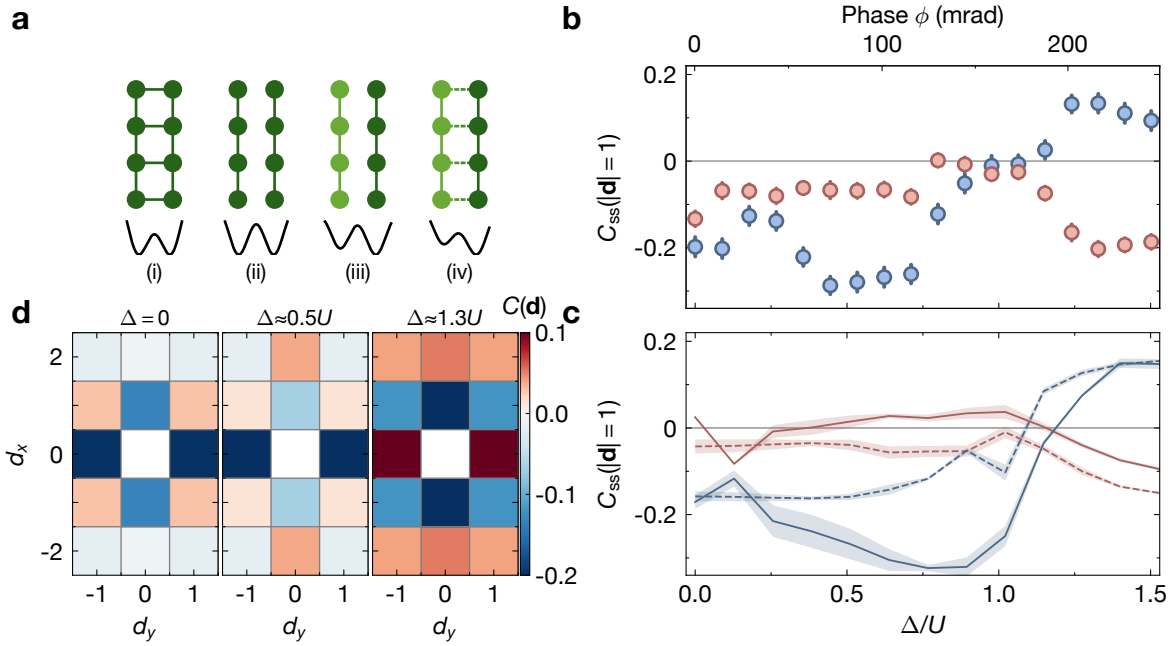

Figure 3.29: Tunable spin coupling using superlattices. **a**, Preparation sequence of detuned ladder systems. **b**, Nearest-neighbour spin correlations along x (red markers) and y (blue markers) as a function of detuning. Around $\Delta = U$, strong mass transport leads to vanishing correlations. For $\Delta > U$, the sign of the correlations along y changes to become positive. The correlations along y are strongest for $\Delta \approx 0.5\,U$. Theory results in **c** at $k_B T/t = 0.2$ at half-filling (solid lines) and a doping of $\delta = 0.125$ (dashed line) agrees with experimental results. Full 2d correlation maps in **d** show the mixed AFM-FM correlation produced at detunings $\Delta > U$.

While the overlap of the Wannier functions only changes marginally with detuning, resonant tunnelling is suppressed (see also section 4.3 for more detailed discussion). However, spin couplings are a second order effect that change continuously with detuning. Following the discussion in [249], we perturbatively find

$$J = \frac{2t^2}{U+\Delta} + \frac{2t^2}{U-\Delta} \tag{3.7}$$

which holds as long as the virtual population in the intermediate state is small enough, i.e. for $\Delta \neq U$. This has been experimentally explored in optical superlattices in [197] and more recently using single-site addressing been applied to ladder systems in [164].

Here, we explore the basic physics using a ladder system. To avoid mass transport, we prepare the system by first loading into two decoupled 1d chains before restoring their coupling (see Fig. 3.29a and section 4.3 for more details). We load

into individual 2-leg ladders of size $L_x \times L_y = 11 \times 8$ with $V_x = 9.0(5)\,E_R$, $V_y = 11.0(5)\,E_R$, $V_y^{SL} = 23(1)\,E_R$ with varying relative superlattice phase ϕ. We set the interactions to $U = h \times 5.04(12)\,\mathrm{kHz}$, with tunnel couplings $t_x = h \times 167(20)\,\mathrm{Hz}$ and $t_y = h \times 345(51)\,\mathrm{Hz}$. The chemical potential is such that the system is slightly hole-doped with $\langle \hat{n} \rangle = 0.93$. We evaluate nearest-neighbour spin-spin correlations as a function of detuning along x (red markers) and y (blue markers) in Fig. 3.29b. We observe an increase in spin correlations along y with increasing detuning, which is consistent with the increase in superexchange coupling. Around $\Delta = U$, the perturbative result of Eq. (3.7) does not hold any more due to excessive population in the intermediate state such that spin correlations along both directions vanish. For $\Delta > U$, the spin correlations along y turn ferromagnetic, consistent with the change in sign of the superexchange coupling in this regime. Meanwhile, couplings along x stay approximately constant or decrease slightly below $\Delta = U$, as correlations are 'redistributed' towards y. For $\Delta > U$, correlations become more strongly negative as the correlations along y change sign. The qualitative features of these results are reproduced in finite temperature exact diagonalisation (ED) calculations in Fig. 3.29c on a small system of $L_x \times L_y = 4 \times 2$. The solid (dashed) line is at a filling of $\langle \hat{n} \rangle = 1$ ($\langle \hat{n} = 0.875 \rangle$) at a temperature of $k_B T/t = 0.2$. Despite significant finite size effects, especially for the doped system, the change of sign for $\Delta > U$ as well as the increase in correlations along y for $\Delta < U$ are clearly visible. We show the spin correlation map for several detunings in Fig. 3.29d. In addition to the nearest-neighbour signals discussed before, we also observe an increase in correlation length along x. While for $\Delta = 0$, correlations at distance $d_x = 2$ are slightly negative, they now become significantly positive for $\Delta = 0.5\,U$ and $\Delta = 1.3\,U$.

3.5 Summary

We have shown the design and characterisation of a new, high-stability bichromatic superlattice setup. We made use of the inherent passive phase stability of the bichromatic design to reduce our fluctuations below 5 mrad, which is the lowest value achieved for a square superlattice so far. By shielding the system from the environment using a Zerodur® base, we have reduced absolute phase changes to below 0.2 lattice sites over many hours of measurements. We characterise the stability by observing single-particle Rabi oscillations in individual double-wells, where we detect long coherence times, opening the possibility of fermionic quantum computation. The high degree of homogeneity of the lattice is shown in 1d quantum walks both in flat and staggered potentials. Finally, we have shown an application of the tunable superlattice phase in the engineering of superexchange coupling from antiferromagnetic to ferromagnetic correlations in 2-leg ladders.

Despite the large capabilities of our lattice, there are still several ways to further improve the setup in a possible next iteration. First, more power in both the lattice and superlattice would reduce the harmonic confinement and thus allow larger system sizes by increasing the beam waist. With limited available laser sources, introducing elliptical beams may be required here. While the cause of the residual phase fluctuations are not known precisely, reducing the path travelled through air between the lattice setups and the main vacuum system, may lead to improved relative phase stability.

The high-degree of stability opens up a plethora of applications, including the realisation of stripe phases in mixed-dimensional systems discussed in the next chapter. However, also in the context of quantum computation, our optical superlattice shows promise. By building on top of the already demonstrated single-particle operations, we can implement two-qubit operations by using the interactions between particles [228, 229]. This can be done either globally by setting the global phase such that the two wells are in resonance, or locally by adding additional single-site potentials to shift individual double-wells into resonance. Finally, superlattices are useful tools in achieving lower temperatures. In a bilayer configuration, the high degree of control over the relative detuning can be used to set up one layer as a reservoir to carry excess entropy from the main system [250]. Alternatively, exploiting the large gaps of band insulators allows for the preparation of very low entropy states which in turn can be adiabatically transferred into a Mott insulating state using superlattices [251].

Chapter 4

Signatures of stripe formation in a mixed-dimensional system

In this chapter, we describe the experimental progress towards the study of low-temperature stripe phases of the Fermi-Hubbard model. We discuss past experimental and theoretical studies and how this phase relates to superconducting phases. We then show our particular realisation of stripes in a Fermi-Hubbard system which, due to the strict temperature requirements, relies on a specific, mixed-dimensional geometry to increase energy scales to experimentally accessible regimes. We present results in both the charge and the spin sector, pointing towards stripes forming in the system. The results of [206] are contained in this chapter. Numerical calculations presented here were performed by our collaborator Henning Schlömer.

4.1 Stripe phases in context

4.1.1 Low-temperature phases of the doped Fermi-Hubbard model

After high-temperature superconductivity had been discovered in the cuprate compound $La_{2-x}Ba_xCuO_4$ (LBCO) [73], the unexpected insulating nature of the undoped state sparked numerous theoretical investigations. This discovery was surprising at first as it could not be explained based on phonon-mediated attraction by the successful BCS theory of superconductivity. Therefore a new theoretical description was required. Such a model was found in the 2d Fermi-Hubbard Hamiltonian as defined in Eq. (2.1) [80, 254], which is a minimal model for strongly correlated phases, driven by the competition of its two terms: kinetic delocalisation versus magnetic ordering. This leads to a rich phase diagram which may describe both the insulating behaviour as well as the superconducting regime based on the exact parameters. A brief overview of the phase diagram for strong interactions $U/t \gg 1$ as depicted in Fig. 4.1 is given here.

In the undoped state, the 2d Fermi-Hubbard model is insulating and forms a Mott insulator as doubly occupied sites are suppressed. Depending on the temperature,

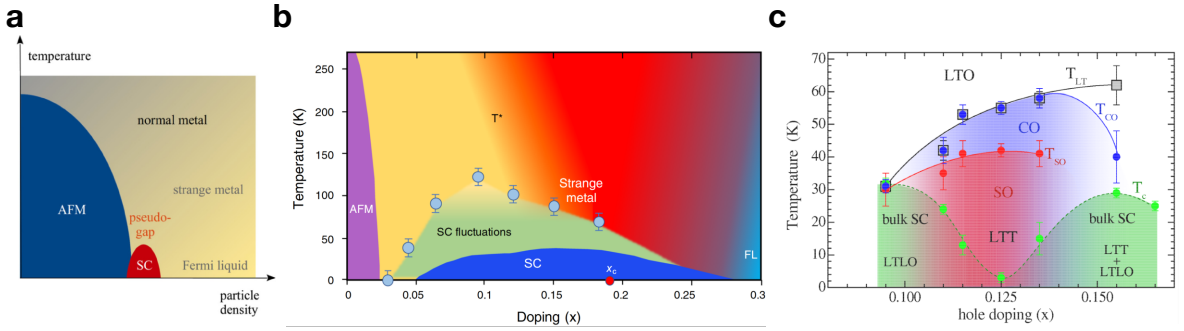

Figure 4.1: Phase diagrams. a, Conjectured phase diagram of the 2d Fermi-Hubbard model for strong interactions $U/t \gg 1$ with antiferromagnetic (AFM), superconducting (SC) and Fermi liquid (FL) phases. **b** (**c**), Phase diagram of cuprate materials $La_{2-x}Sr_xCuO_4$ ($La_{2-x}Ba_xCuO_4$). Even between two closely related materials, significant differences in their phase diagram are visible. The interplay between spin and charge stripe order (SO and CO) with the addition of structural changes between low-temperature (less-)orthorombic (LTO/LTLO) and tetragonal (LTT) lattices lead to complex behaviour that is hard to model in theoretical investigations. The phase diagrams are adapted from [91], [252] and [253] respectively.

this can be a paramagnetic state for $T > T_{\text{Néel}}$ or an antiferromagnetic state for $T < T_{\text{Néel}}$. Note, however, that for 2d systems there is only long-range order in the ground state [132]. In the opposite limit of large doping ($\delta \gtrsim 30\%$), the system can be accurately described by Landau's Fermi liquid theory, making the system metallic. Between these two limits, the ground state is dominated by collective effects, which have been speculated to be superconducting, as discussed in more detail later on. The exact processes governing the doping region around ca $10 - 20\%$ doping are still under heavy debate and may depend strongly on the precise model parameters. For higher temperatures $T > T_C$, the system returns to a metallic state. However, the physics in this region also feature peculiar effects, that are not fully understood, as excitations seem to be suppressed in certain regions of the Fermi surface. This so-called pseudogap regime is often considered as a precursor to the more collective effects coming into play when cooling the system further down. Even the metallic phase (dubbed strange metal) exhibits non-trivial properties as its resistivity rises linear with temperature.

The 2d Fermi-Hubbard model of Eq. (2.1) is a minimal model for strongly correlated systems, but does not capture the full phenomenology of cuprate materials. As can be seen in Fig. 4.1b, c, while $La_{2-x}Sr_xCuO_4$ (LSCO) seems to exhibit similar features to the conjectured Fermi-Hubbard phase diagram, LBCO on the hand displays interesting effects at a doping of $1/8$ (see below for further discussion). The excessively wide range of possible coupling terms and parameter regimes impedes a full,

comprehensive study of the Fermi-Hubbard model, with small out-of-plane, diagonal or next-nearest-neighbour couplings playing important roles (see section 4.1.3).

4.1.2 Stripe phase definition and signatures

Historical overview

Despite superconductivity being the most prominent low-temperature phase in the doped cuprates, numerous alternative states have been observed and investigated. Especially the so-called stripe phase has attracted a lot of interest due to its proximity and overlap with possible superconducting phases. While the exact origin and relationship of superconductivity and stripes is not conclusively known, the last decades have led to many insights into the properties of stripe phases.

In 1994/95, almost a decade after the discovery of high-temperature superconductivity, Tranquada et al. discovered charge-ordered stripes in $La_{1.6-x}Nd_{0.4}Sr_xCuO_4$ and La_2NiO_4 at a doping of $1/8$ [82, 83, 255, 256]. Already a few years earlier, unexpected features in the spin structure factor in LSCO had indicated the presence of spin stripes, pointing towards the possible existence of charge stripes as well [257–263]. Due to the very similar temperature dependence of charge and spin stripes, theories citing the spin order as the origin of charge ordering were proposed.

While the subsequent rise of DMRG allowed for more detailed studies, the near-degeneracy of many different states remained a numerical challenge. Only in recent years, numerical progress as well as cross-comparison between many different methods allowed for more rigorous studies of the low-temperature phase diagram [81, 85, 87].

Stripe order properties

In general, stripe order is a charge density wave where dopants align along a specific lattice direction, leading to a breaking of the crystal symmetry. While this charge order can in some cases be accompanied by a similar spin density wave, it has been shown that in reverse, spin stripe order requires charge stripe order [264]. The charge density wave may be seen as micro-phase separation along a given axis [74]. This axis can either be any direction (thus forming fluctuating stripes) or unidirectional, leading to static stripes. It has been suggested that stripe order is enhanced by specific lattice distortions [82, 255, 265, 266]. In DMRG studies, a similar effect is reached due to the anisotropic geometry of the system as well as the periodic/open boundary conditions along the short/long lattice axis. The charge and spin density waves are closely intertwined with the nodes of the spin density wave sitting at the positions of highest dopant density such that the dopants act as domain walls in the spin

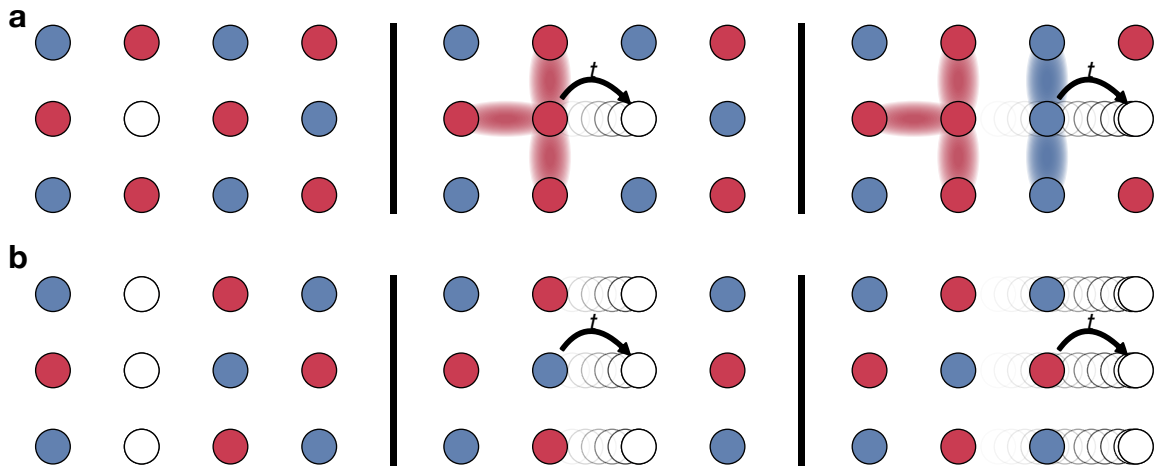

Figure 4.2: Dopant delocalisation. Effect of dopant delocalisation in an antiferromagnetic background. With every hopping event with amplitude t of a single hole in the system, the surrounding antiferromagnetic spin order is destroyed (**a**). Therefore kinetic energy advantages are penalised with a cost in magnetic energy. For charges arranged in a stripe, the whole structure can delocalise without disturbing the magnetic background (**b**).

pattern [267]. Consequently, while the exact periodicity of stripe order has not yet been conclusively determined theoretically, it is usually observed between 4 and 8 sites [87], where spin stripes have a period twice that of charge stripes. Furthermore, there exist many more variations to stripe order. Both experimental [268] and theoretical [269, 270] investigations have revealed the possibility of half-filled stripes while diagonal stripes may also dominate in specific situations [87, 268, 271]. Finally, the question whether stripes prefer to be bond- or site-centred with respect to the lattice is not yet determined either [125].

Microscopic picture

While there is no conclusive, microscopic theory describing stripe formation in either theoretical models or the cuprates, there are numerous proposals trying to explain the observed phenomenology. In the following, we will introduce three prominent microscopic interpretations of stripe ordering where we will focus on coexisting charge and spin stripes as e.g. in La-based compounds. In the undoped regime, the system has antiferromagnetic correlations due to superexchange couplings. Individual holes introduced into the system will then try to delocalise to lower their kinetic energy. Delocalisation of dopants does, however, negatively impact the magnetic order, leaving behind a 'string' of displaced spins (see Fig. 4.2a). This leads to a competition between

kinetic and magnetic energy, which drives most of the physics at low temperatures. The result is each dopant being surrounded by a region of disturbed spin correlations, forming a new quasiparticle called a magnetic polaron [272].

Starting from this picture, we can now interpret stripes as interacting polarons, where for suitable doping and couplings, the lattice symmetry is broken, leading to effective attraction along one direction. This state is energetically favourable in the sense of micro-phase separation as bunching dopants together in charge stripes leads to overall less disturbance of the magnetic AFM background. The spin stripe structure is then inherited from polaronic spin correlations which already show a phase jump across a dopant (see Fig. 4.2b) [106].

A second, similar interpretation of stripes is found based on pairing of dopants. Real-space pairing of charge carriers to bosonic pairs [78] may allow for condensation of these pairs into metallic 'rivers', forming stripes. This interpretation would lead to (super)conducting stripes, as found in for example LBCO at $\delta = 1/8$. This interpretation is limited as there are also many materials, such as LSCO, where the ground state exhibits insulating stripes.

Finally, instead of starting from a strong coupling perspective, we can also think about it in the weak coupling limit. Starting from Fermi liquid theory, stripe order occurs when there are nearly nested segments of the Fermi surface [74]. While this interpretation can lead to interesting insights especially for transport measurements, for many observables there is experimental evidence more in favour of a strong coupling approach. Most importantly, whenever charge and spin stripes are present in a material, charge stripes appear at higher temperatures than spin stripes [273, 274], while in the weak coupling regime, they appear simultaneously [74].

Experimental observables and measurements

Over the years, many experimental methods have been used to identify stripe order in numerous materials. For a more detailed review of experimental studies see [30, 74]. One of the most prominent methods are diffraction measurements, either elastic neutron or x-ray scattering. By measuring the magnetic and nuclear structure factors $S(\boldsymbol{k}, \omega = 0)$, charge and spin stripes can be investigated. After the original neutron scattering measurements in 1995 on $La_{1.48}Nd_{0.4}Sr_{0.12}Cu0_4$ (see Fig. 4.3), similar studies on hole-doped La- and Y-based superconductors found evidence of charge stripes. Complementary to these momentum space measurements, advances in scanning tunnelling microscopy (STM) lead to the possibility of real-space studies on an atomic scale by measuring the local density of states (see Fig. 4.4). Surveys on $Bi_2Sr_2CaCu_2O_{8+\delta}$ [275, 276], $Bi_2Sr_{2-x}La_xCuO_{6+\delta}$ [277] as well as LBCO [278] added local information for systems with short coherence lengths. In addition, studies using e.g. NMR [279], ARPES [278, 280] or TEM [281, 282] have been performed.

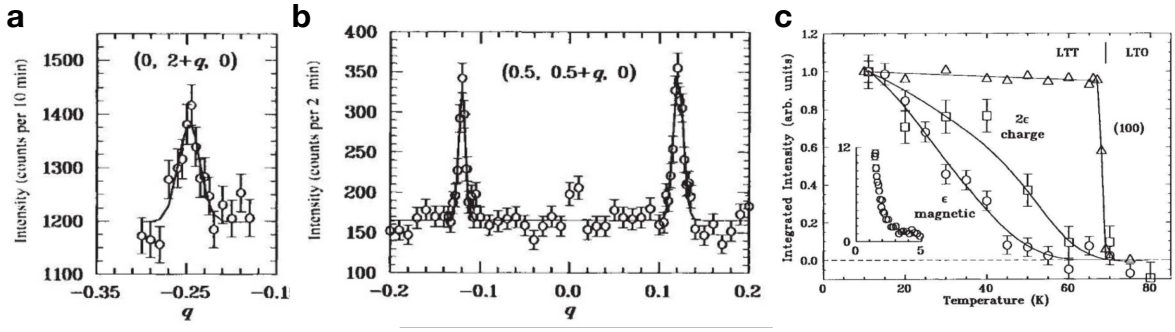

Figure 4.3: Solid state stripe measurements. Neutron scattering studies on $La_{1.48}Nd_{0.4}Sr_{0.12}Cu0_4$ for a doping of $\delta = 1/8$. **a**, Evidence of charge stripes in superlattice peaks at a period of $2\delta = 0.25$ by scanning along $(0, 2-q)$. **b**, Spin stripe signature from diffraction peaks at $(1/2, 1/2 \pm \delta)$. The orientation of the stripe is pinned by the low-temperature tetragonal (LTT) crystal structure (in contrast to low-temperature orthorombic (LTO) structures). **c**, Temperature dependence of diffraction peaks shown in **a**, **b**. Charge structure survives to higher temperature than spin structure but disappears below LTT-LTO transition. Adapted from [83].

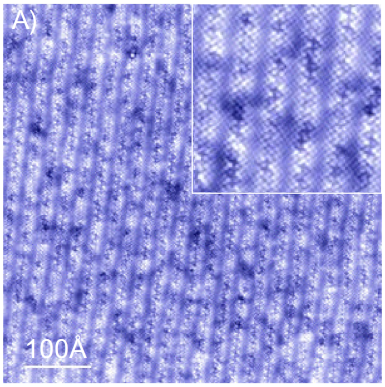

Figure 4.4: Real space solid space measurement. Topographic STM measurement on $Bi_2Sr_2CaCu_2O_{8+\delta}$ with clearly visible supermodulation on a field of view of 560 Å. The inset shows the atomic resolution with higher magnification. Adapted from [275].

Theoretical methods and limits

The inherent fermion sign problem of the Hubbard model has been a main limitation to definite solutions of the low-temperature phase diagram. In the last decades, many methods have been applied to tackle this problem. Early on, a lack of computational resources led to main results being extracted from mean-field calculations [267, 283, 284]. The rise of density-matrix renormalisation-group (DMRG) methods allowed for more precise studies, limited by the available system size. Finally, several different

Method	System size	Limits
DMRG	$6 - 7 \times 64$	System size and boundary conditions
METTS	32×4	System size and boundary conditions
CP-AFQMC	72×12	Error from constrained path approximation
DQMC	32×32	Lowest achievable temperature $k_B T/t \sim 0.2$
iPEPS	Thermodynamic limit	Empirical extrapolation techniques
DMET	Thermodynamic limit	Finite impurity-size error

Table 4.1: Overview of numerical techniques. List of algorithms based on matrix-product-state (density-matrix renormalisation group, DMRG, and maximally entangled typical thermal states, METTS), quantum Monte-Carlo (constrained-path, auxilliary-field QMC, CP-AFQMC and determinant QMC, DQMC), density matrix embedding DMET and infinite projected entangled pair states, iPEPS

quantum Monte-Carlo methods have ben successfully applied on larger system sizes, despite also only being able to investigate specific parameter regimes or relying on approximations [87]. A selected overview of available methods and some of their limitations is given in Tab. 4.1. Wide-range studies in recent years cross-referencing a number of different methods showed consistent results, albeit with very small energy gaps for some states [81, 87]. Most importantly, it has been shown that the ground state of the plain, 2d Fermi-Hubbard model at physically relevant parameters of $U/t \sim 8$ and $\delta = 1/8$ is indeed a striped state [81]. Meanwhile, many details concerning the exact properties of this state are not yet determined as e.g. the exact periodicity of these stripes. As shown in [87] (see Fig. 4.5a), the energy gaps between stripe states of different periodicity is within the uncertainty of the individual methods. While $\lambda = 8$ seems to be slightly favourable, exact claims on this result remain a subject of further debate. Especially methods limited by their small system size along one direction (such as DMRG and METTS), are affected by this as in this case commensurability effects between stripe filling, periodicity and doping can be relevant. For example, as shown in [81], for a 6-legged system, only fully filled or $2/3$-filled stripes can be stabilised. Similarly, 4-leg systems are essentially two coupled plaquettes, such that pairing and half-filled stripes are indistinguishable. Finally, due to the aforementioned small energy differences between states, model variations have large effects on the ground state properties. In this case, it may matter whether the full Fermi-Hubbard model or the strong-coupling limit $t - J$ model is being simulated. Furthermore, as will be discussed in the next section, next-nearest-neighbour couplings can have significant impact when being included in the model.

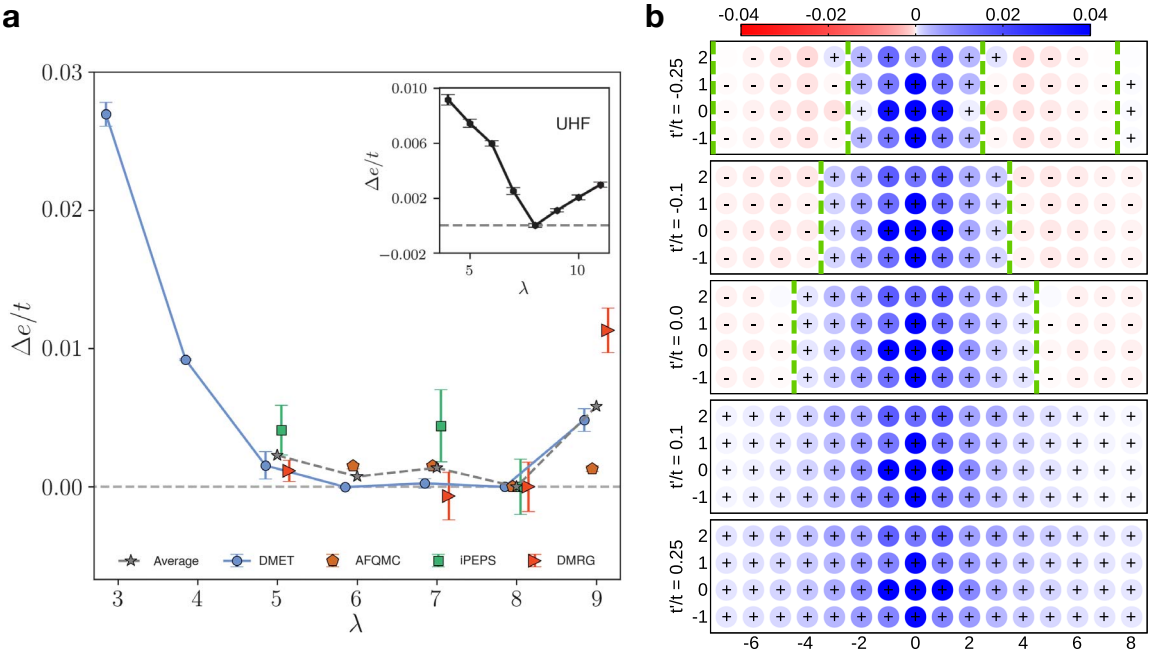

Figure 4.5: Numerical stripe studies. **a**, Stripe state energies from different numerical methods as a function of wavelength λ for $U/t = 8$, $\delta = 1/8$ relative to the energy at $\lambda = 8$. Adapted from [87]. **b**, Staggered spin correlations from DQMC for $\delta = 0.125$, $U/t = 6$, $k_B T/t = 0.22$ for several t'/t. Adapted from [85].

4.1.3 Stripes and superconductivity

The presence of charge stripes in direct vicinity or in coexistence with superconductivity in the cuprates poses the question, what exactly the relationship between these two phases is. The '1/8-anomaly', where materials such as LBCO exhibited a strong suppression in T_c at a specific doping, was assumed to be caused by the emergence of stripe order at this doping level due to commensurability effects [83]. Therefore, the interpretation that stripe order competes with spatially uniform d-wave superconductivity seemed likely [84]. However, there is also experimental evidence of stripes coexisting with superconductivity [285]. One possible explanation for this may be non-uniform superconducting states, where the individual static charge stripes become superconducting once coherence is established between the regions of high dopant concentration [125].

From a theoretical point of view, recent studies have established a few main points concerning the intricate connection between these two phases. First, it has recently been shown using AFQMC and DMRG methods that the pure, 2d Fermi-Hubbard model without next-nearest-neighbouring coupling t' for $U/t = 8$ and $\delta = 1/8$ is

a stripe phase without superconducting correlations[1] [81]. The pair-pair correlations decay exponentially with a correlation length of ~ 2.9 sites. Furthermore, by applying a pairing field, it has been shown that there is actual competition between these two states as stripe order vanishes with increasing pairing field. This result is fairly robust with respect to changes of U/t, as for $U/t \geq 6$, i.e. in the strong coupling regime, stripe phases seem to dominate. Similarly, changes in the exact doping mostly affect the stripe periodicity or filling. [81]

The impact of next-nearest-neighbour coupling has been investigated in DQMC for $U/t = 6$ and $k_\mathrm{B}T/t = 0.2$ [85]. For $t'/t = 0$ the system is a stripe phase, consistent with the study described above. However, for $t'/t = -0.25$, the periodicity of the stripes is $\lambda \sim 5$ instead of $\lambda = 8$ and thus closer to experimental results [83] while retaining the same general stripe phase features (see also Fig. 4.5b). On the other hand, for $t'/t > 0$, the stripe phase is not favourable any more. In this case, simple AFM order dominates as dopants can again move freely diagonally through the system without any frustration [85].

Finally, the question remains, where the key differences between different experimental findings in the cuprates and numerical results in the Fermi-Hubbard model arise. One key ingredient has been found in [85] to be the aforementioned next-nearest-neighbour hopping. Agreement is substantially better when including slightly negative values of t'/t. However, it is still not ultimately known whether the long-range Coulomb interaction is a relevant and necessary component in the description of the low-temperature phases of the cuprates. This may also help to explain differences in stripe periodicity. Lastly, the precise impact of interlayer couplings remains an open question [125].

4.1.4 Perspective from quantum simulation with ultracold atoms

Between the numerically difficult theoretical studies of the Fermi-Hubbard model and the experimental work on the cuprates that depend on the precise material being investigated, new approaches hold the potential to yield new insights into strongly correlated systems. Quantum simulation using ultracold atoms in optical lattices allows for the precise characterisation and tunability of system parameters while measuring a wide range of both local and global observables (see chapter 2 and 3). While so far not being able to achieve sufficiently low temperatures to fully delve into the lowest collective phases of the phase diagram of the Fermi-Hubbard model, cold atoms can exceed the system sizes achieved e.g. in DMRG or METTS. The microscopic resolu-

[1] These are defined via the pairing operator $\hat{\Delta}_{ij} = (\hat{c}_{i\uparrow}\hat{c}_{j\downarrow} + \hat{c}_{i\downarrow}\hat{c}_{j\uparrow})/\sqrt{2}$ and the resulting pair-pair correlation function $P_{i'j',ij} = \langle \hat{\Delta}^\dagger_{i'j'} \hat{\Delta}_{ij} \rangle$. This term can explicitly added to the Hamiltonian using a pairing field $\hat{H}_p = -\sum_{\langle i,j \rangle} h_p^{ij} (\hat{\Delta}_{ij} + \hat{\Delta}^\dagger_{ij})/2$ [81].

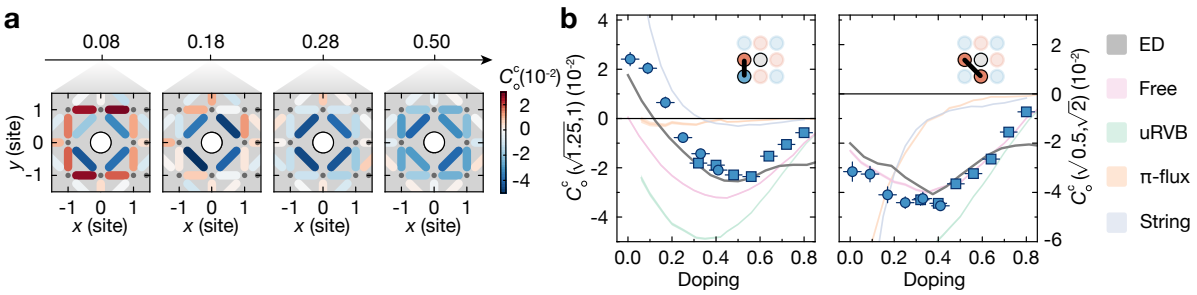

Figure 4.6: Polaron signatures in quantum simulation. **a**, Evolution of connected hole-spin-spin correlations around a hole with doping. Above 30% doping, the system only shows Fermi-liquid like behaviour. **b**, Comparison of correlations at specific distances with different theories. Only exact diagonalisation and effective string theories yield the correct sign at low doping. Adapted from [66].

tion allowed for the study of the evolution of polarons with doping in the repulsive Fermi-Hubbard model (see Fig. 4.6) [66, 106, 286]. A detailed comparison to different, effective theories revealed a good agreement with Fermi-liquid like behaviour at high doping, while at low doping only effective string theories captured the correct sign of the correlators. Similarly, studies on the attractive side of the Fermi-Hubbard model found non-local pairs [72].

To truly investigate phases closer to the ground state, improvements in temperature are required. With latest studies already showing signs of approaching the pseudogap regime [111] and theoretical studies hinting towards pairing at temperatures that are within reach [287], several methods for further cooling have been proposed and partially implemented [198, 250, 251]. An alternative route lies in the engineering of couplings as will be discussed in the next section.

4.2 Charge order in mixed-dimensional systems

While ultracold atoms have several advantages over solid state experiments in terms of microscopic control and readout, the main limitation for the exploration of the Fermi-Hubbard model is usually the lowest achievable temperature. State-of-the-art fermionic quantum gas microscopes realise temperatures as low as $0.4J$ [64, 111]. However this is still significantly above the previously stated temperatures where stripe order is expected in Fermi-Hubbard systems. The microscopic origin of the small energy scale can be found in the fermionic nature of the charge carriers. Every dopant is inclined to delocalise in order to reduce its kinetic energy. As soon as dopants are in close proximity with each other, as e.g. in the case of stripe order, delocalisation is suppressed due to the Pauli exclusion principle. At high temperatures at or above the superexchange energy, this is the dominant mechanism which then prevents dopants from forming pairs or stripes (see Fig. 4.7a). Only once the spin order is strong enough to supersede this repulsion, does hole pairing or stripe order become beneficial.

While sufficiently low temperatures remain out of reach for ultracold atom experiments, more exotic couplings present another path to observe stripe order in optical lattices. To remove the dominant effect of Pauli blocking of dopants, one possibility

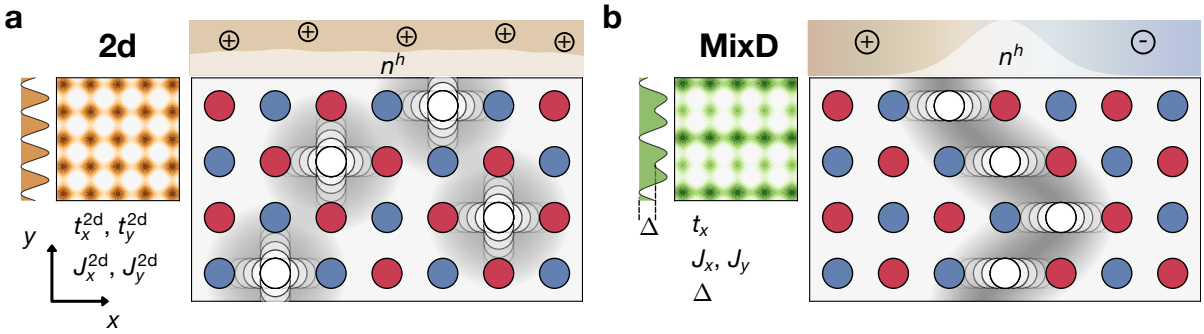

Figure 4.7: Mixed-dimensional Fermi-Hubbard systems. **a**, Illustration of the isotropic 2d Fermi-Hubbard model. Holes delocalise within small regions and disturb their respective spin background, forming magnetic polarons. The overall hole density is uniform and holes repel each other due to their fermionic statistics at experimentally accessible temperatures of $k_B T = 0.4J$. There are no domain walls in the spin order. **b**, By raising the potential on every other lattice site along y by Δ, one can suppress tunnelling along this direction, thus disabling the Pauli repulsion, while preserving the superexchange coupling J_y. The holes form collective structures, which also result in a domain wall in the AFM correlations of the system, indicated by the sign structure at the top.

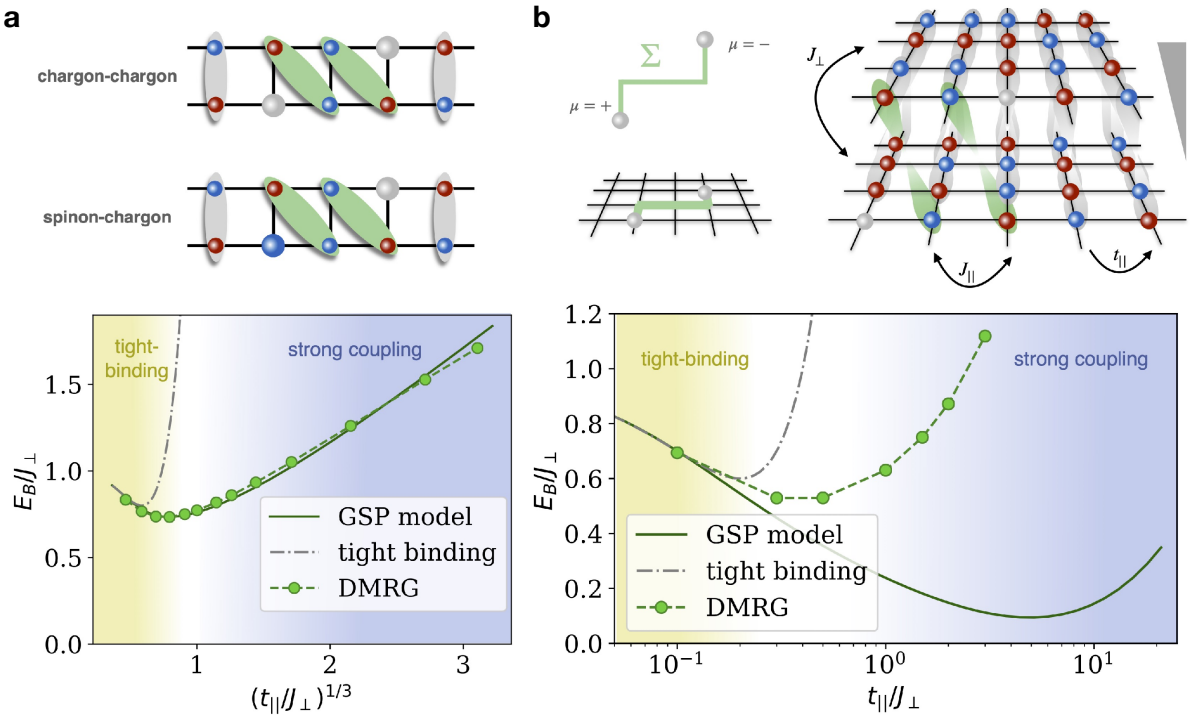

Figure 4.8: Numerical mixD studies on ladder and bilayer systems. **a** (**b**) Binding energy as a function of the ratio $t_\parallel/J_\perp$ for 2-leg ladders (**a**) and bilayer systems (**b**). For $t_\parallel/J_\perp \gg 1$, the binding energy scales as $t_\parallel^{1/3}/J_\perp^{2/3}$. Adapted from [288].

can be found in so-called *mixed-dimensional* (mixD) systems (Fig. 4.7b). These systems are two-dimensional systems where spin exchange coupling is present along both axes while hopping of particles is only possible along one axis. This biases stripe formation along the direction without tunnel coupling as the binding mechanism in the form of the antiferromagnetic spin order still exists. Therefore, without the dominant Pauli blocking, energy scales are increased to more easily accessible regimes. Meanwhile, the general phenomenology of the system is supposed to stay close to the original isotropic Fermi-Hubbard model.

4.2.1 Theoretical mixD studies

Numerically, mixD systems have been studied in recent years, mostly using DMRG. First results in 2-leg ladders revealed hole binding energies slightly below the superexchange coupling J while scaling as $t^{1/3}J^{2/3}$ for $t/J \gg 1$ (see Fig. 4.8) [288]. Similarly, in a mixD bilayer system, pairing between planes was also observed at experimentally accessible temperatures. The results agree (especially in the ladders system)

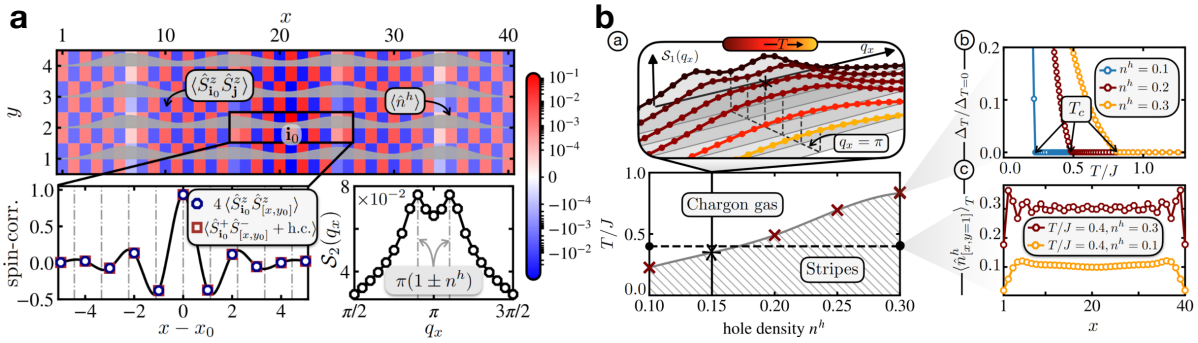

Figure 4.9: Two-dimensional, mixD Fermi-Hubbard systems in DMRG. a, Ground state hole distribution and spin correlations for a system of 40×4 sites and $\delta = 0.1$. The static spin structure factor $\mathcal{S}_2(q_x)$ shows a clear splitting of the peak at $q_x = \pi$, associated with incommensurate magnetism. **b**, Finite temperature calculations. The critical temperature T_c is extracted from the splitting of the static spin structure factor at $q_x = \pi$ and rises with increasing doping. Adapted from [289].

with an effective parton model based on a spinon and chargon connected by a string of displaced spin bonds. Experimentally important, however, is the obtained binding length between two dopants $E_B \propto t_{\parallel}^{1/3} J_{\perp}^{2/3}$. The consequence is that in the regime of strongest binding energy $E_B > J_{\perp}$, the binding length is very large, making it very challenging to observe experimentally.

As an extension of this study, two-dimensional mixD systems were also investigated [289] (see Fig. 4.9). Here, they found stripes at temperatures of $0.5 - 1\,J$, depending on the doping level. A transition from a chargon gas of individual holes to a striped state was extracted using the splitting of the spin structure factor. However, this does not account for potential differences in the transition temperatures between spin and charge stripes, which, as was established in solid state experiments, may differ substantially. Furthermore, small numerical system size may introduce significant finite size effects.

4.2.2 Experimental studies

The aforementioned theoretical mixD proposals led to experimental interest on different platforms. In quantum simulation, improved control of the on-site potential allowed for the observation of paired holes in 2-leg ladders [71] (see Fig. 4.10). Here, we found tightly-bound hole pairs at temperatures slightly below the superexchange energy. Furthermore, the strong Pauli repulsion along the perpendicular direction yielded signatures of Pauli crystals of pairs forming in the ladder (Fig. 4.10b, c). However, no clear signature in the spin sector was found, in agreement with the expecta-

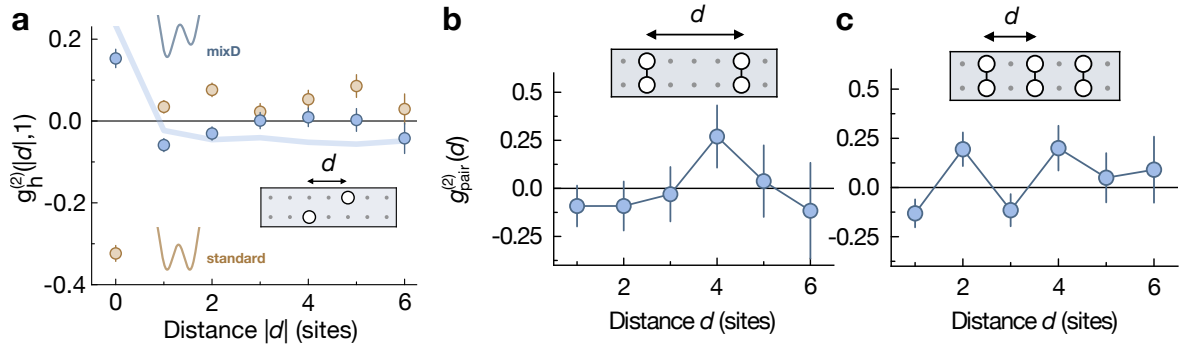

Figure 4.10: Hole pairing in ladders with ultracold atoms. a, Hole-hole correlations as a function of distance in mixD and standard ladders. For mixD ladders, there is a clear signature of tightly bound holes. **b** (**c**), Pair-pair correlations for a doping of 4 (6) holes, showing signs of a Pauli crystal. Adapted from [71].

tion of spin signatures (especially for $J_\perp \gg J_\parallel$) forming at lower temperatures than charge signatures. Finally, recent studies of the bilayer nickelates found critical temperatures of $\sim$ 80K, which according to numerical studies, is related to the mixed-dimensional character of this platform [290–292].

4.3 Preparation of mixD systems

4.3.1 Model and parameter regime

Our quantum gas microscope is uniquely suited to explore mixD systems. The additional couplings that we can introduce using optical superlattices (see section 3.4.5) as well as our full readout of spin and charge degrees of freedom allows for the study of highly controlled systems with system sizes well exceeding what is currently achievable in numerical simulations. We experimentally realise a Fermi-Hubbard type Hamiltonian of Eq. (2.1), where we introduce potential offsets between neighbouring sites along y using our optical superlattice. We now consider the local detuning in more detail. Hopping of particles to an unoccupied neighbouring site is only possible if the detuning between the two sites is sufficiently small, i.e. smaller than the bandwidth W. While for $\Delta > W$ hopping is suppressed, spin coupling between two occupied sites is still possible as it is mediated via virtual intermediate double occupancies. However the effective spin coupling changes as a function of the detuning as stated in Eq. (3.7). Due to the differing signs in the two contributing terms, this leads to several different regimes depending on U/Δ and Δ/W:

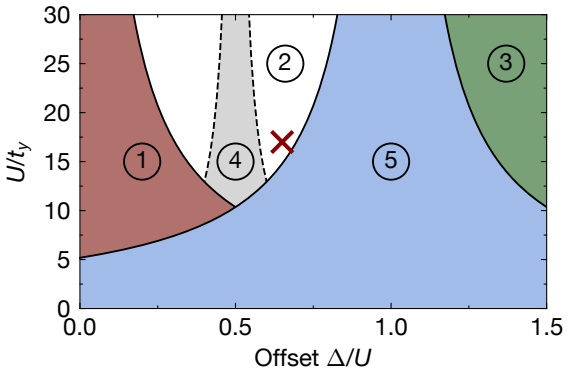

Figure 4.11: Available mixD parameter space. MixD regimes based on potential offset and interactions in a 2d system. For small offsets and large interactions, hopping is not suppressed and an imbalance is created (regime 1). Around $\Delta = U$, doublons are formed (regime 5), while for $\Delta > U$ the spin couplings are ferromagnetic (regime 3). There is a narrow resonance around $\Delta = U/2$ due to the described higher order process, creating doublons and holes (regime 4). The red cross marks the experimental parameters where tunnelling is suppressed with AFM spin couplings (regime 2). Everything is drawn for for a fixed ratio of $t_y/t_x = 27/17$.

1. $\Delta/W < 1$, $U/\Delta < 1$: Hopping is still allowed, antiferromagnetic spin coupling with $J > J_{\Delta=0}$
2. $\Delta/W > 1$, $U/\Delta < 1$: Hopping is suppressed, antiferromagnetic spin coupling
3. $\Delta/W > 1$, $U/\Delta > 1$: Hopping is suppressed, ferromagnetic spin coupling

For the realisation of mixD systems we work in the intermediate regime of suppressed hopping and AFM spin coupling. However, this also leads to restrictions on the possible parameter regime due to conflicting requirements: as the mechanism underlying stripe formation is based on spin coupling, higher values of J/t (i.e. lower values of U/t) are beneficial. On the other hand, for tilts approaching U, we create doublons in the lower chain as the transfer of particles to already occupied sites is then resonant. This transition also has a finite width, reducing the available parameter space as well. Calculations performed to map out the parameter space are shown in Fig. 4.11 and match the described intuitive expectations. Overall, these conditions lead to experimentally rather large values of $U/t_x = 27(2)$ and $U/t_y = 17(1)$ (see Tab. 4.2 for full parameter list). We choose to work with anisotropic parameters where $J_y/J_x \approx 4$. While it is known for 2-leg ladders that the binding energy increases for larger t_x [288, 293], larger values of t_x also lead to stronger fluctuations of charge structures along x, making them experimentally harder to observe. Therefore, using

	2d system	mixD system
t_x	$h \times 163(10)$ Hz	$h \times 163(10)$ Hz
t_y	$h \times 253(13)$ Hz	0 Hz
U	$h \times 4.4(1)$ kHz	$h \times 4.4(1)$ kHz
U/t_x	27(2)	27(2)
U/t_y	17(1)	-
Δ/U	0	0.65(5)
J_x	$h \times 24(4)$ Hz	$h \times 24(4)$ Hz
J_y	$h \times 58(7)$ Hz	$h \times 104(23)$ Hz

Table 4.2: Experimental parameter overview List of coupling strengths used in the experiment after the full preparation procedure described in the text. Where relevant, we denote the couplings in the 2d system in the text with superscripts (e.g. t_y^{2d}).

anisotropic couplings reduces these fluctuation, while the reduced coupling along x makes interactions between several stripes more difficult to realise, limiting the observables available to identify stripes (see section 4.5).

We prepare a system of 109 lattice sites in a circular region which is surrounded by a low-density reservoir required to achieve low temperature (see Fig. 4.12 as well as Fig. 3.12) [155]. For comparison we prepare both 2d and mixD systems. We set the chemical potential to achieve a hole doping of $10-30\%$ by adjusting the height of the surrounding reservoir to be slightly below $U/2$. In total, we collect 11675 experimental realisations, out of which 1254 were taken in a 2d system with $\Delta = 0\,U$, while the remaining 10421 are in the mixD setting with $\Delta = 0.65(5)\,U$. We ensure that there is

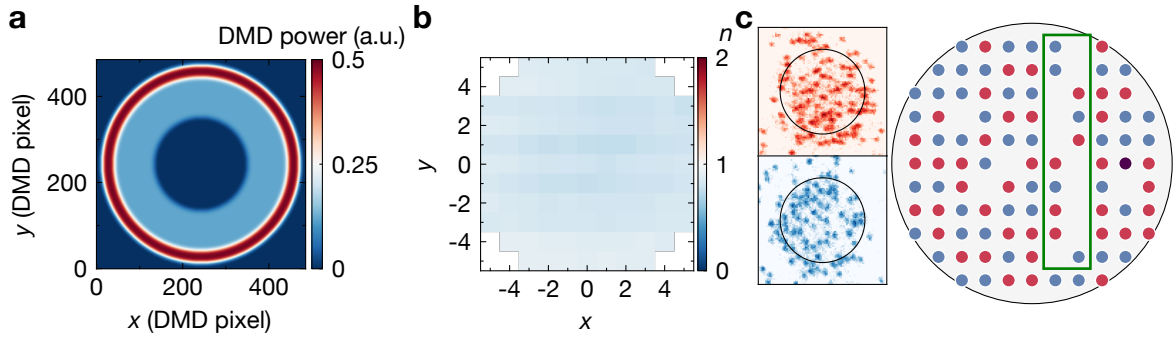

Figure 4.12: MixD system preparation. a, DMD potential for mixD preparation. The main central region is surrounded by a low density reservoir. **b**, Density of central region of 109 sites used for analysis. There is a small residual imbalance due to the preparation process. **c**, Single experimental realisation of spin up (red) and spin down (blue) atoms with their reconstructed occupation.

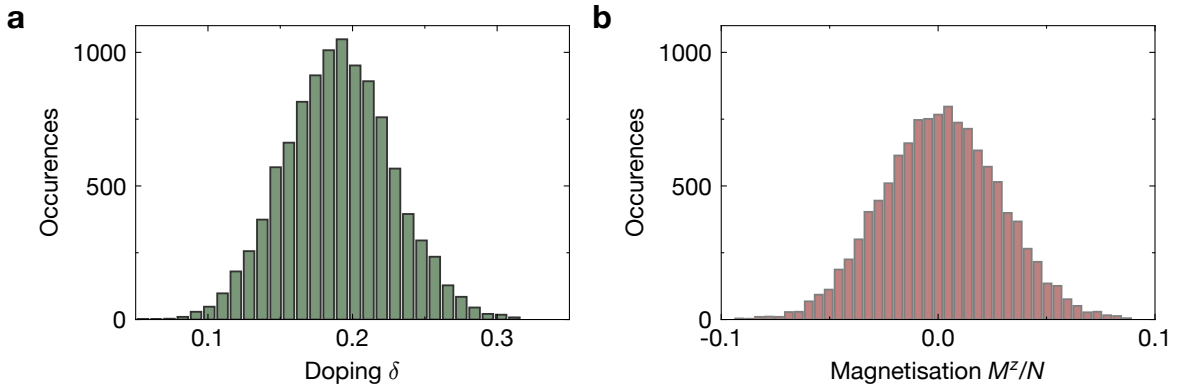

Figure 4.13: Data statistics. Histograms of doping (**a**) and magnetisation (**b**). We take data at 10 to 30% doping while the total magnetisation is well centred around 0.

no overall magnetisation $M^z = \sum_i \langle S_i^z \rangle$ within the system by checking the distribution of magnetisation normalised by the system size (see Fig. 4.13b). We find the width of this distribution to be below shot-noise.

4.3.2 Lattice ramps

To prepare the system at these given settings, care needs to be taken to avoid mass transport during the loading process. Specifically, direct loading into mixD systems from a bulk gas will create a strong occupation imbalance between chains regardless of the final parameters as small potential offsets at intermediate times will still have finite t_y. Therefore a quench into a mixD system is required. In order to avoid heating, we first prepare the system in decoupled 1d chains along x by exponentially ramping the lattices within 200 ms from a 2d gas confined by the vertical lattices and the DMD potential to $V_x = 3\,E_\mathrm{R}$, $V_y = 35\,E_\mathrm{R}$. At this point we quench the superlattice along y within 1 ms to $V_y^\mathrm{SL} = 2\,E_\mathrm{R}$ at $\phi = \pi/2$ to create the desired staggered potential. Finally the lattices are being ramped linearly within 56 ms to their final depths of $V_x = 9\,E_\mathrm{R}$, $V_y = 7\,E_\mathrm{R}$ leading to the parameters as listed in Tab. 4.2. The full ramps and corresponding energy scales are shown in Fig. 4.14.

Further care needs to be taken when considering the interactions as the large changes in the lattice depths during the preparation lead to varying interactions at fixed scattering length. Changes in the interactions during the second part of the ramp might inadvertently introduce doublons into the system due to the resonant process at $\Delta = U$. To avoid this, we set the scattering length such that the interactions in the decoupled 1d chains are already at the desired final value of 4.4 kHz with $a_s = 1160\,a_B$. From then on we adjust the scattering length depending on the instantaneous lattice depths such that the interactions stay constant.

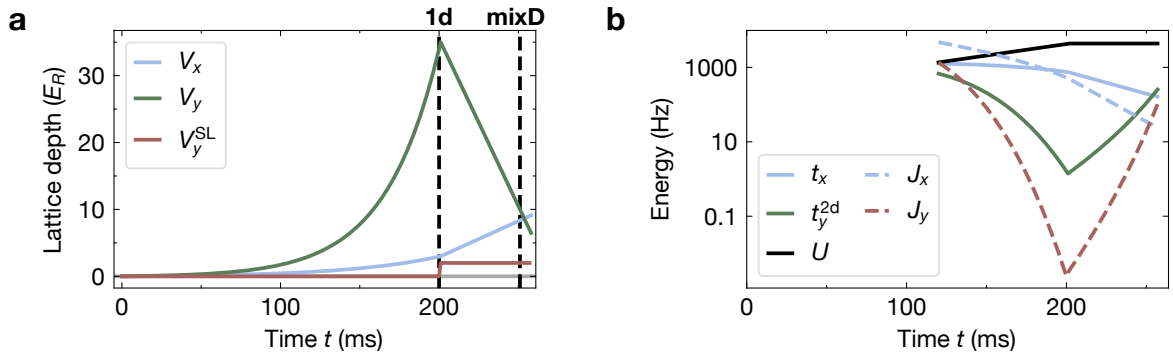

Figure 4.14: Ramps for mixD preparation. **a**, Lattice ramps to prepare the mixD system with the corresponding tunnelling and superexchange couplings plotted in **b**. We first ramp in 200 ms to decoupled 1d chains, then quench the y-superlattice before ramping to the full mixD system.

4.3.3 Calibration

Relative superlattice phase calibration

To controllably apply offsets between neighbouring sites, we calibrate our superlattice potential with two separate methods. First, we determine the relative superlattice phase with high accuracy. For this, similarly to the measurements in section 3.4.2, we adiabatically load a dilute cloud of atoms into a system of decoupled double-wells along y where $V_x = 40\,E_\mathrm{R}$, $V_y = 8\,E_\mathrm{R}$ and $V_y^\mathrm{SL} = 21\,E_\mathrm{R}$. For any small offset between neighbouring sites, the atoms will be loaded into the lower site, creating an imbalance $\mathcal{I} = (\langle\hat{n}_L\rangle - \langle\hat{n}_R\rangle)/(\langle\hat{n}_L\rangle + \langle\hat{n}_R\rangle)$ in the occupation of the system (see Fig. 4.15). We can neglect interactions effects due to the small filling and postselection on double-wells with only one atom. We observe a sharp transition from negative to positive imbalance which we identify as the symmetric phase $\phi = 0$ where the detuning Δ between sites vanishes. For a given intrawell coupling $t_y(\phi = 0) = h \times 724\,\mathrm{Hz}$ between sites, the large slope of the curve points to a high degree of homogeneity of the phase within the system. To realise mixD systems, we work at $\phi = \pi/2$ which is the fully antisymmetric configuration where interwell and intrawell couplings are identical.

Potential offset calibration

While the calibration of lattice depths (via modulation spectroscopy) already yields the potential offset as a function of superlattice depth, we confirm these results and check whether our chosen regime allows for the realisation of mixD systems as expected from the calculations shown in Fig. 4.11. For this purpose, we follow the loading procedure described in the previous section, preparing a slightly hole doped sys-

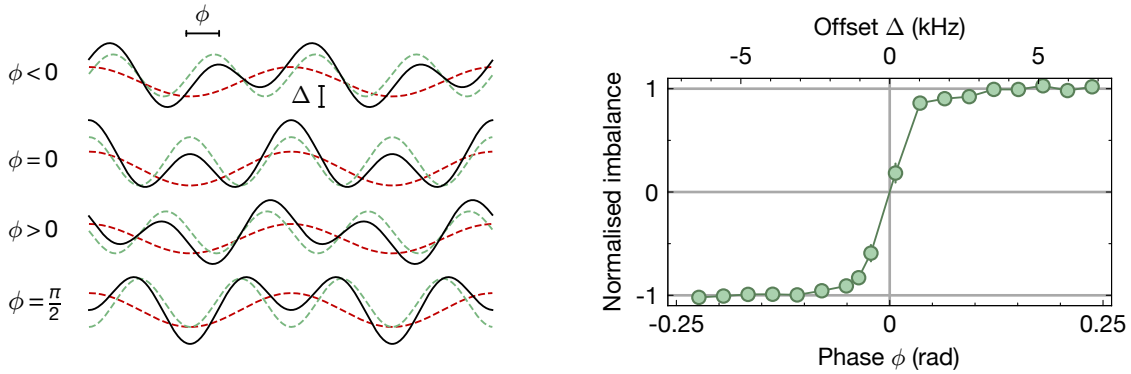

Figure 4.15: Relative superlattice phase calibration. We load a dilute cloud into a deep superlattice ($V_x = 40\,E_\mathrm{R}$, $V_y = 8\,E_\mathrm{R}$ and $V_y^\mathrm{SL} = 21\,E_R$) with different phase and extract the imbalance in occupation between neighbouring chains. At the symmetric double-well configuration ($\phi = 0$) we reach zero imbalance while even for small deviations we quickly occupy only one part of the double-well. All experimental results of this chapter are obtained for $\phi = \pi/2$.

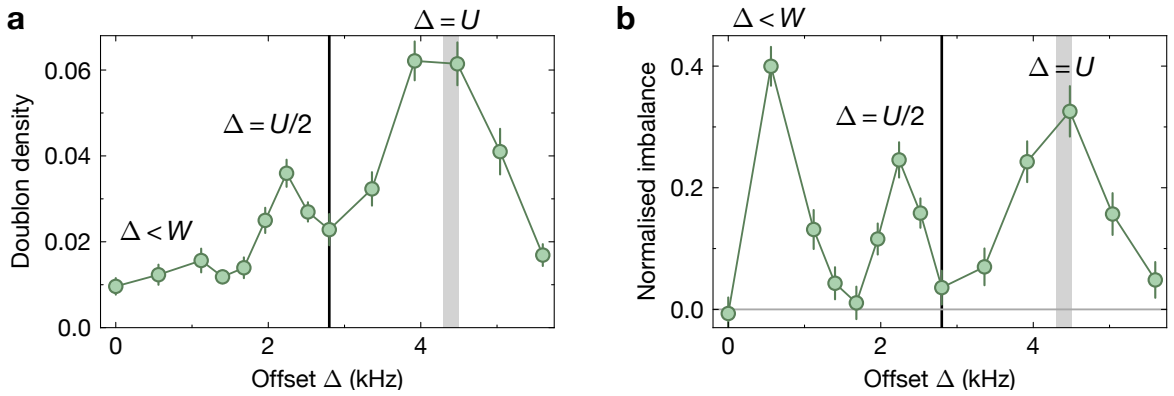

Figure 4.16: Potential offset scan. Doublon density (**a**) and imbalance between chains (**b**) as a function of potential offset Δ (i.e. superlattice power) for a relative superlattice phase of $\pi/2$. The peak in the doublon density coincides with the interaction energy U (grey line) at which atoms are then resonantly transferred to neighbouring chains. For small offsets, tunnelling is not yet fully suppressed and an imbalance is created. Above an intermediate peak at $U/2$ (created by a higher order process), there is a low imbalance regime where the experiment is performed (black line).

tem while varying the superlattice depth to realise different potential offsets. We show the resulting doublon density and imbalance in Fig. 4.16. We clearly identify the different regimes described earlier: initially, for offsets smaller than the bandwidth, hopping is not yet suppressed and atoms will tunnel to the lower chain, creating a strong

imbalance (regime 1). Around $\Delta = U$, if both legs are occupied, doublons are created on the lower chains, increasing both the doublon density and the imbalance (regime 5). In between these two regimes, we see a signature of the higher-order process at $U/2$ which produces doublons in the lower chains from two adjacent atoms in the upper chains (regime 4, see also Fig. 3.24). The position of these resonances match the expectations from band structure calculations. We identify a promising regime above $U/2$ at $\Delta/U = 0.65(5)$ where we can prepare a mixD system with low imbalance.

Thermometry

We use nearest-neighbour spin-spin correlations (as defined in Eq. (3.6)) as a function of doping as a measure for the temperature in our system by comparing to numerical DMRG calculations on a system size of $L_x \times L_y = 8 \times 3$ sites with open boundary conditions. We simulate the mixD $t - J$ model of Eq. (2.3) where couplings are set to $t_y = 0$, $J_y/t_x = 0.5$, $J_x/t_x = 0.15$. Due to the small system size in the simulation, we expect finite size effects in the spin-correlations, especially away from half-filling. This will affect correlations along x and y differently due to the rectangular geometry. For this reason, we extract individual temperatures along x and y per doping level. Averaging over all doping levels per direction yields temperatures of $k_B T/t_x = 0.3(1)$ and $k_B T/t_x = 0.4(1)$ along x and y respectively. The difference in temperature compared to the state-of-the-art reported in section 3.4.1 can be attributed to the very different energy scales due to the large interactions used here, as well as heating during the more elaborate mixD preparation sequence. Note, that correlations along x are mostly independent of doping, which may already hint towards the results in higher-order spin correlators examined in section 4.5.

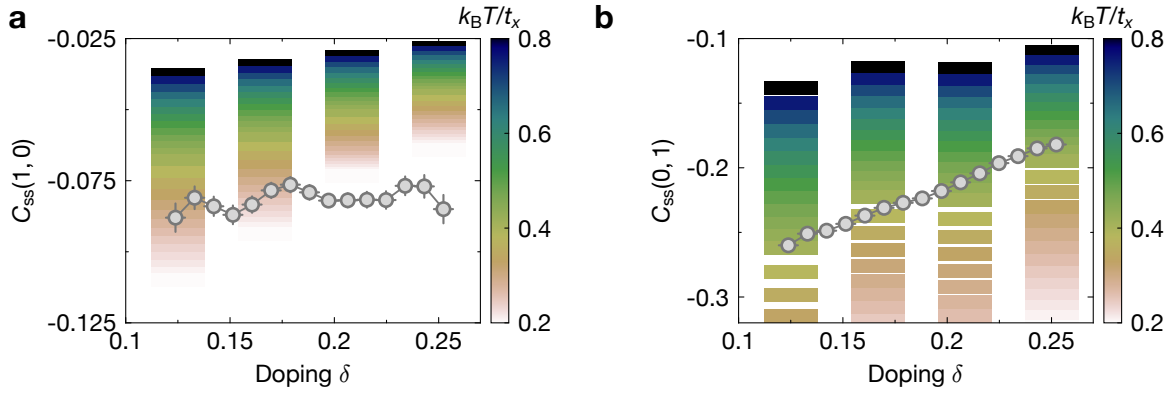

Figure 4.17: Spin-spin correlations as thermometer. Nearest-neighbour spin-spin correlations along x (**a**) and y (**b**) for different doping levels. We compare the experimental (grey markers) to numerical data for $C_{ss}(1)$ for different temperatures for simulations on $L_x, L_y = 8, 3$ and $J_y/t_x = 0.5$ to get an estimate for our temperature.

4.4 Results in the charge sector

One of the main characteristics of stripes is extended charge ordering. Commonly identified via charge structure factors [83], this observable is challenging for our anisotropic parameter regime. However, the microscopic observables in ultracold atoms allow to study arbitrary equal-time spin- or density correlation functions. In the following we show charge correlations indicating stripe ordering in our mixD system.

4.4.1 Correlation functions

For the characterisation of correlations within a system, the N-particle correlation function $G^{(N)}$ is of particular use. It is defined as

$$G^{(N)} = \langle \hat{\mathcal{O}}_1 ... \hat{\mathcal{O}}_N \rangle, \tag{4.1}$$

This can be normalised to $g^{(N)}$ by the individual operator expectation values such that its uncorrelated limit is set to 1.

$$g^{(N)} = \frac{\langle \hat{\mathcal{O}}_1 ... \hat{\mathcal{O}}_N \rangle}{\langle \hat{\mathcal{O}}_1 \rangle ... \langle \hat{\mathcal{O}}_N \rangle}. \tag{4.2}$$

For correlation functions of order 2 and higher, we define a connected correlator by subtracting all combination of lower order correlations. This serves to isolate the specific effect of higher-order correlations from lower-order correlations. For the most common example of two-point correlation functions, this just subtracts the expectation value of the individual operators. In the case of hole-hole correlations, the full connected, normalised, two-point correlator then takes the form of

$$g^{(2)}_{\mathrm{hh}}(\boldsymbol{d}) - 1 = \frac{1}{\mathcal{N}_{\boldsymbol{d}}} \sum_{\boldsymbol{i}} \left(\frac{\langle \hat{n}^h_{\boldsymbol{i}} \hat{n}^h_{\boldsymbol{i}+\boldsymbol{d}} \rangle}{\langle \hat{n}^h_{\boldsymbol{i}} \rangle \langle \hat{n}^h_{\boldsymbol{i}+\boldsymbol{d}} \rangle} - 1 \right) - o_\delta, \tag{4.3}$$

with the fermionic hole operator $\hat{n}^h_{\boldsymbol{i}}$, global offset o_δ and the sum being evaluated over all possible positions $\boldsymbol{i}$ within the system.

This two-point correlator should be close to the interpretation of a probability distribution where it describes the probability for the position a second particle with respect to the first one. However, as we will show in the following section, even fully uncorrelated particles will exhibit finite correlations corresponding to a global offset.

We consider a system of N fermions on V lattice sites with density $n = N/V$ without any further assumptions on the geometry of the system or nature of the fermions. We define the local two-point correlator $\Gamma(i, j) = \frac{\langle \hat{n}_i \hat{n}_j \rangle}{n_i n_j} - 1$ where $n_i = \langle \hat{n}_i \rangle$ is the local

density. After summation over all possible pairs of sites i, j, this can be expressed as

$$\sum_{i,j} \Gamma(i,j) = \sum_{i,j} \left(\frac{\langle \hat{n}_i \hat{n}_j \rangle}{n_i n_j} - 1 \right) \approx \left(\frac{\langle \hat{N}^2 \rangle}{n^2} - V^2 \right), \tag{4.4}$$

where we used $\hat{N}^2 = \sum_{i,j} \hat{n}_i \hat{n}_j$ and assumed a homogeneous system such that and $n_i \approx n_j \approx n$. This yields

$$\frac{1}{V^2} \sum_{i,j} \Gamma(i,j) = \frac{\mathrm{Var}(\hat{N})}{N^2}. \tag{4.5}$$

Without any further assumptions, we can simplify this sum by splitting off the on-site term where $i = j$ using fermionic statistics $\hat{n}^2 = \hat{n}$ (and thus $\Gamma(i,i) = \frac{1}{n} - 1$), leading to

$$\frac{1}{V^2} \sum_{i \neq j} \Gamma(i,j) = \frac{\mathrm{Var}(\hat{N}) - N(1-n)}{N^2}. \tag{4.6}$$

This expression now allows us to consider a few specific cases. First of all, we note that in general the right-hand-side of this equation can be non-zero even at infinite temperature. This contradicts the intuition that at sufficiently high temperatures, there should be no correlations present within the system. Instead, this only holds in certain situations where the global fluctuations are also fermionic (i.e. multinomial such that $\mathrm{Var}(\hat{N}) = N(1-n)$). Alternatively in the thermodynamic limit $N \to \infty$, where usually $\mathrm{Var}(\hat{N})$ scales as $1/N$ or less, the expression vanishes as well.

Experimentally we find that when computing hole-hole correlations on the full dataset, the fluctuations are close to multinomial such that the expression of Eq. (4.6) is small. However, by evaluating correlations for specific doping levels, the variance within this subset is different, which in turn leads to large correlator offsets. For this reason we define the offset o_δ in Eq. (4.3) to be

$$o_\delta = \frac{\mathrm{Var}(\hat{N}^h) - N^h(1-n^h)}{(N^h)^2}, \tag{4.7}$$

such that we recover vanishing correlations for $i \neq j$ for infinite temperature. We note that this offset is global and does not depend on distance $d = i - j$. Furthermore, it is only relevant when evaluating correlations on subsets of data. Whenever we evaluate correlations on the full dataset, no offset correction is required.

4.4.2 Hole-hole correlations

We evaluate the two-point correlator of Eq. (4.3) for $t_y = 0$ and a doping of $\delta = 0.18$ and show the symmetrised result as a function of distance $\boldsymbol{d}$ in Fig. 4.18. Most prominently, we observe strong positive correlations at the nearest distance along y for

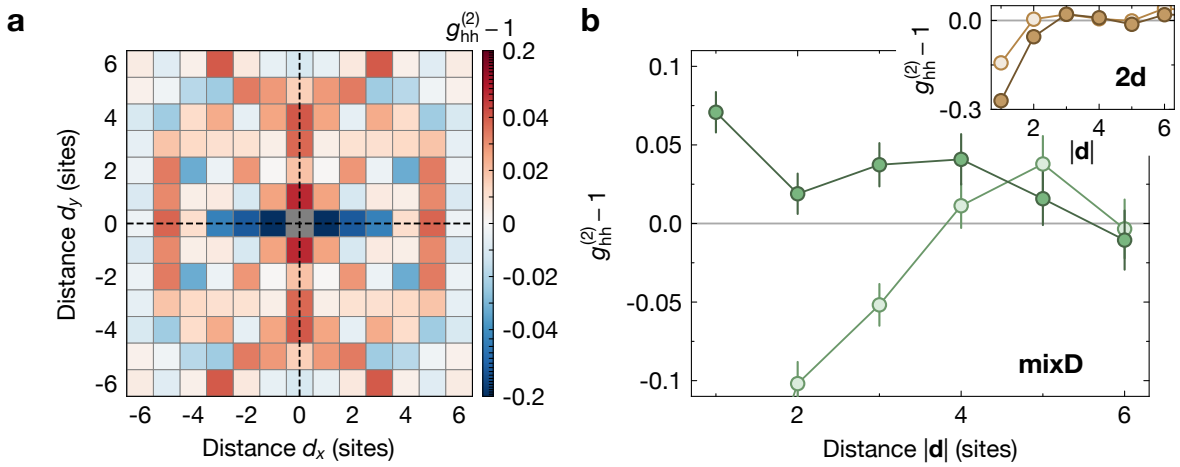

Figure 4.18: Extended mixD hole-hole correlations. a, Symmetrised hole-hole correlations in a mixD system for $\delta = 0.18$. We observe extended positive correlations for $d_y \geq 1$ and strong Pauli anticorrelations for $d_y = 0$. Positive signals at $d_x = 5$ hint towards the presence of a second charge structure in the system. **b**, Cuts along x (y) in light (dark) green for the mixD system with the outset showing the equivalent data for a normal 2d system. Error bars are estimated using bootstrapping.

$d_x = 0$. However, even at larger distances $d_y > 1$, the correlations remain positive. This is indicative of charge structures that exceed pairing of holes at closest distances as larger stripe-like configurations of holes begin to form. Furthermore, positive correlations along the diagonals (i.e. $\boldsymbol{d} = (\pm 1, 1)$) show that the emerging charge structures are not fully static along x. While we work at an anisotropic parameter regime, hopping along x is of a similar order of magnitude as the superexchange along y (which is then related to stripe formation). Therefore, charge fluctuations along x are not fully suppressed which in turn may decrease signals at larger distances for $d_x = 0$. We also clearly observe the effect of the next-nearest-neighbour hopping term studied in Ch. 3 as it leads to lowered correlations at distance $d_y = 2$. We are still able to observe positive correlations as the spin exchange dominates over next-nearest-neighbour hopping $\tilde{t}_y \approx 0.8 J_y$ (see also section 3.4.3).

Along x, the main feature for $d_y = 0$ is a strong anticorrelation at short distances which is expected due to the Pauli repulsion of holes within the same chain. However, at distance $d_x = 5$, there are weak positive correlations for $d_y \leq 2$. This may point towards the presence of a second stripe-like structure beginning to form within the system.

We also compare this to a normal 2d system with both $t_x, t_y^{\mathrm{2d}} \neq 0$ (see inset of Fig. 4.18b). In this case, we only observe anticorrelations along both directions as the Pauli repulsion vastly dominates over the effective attraction via the superexchange

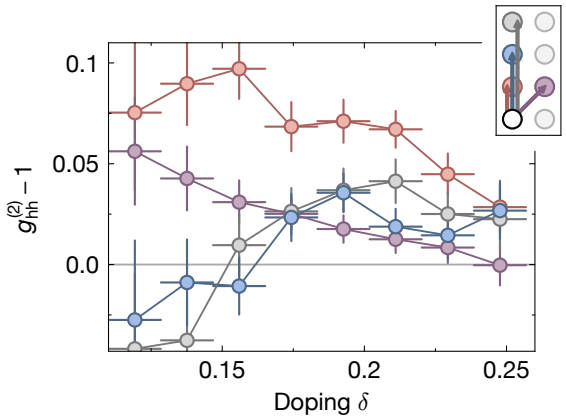

Figure 4.19: MixD hole-hole correlations by doping level. For distances $\boldsymbol{d} = (0,1),(1,1),(0,2),(0,3)$ we show the corresponding mixD hole-hole correlations in red, purple, blue, grey as a function of doping with a binning of ± 0.009. Around $\delta = 0.2$, correlations at larger distances $d_y > 1$ become positive. Error bars are estimated using bootstrapping.

coupling. Comparing the Pauli repulsion along x for mixD and 2d, it can be seen that removing the Pauli repulsion along y strengthens the anticorrelations along x as there is no more competition between the two directions.

By binning the data by doping level, we study the evolution of mixD hole-hole correlations at specific distances as a function of doping (see Fig. 4.19). For nearest-neighbour and diagonal distances, we observe a decrease of correlations with doping. As spin correlations along y are responsible for binding in our system, they can be linked to the presence of charge structures within the system. However, as shown in Fig. 4.17, spin correlations decrease with increasing doping, which in turn decreases the effective attraction between charges along y and thus the correlations. This only easily holds for $d_y = 1$, while for larger distances the situation is more complicated. Due to the preparation from 1d chains, the doping level in each individual chain is probabilistic. Therefore, for low doping levels, the probability to have dopants in three or more neighbouring chains is low such that there are mostly only individual holes or pairs of holes present. Meanwhile, at very high doping level, even the pair formation probability decreases as explained above, such that no larger structures form either. Thus only in an intermediate regime, that we find to be around $\delta \sim 0.2$, are longer-ranged correlations present in our system. This may be interpreted as a transition from individual hole pairs, to larger stripe-like structures, to a chargon gas of unbound holes.

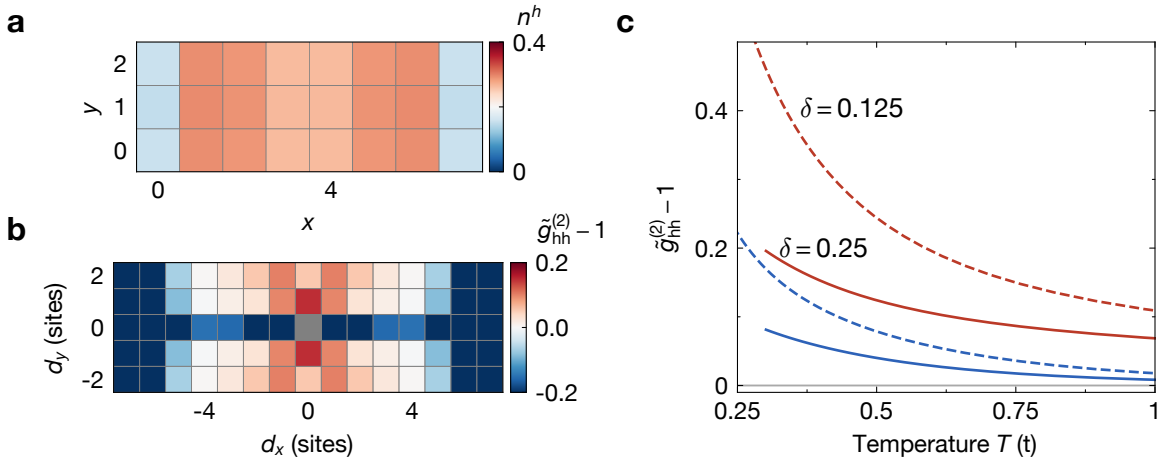

Figure 4.20: Numerical hole-hole correlations. a, Hole density from DMRG for $L_x \times L_y = 8 \times 3$, $\delta = 0.25$, $k_B T/t_x = 0.41$. Two separate stripes at a distance of ~ 4 sites are found in the system. **b**, Renormalised hole-hole correlations as a function of distance. As in the experiment, the strongest signal is for $\boldsymbol{d} = (0, 1)$ but there are also significant contributions at $\boldsymbol{d} = (1, 1)$ due to fluctuations along x. **c**, Hole-hole correlations as a function of temperature for $d_y = 1$ (red) and $d_y = 2$ (blue) for $\delta = 0.125$ (dashed lines) and $\delta = 0.25$ (solid lines).

Theory comparison

To compare these results to theory, DMRG calculations of the mixD $t - J$ model were performed by our theory collaborators. Due to the fermion sign problem, numerical simulations of this model are very computationally expensive and limited in system size. This makes quantitative comparison hard due to finite size effects only present in the simulation. When using open boundary conditions, this will introduce sharp edges. This can immediately be seen when considering the density for a given doping level. While experimentally the density is homogeneous, in the numerical data the dopants aggregate in the centre of the system to increase their kinetic energy by avoiding the edges (see Fig. 4.20). For a fully pinned stripe, the connected correlator introduced in Eq. (4.3) vanishes as the contribution from the density is explicitly subtracted. To partially mitigate this issue, we introduce the renormalised correlator

$$\tilde{g}^{(2)}_{\mathrm{hh}}(\boldsymbol{d}) = \frac{1}{\mathcal{N}_{\boldsymbol{d}}} \sum_{\boldsymbol{i}} \left(\frac{\langle \hat{n}^h_{\boldsymbol{i}} \hat{n}^h_{\boldsymbol{i}+\boldsymbol{d}} \rangle}{n^h n^h} - 1 \right), \tag{4.8}$$

where instead of using the local density n_i in the denominator, we use the global density $n_h = \delta$. In the limit of a perfectly homogeneous system, this is equivalent to Eq. (4.3).

We show hole-hole correlations as a function of distance for $\delta = 0.25$ and $k_B T/t_x = 0.41$ in Fig. 4.20b and for specific distances as a function of temperature in Fig. 4.20c. Quantitative comparison to experimental results is hard due to several reasons. First of all, the small system size along y leads to significant finite size effects and effectively increases the obtained hole-hole correlations. Furthermore, the calculations do not include the next-nearest-neighbour hopping term, which is present in the experiment. Finally, in the experiment in each realisation the global doping level can vary significantly from the local doping level in each individual chain as it depends entirely on how dopants are distributed between individual 1d chains. This means that there are realisations where despite the global doping level being optimal for the formation of charge structures, the distribution between chains may not allow such configurations. Meanwhile, in the simulation global and local doping levels are identical. Therefore the values in the experiment are further lowered compared to the the simulation.

4.4.3 Multi-point charge correlations

The two-point hole correlator $g^{(2)}_{\mathrm{hh}}$ shown so far reveals nearest-neighbour pairing between holes and shows correlations that extend over larger distances. Whether these are isolated pairs or larger charge structures is however not entirely clear from this observable. To study the interactions of pairs with other dopants and pairs, we define a pair as two directly adjacent holes with distance $\boldsymbol{d}^h = (0, 1)$ such that $\hat{n}^p_{\boldsymbol{i}} = \hat{n}^h_{(i_x,i_y)}\hat{n}^h_{(i_x,i_y+1)}$. This is a valid definition as we have shown before that these pairs are present (see Fig. 4.18). However, the significant fluctuations along x seen previously are neglected for simplicity in this case. Therefore, the charge ordering in the system, as extracted from these pairs, may be underestimated. We then consider the 'partially connected' pair-hole and pair-pair correlators

$$g^{(2)}_{\mathrm{ph}}(\boldsymbol{d}) - 1 = \frac{1}{\mathcal{N}_d}\sum_{\boldsymbol{i}}\left(\frac{\langle \hat{n}^p_{\boldsymbol{i}}\hat{n}^h_{\boldsymbol{i}+\boldsymbol{d}}\rangle}{\langle \hat{n}^p_{\boldsymbol{i}}\rangle\langle \hat{n}^h_{\boldsymbol{i}+\boldsymbol{d}}\rangle} - 1\right), \tag{4.9}$$

and

$$g^{(2)}_{\mathrm{ph}}(\boldsymbol{d}) - 1 = \frac{1}{\mathcal{N}_d}\sum_{\boldsymbol{i}}\left(\frac{\langle \hat{n}^p_{\boldsymbol{i}}\hat{n}^p_{\boldsymbol{i}+\boldsymbol{d}}\rangle}{\langle \hat{n}^p_{\boldsymbol{i}}\rangle\langle \hat{n}^p_{\boldsymbol{i}+\boldsymbol{d}}\rangle} - 1\right). \tag{4.10}$$

These are still technically only connected two-point correlators, just between pairs instead of individual holes. They may also be interpreted as 3-point (Eq. (4.9)) and 4-point (Eq. (4.10)) correlators where contributions involving the two holes in the pair individually are not subtracted.

The results for these correlators applied to the data is shown in Fig. 4.21. For improved statistics we do not select any doping level but use the full dataset as shown in

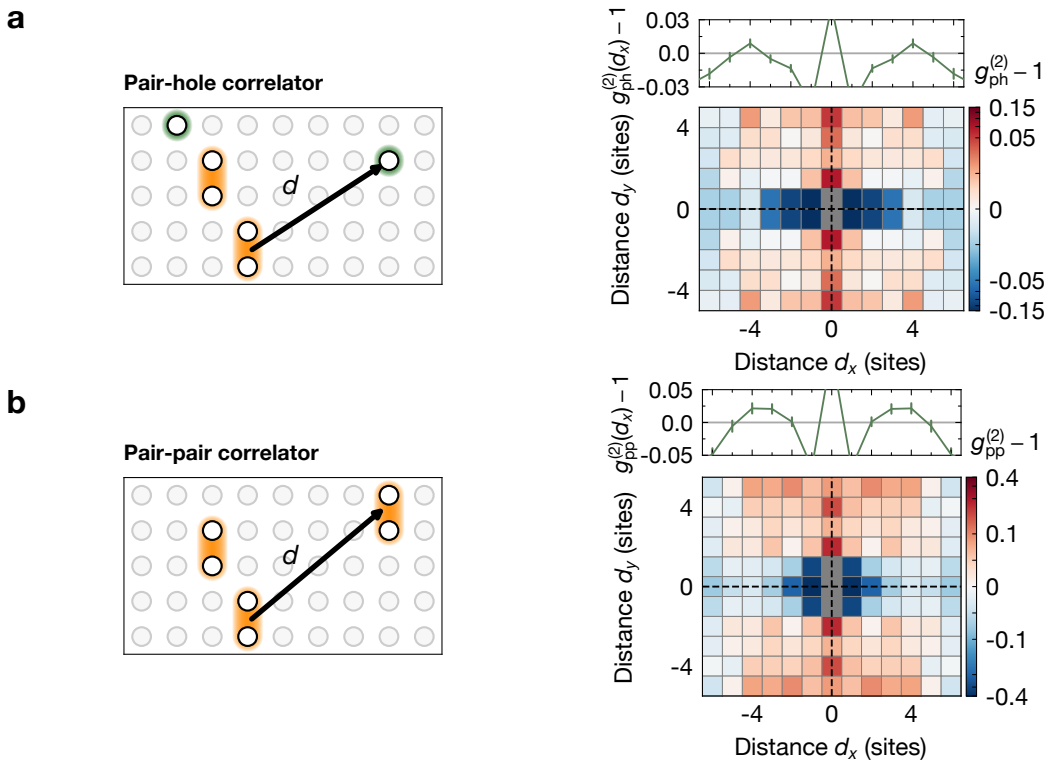

Figure 4.21: Pair correlations. Symmetrised pair-hole (**a**) and pair-pair (**b**) correlation maps with pairs being defined as nearest-neighbouring holes along y. We observe positive correlations at $d_y \geq 1$ extending through the system in addition to diagonal contributions. Averaging over y shows a maximum at $d_x = 4$, potentially related to another stripe-like structure forming.

Fig. 4.13. We observe positive correlations at nearest distances along y for both correlators. This already shows that pairs do not repel each other. Instead, they align along y and form stripe-like structures that extend far through the system. Along x the main feature is the strong anticorrelation due to the Pauli repulsion of the individual holes in the pair. However, when averaging over all distances along y, the correlations are slightly positive at $d_x \approx 4$ (see cut on top of correlation maps). Similar to the signal found in Fig. 4.18, this may be a second stripe-like structure in the system forming at that distance. It is found at a smaller distance than the previous signature in the hole-hole correlator. This may be due to more dopants being available at higher doping levels (which is relevant here as all doping levels are included for this correlator), reducing the average optimal distance between stripes. Both signatures may be seen as the onset of a charge density wave.

As mentioned before, there are several contributions to a fully connected multi-

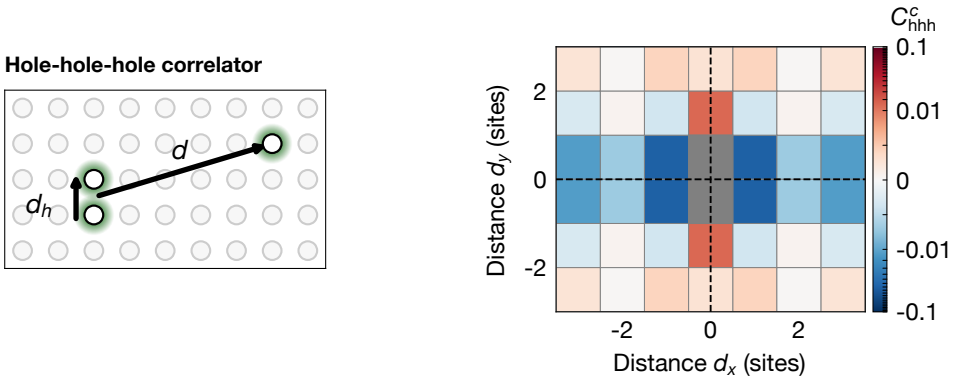

Figure 4.22: Connected 3-point correlations. Connected hole-hole-hole correlations as a function of distance where the distance between two of the holes $\boldsymbol{d}^h = (0,1)$. There is a positive signal for $\boldsymbol{d} = (0,1.5)$ which indicates that holes are attracted to each other beyond pair formation.

point correlator neglected in Eq. (4.9). By adding these additional terms, we consider whether it is favourable for a third hole to be added to a pair in excess of the pair formation probability associated with the individual two-point correlations between the first two holes and the third one. The fully connected, three-point hole-hole-hole correlator is defined as

$$C^c_{\mathrm{hhh}}(\boldsymbol{d}^h,\boldsymbol{d}) = \frac{1}{\mathcal{N}_{\boldsymbol{d}^h,\boldsymbol{d}}} \sum_{\substack{i \\ j=i+\boldsymbol{d}^h/2+\boldsymbol{d}}} \frac{1}{\langle \hat{n}^h_i\rangle\langle \hat{n}^h_{i+\boldsymbol{d}^h}\rangle\langle \hat{n}^h_j\rangle} \times$$
$$\left(\langle \hat{n}^h_i \hat{n}^h_{i+\boldsymbol{d}^h}\hat{n}^h_j\rangle - \langle \hat{n}^h_i \hat{n}^h_{i+\boldsymbol{d}^h}\rangle\langle \hat{n}^h_j\rangle - \langle \hat{n}^h_i\rangle\langle \hat{n}^h_{i+\boldsymbol{d}^h}\hat{n}^h_j\rangle - \langle \hat{n}^h_i \hat{n}^h_j\rangle\langle \hat{n}^h_{i+\boldsymbol{d}^h}\rangle + 2\langle \hat{n}^h_i\rangle\langle \hat{n}^h_{i+\boldsymbol{d}^h}\rangle\langle \hat{n}^h_j\rangle\right). \tag{4.11}$$

We show the value of this correlator for $\boldsymbol{d}_h = (0,1)$ as a function of distance $\boldsymbol{d}$ in Fig. 4.22. The only feature significantly deviating from zero here is the positive signal at $\boldsymbol{d} = (0,1.5)$. This is a striking result as it shows that larger structures are not simply 'stacked pairs', but instead are energetically favourable beyond individual pairs. It also shows that simple two-point correlations are not able to capture the full physical picture of stripe formation, further highlighting the strength of quantum gas microscopy.

4.4.4 Stripe identification

All correlators shown so far have significant diagonal contributions due to the coupling along x. To be able to study charge structure formation despite these fluctuations, we want to define an observable that directly identifies stripe-like structures. As

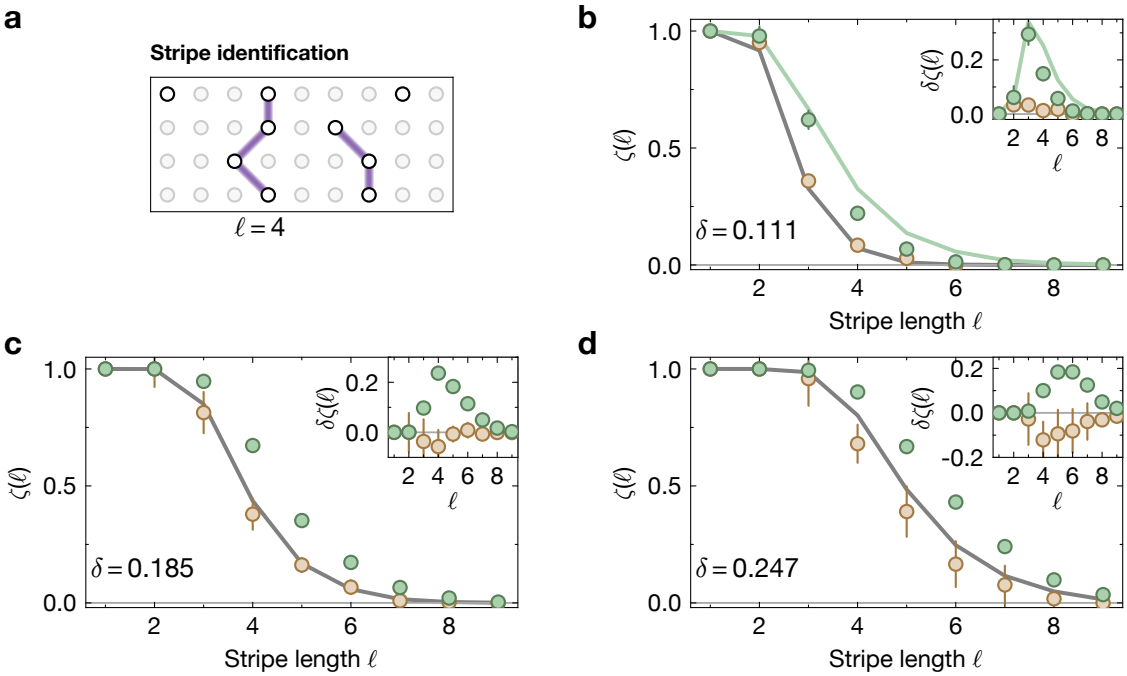

Figure 4.23: Identification of stripe-like structures. By identifying stripe-like structures in individual snapshots (**a**, see text), we calculate the histogram of stripe lengths for mixD (green points) and 2d (brown points) systems for several doping levels (**b-d**). For comparison, we show random distributions of holes including Pauli repulsion along x (grey lines, see text) and calculate the difference in the insets. We use an effective mean field theory (see text) to describe the low doping behaviour and find good agreement for $k_\mathrm{B}T/t_x = 0.355$ (green line in **b**).

we have access to individual snapshots in our quantum gas microscope, we identify a 'stripe' as a continuous line of holes along y. To allow for fluctuations along x, we include any structures where the distance along x between holes in adjacent chains is at most 1 (see Fig. 4.23a). We denote the length ℓ of such a structure by the number of involved chains along y and then label the snapshot with the longest length found. This analysis is performed on a subregion of 9×9 sites to avoid effects from chains of different length within the system. The fraction ζ of experimental realisations containing a 'stripe' of length at least ℓ for several different doping levels is shown in Fig. 4.23b-d where we compare mixD measurements (green) with 2d measurements (brown). There is a clear difference between the two systems with mixD measurements favouring longer structures compared to 2d systems.

To provide a more meaningful interpretation to this observable, we compare the measured fraction ζ with randomly generated data. Depending on the assumptions involved in generating this data, quantitative differences may arise, while we find

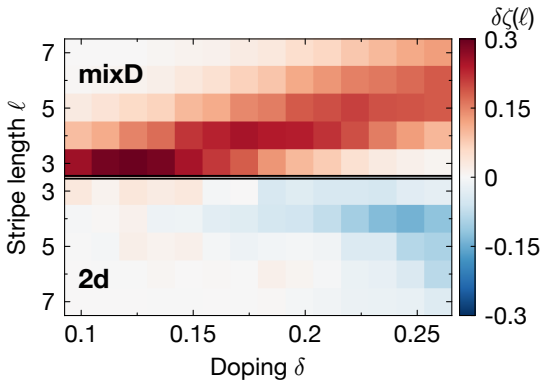

Figure 4.24: Doping analysis of stripe length histograms. Comparing the stripe length histograms of Fig. 4.23 to random distributions, we calculate the full doping dependence for mixD (top) and 2d systems (bottom). Excess occurrences tend towards longer lengths with larger doping.

results to stay qualitatively the same. Here, we chose to include the strong Pauli repulsion between holes along x by sampling holes according to the measured anti-correlations as shown in Fig. 4.10b. This repulsion could in principle lead to structures of increased length in finite systems and sufficiently high doping levels compared to fully randomly distributed holes. The resulting data is shown as grey lines in Fig. 4.23. The difference between the random data and the experimental data $\delta\zeta$ is shown in the corresponding insets. We also show the full distribution as a function of doping in Fig. 4.24. We find an excess of stripes for all doping levels of mixD while the 2d system is consistent with randomly distributed holes. This corroborates the interpretation of long charge structures forming in the system as extracted from the two- and three-point correlation analysis.

Effective theories for stripe length analysis

Full numerical simulation of this is out of reach as system sizes typically do not exceed $L_y = 3$ ($L_y = 4$ under some circumstances), which is much smaller than the experimental size of $L_y = 9$. Therefore we rely on effective theories to compare to our data. We show a mean-field theory (MFT) at $k_B T/t_x = 0.355$ in Fig. 4.23b (green line) and find good agreement with the measured mixD results. We give a brief summary of the theories here with more details to be found in [206].

First, we consider a mean-field model where we assume to have exactly one hole per chain described by the mixD $t - J$ model. For $t_x/J_{x/y} \ll 1$, we can use the frozen spin approximation where spin wave functions (in squeezed space) and charge wave functions can be separated. Using this ansatz, we can then define an effective inter-

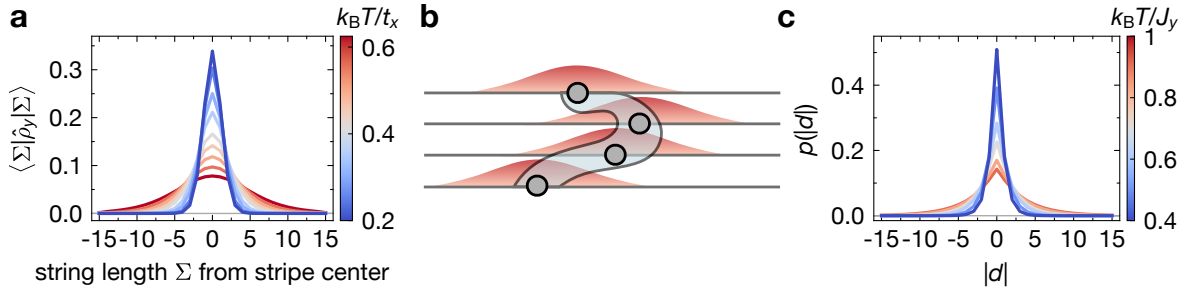

Figure 4.25: Effective models for stripe identification. **a** Thermally averaged string length distribution for a mean field model for temperatures of $k_BT/t_x \in [0.2, 0.625]$ and $t_x/J_y = 2$. Thermal correlations in the Heisenberg model are taken from DMRG calculations with $J_x/J_y = 0.3$. **b**, Illustration of MHZ estimate where hole positions are sampled according to the red probability distributions, whereby the distribution for position $x_l + 1$ is centred around x_l – capturing fluctuating, extended stripes. **c**, Hole distance distributions for various temperatures $k_BT/J_y \in [0.4, 0.91]$.

chain potential between holes that are separated by a string of displaced spins Σ along x. This potential is extracted from nearest-neighbour and diagonal spin correlations along y in the undoped Heisenberg model for $J_x/J_y = 0.3$. Finally, we can use exact diagonalization to determine the distribution of these string lengths (related to the distance a hole has travelled from the centre of a stripe), see Fig. 4.25a.

Alternatively, we also employ a classical model using the Müller-Hartmann-Zittartz (MHZ) approach. Here we reduce the problem to 1d systems of fluctuating holes, bound by an effective potential (again with exactly one hole per chain), Fig. 4.25b. As before, we use the Heisenberg spin correlations to describe the effective potential $V_{\text{pot}}(|d|;T)$ and then sample the distance d of holes from the centre according to the probability distribution

$$p(d) = \exp[-\beta V_{\text{pot}}(|d|;T)] \Big/ \left(\sum_{d=-L_x}^{L_x} \exp[-\beta V_{\text{pot}}(|d|;T)] \right). \tag{4.12}$$

The resulting distribution is shown in Fig. 4.25c.

We compare both approaches to experimental data in Fig. 4.26. We find agreement with measurements for temperatures around $k_BT/t_x \approx 0.3$, matching the estimations from spin correlations. However, for both models, effective theories slightly overestimate the amount of order compared to the experimental results.

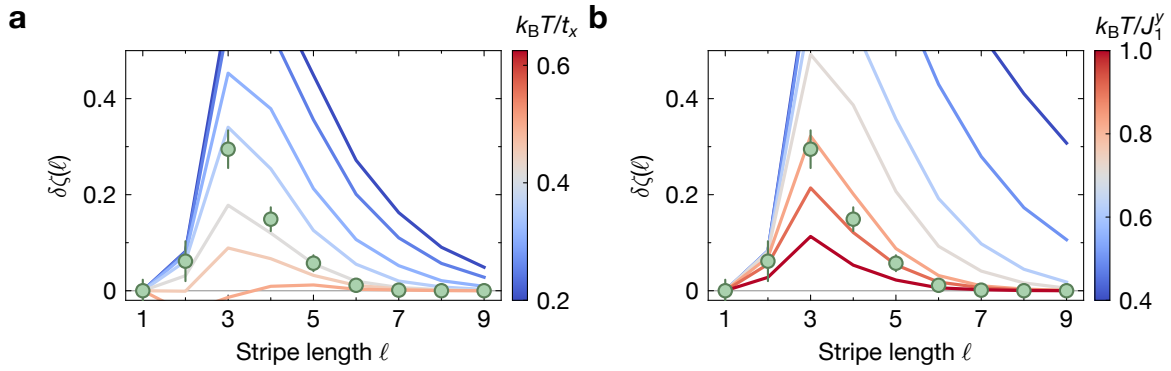

Figure 4.26: Comparison of effective models and experimental data.. Difference of MFT stripe length histograms to random distribution for $k_BT/t_x \in [0.2, 0.625]$ and $J_x/J_y = 0.3$ (**a**) as well as classical MHZ results for $k_BT/J_1^y \in [0.4, 0.91]$ (**b**). Experimental data for $\delta = 0.111$ is shown as green markers.

4.5 Results in the spin sector

In many materials exhibiting charge density wave ordering[2], charge ordering goes hand in hand with the formation of a related spin density wave where the parity of the AFM pattern changes at the position of the stripes. However, due to the rather short-ranged spin correlations along x in our anisotropic system, we do not have large, global AFM domains but instead only local AFM patches. This means that common signatures, such as weight in the spin structure factor away from (π, π), are not to be expected in our parameter and temperature range. Instead, we rely on more local observables to extract the spin ordering at the onset of charge ordering.

4.5.1 Spin-charge correlations

First we investigate three-point spin-charge correlations, similar as to what has previously been studied in much detail in isotropic 2d systems (see section 4.1.4). In a similar fashion, we employ a hole-spin-spin correlator, which allows us to determine the effect of individual dopants on the local spin correlations. For this we define the normalised, bare hole-spin-spin correlator as

$$C_{\text{hss}}(\boldsymbol{d}^s, \boldsymbol{d}^h) = \frac{1}{\mathcal{N}_{\boldsymbol{d}^s,\boldsymbol{d}^h}} \sum_{\substack{\boldsymbol{i} \\ \boldsymbol{j}=\boldsymbol{i}+\boldsymbol{d}^h-\boldsymbol{d}^s/2}} \frac{\langle \hat{n}_{\boldsymbol{i}}^h \hat{S}_{\boldsymbol{j}}^z \hat{S}_{\boldsymbol{j}+\boldsymbol{d}^s}^z \rangle}{\langle \hat{n}_{\boldsymbol{i}}^h \rangle \sigma(\hat{S}_{\boldsymbol{j}}^z) \sigma(\hat{S}_{\boldsymbol{j}+\boldsymbol{d}^s}^z)}, \tag{4.13}$$

[2]but not all materials, e.g. YBCO [294]

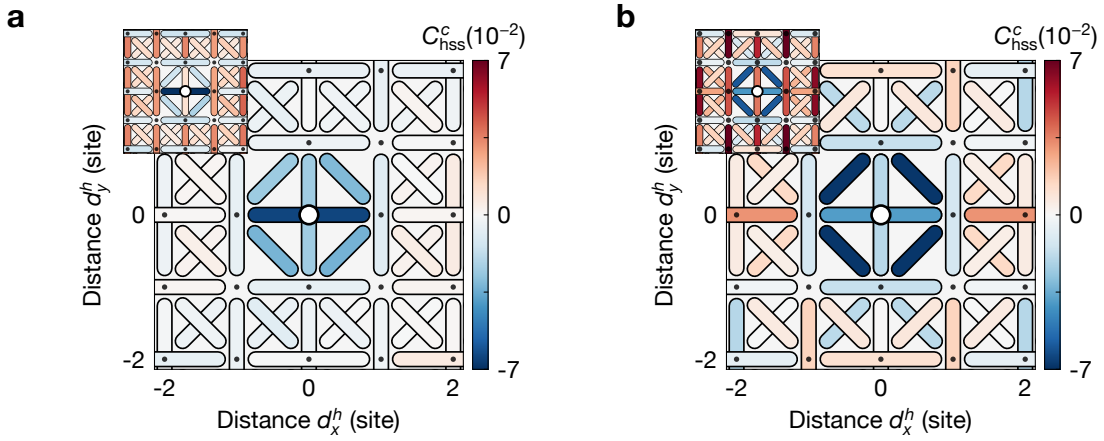

Figure 4.27: Spin-charge correlations. Hole-spin-spin correlations in the experiment (**a**) and theory (**b**, $\delta = 0.125$, $k_B T/t_x = 0.4$). The main figures show the connected correlators while the inset is the same data with only the bare correlator. The bond across the hole at distance $\boldsymbol{d}^s = (2,0)$ is strongly negative, consistent with the onset of a domain wall in the local AFM pattern.

where $\boldsymbol{d}^s$ is the spin bond vector, $\boldsymbol{d}^h$ the distance of the bond from the dopant and we normalise by hole density $\langle \hat{n}^h \rangle$ and the spin standard deviation $\sigma(\hat{S}^z)$. This correlator directly measures the total spin environment around a hole. For some applications it might be more interesting to consider what is the effect of the hole on the spin background by subtracting out the background AFM pattern. We do this by defining the connected correlator as

$$C^c_{\mathrm{hss}}(\boldsymbol{d}^s, \boldsymbol{d}^h) = \frac{1}{\mathcal{N}_{\boldsymbol{d}^s,\boldsymbol{d}^h}} \sum_{\substack{\boldsymbol{i} \\ \boldsymbol{k}-\boldsymbol{j}=\boldsymbol{d}^s, \\ (\boldsymbol{k}+\boldsymbol{j})/2-\boldsymbol{i}=\boldsymbol{d}^h}} \frac{\langle \hat{n}^h_{\boldsymbol{i}} \hat{S}^z_{\boldsymbol{j}} \hat{S}^z_{\boldsymbol{k}} \rangle - C_{\mathrm{disc}}}{\langle \hat{n}^h_{\boldsymbol{i}} \rangle \sigma(\hat{S}^z_{\boldsymbol{j}}) \sigma(\hat{S}^z_{\boldsymbol{k}})} \tag{4.14}$$

where we used the disconnected part

$$C_{\mathrm{disc}} = \langle \hat{n}^h_{\boldsymbol{i}} \rangle \langle \hat{S}^z_{\boldsymbol{j}} \hat{S}^z_{\boldsymbol{k}} \rangle + \langle \hat{n}^h_{\boldsymbol{i}} \hat{S}^z_{\boldsymbol{j}} \rangle \langle \hat{S}^z_{\boldsymbol{k}} \rangle + \langle \hat{n}^h_{\boldsymbol{i}} \hat{S}^z_{\boldsymbol{k}} \rangle \langle \hat{S}^z_{\boldsymbol{j}} \rangle - 2 \langle \hat{n}^h_{\boldsymbol{i}} \rangle \langle \hat{S}^z_{\boldsymbol{j}} \rangle \langle \hat{S}^z_{\boldsymbol{k}} \rangle. \tag{4.15}$$

We apply these two correlators to our data in Fig. 4.27a. The connected correlator reveals negative correlations in the direct vicinity of the hole with the strongest signal being the bond across the hole with $\boldsymbol{d}^s = (2,0)$. As visible in the bare correlator in the inset, this specific bond also has a negative sign in the bare correlator, where an undoped system should have a positive correlation. This is consistent with a change in parity of the local AFM pattern across the hole, which may be seen as a precursor of true, spin density wave ordering. The negative diagonal correlations around the hole

are due to the fluctuations of the hole along x. We compare these results to DMRG simulations at $\delta = 0.125$, $k_B T/t_x = 0.4$ in Fig. 4.27b. We find qualitatively similar features as in the experimental data. Slight deviations can be attributed to differences in the doping level as well as the precise spin couplings.

While this feature is consistent with what is expected from stripe-ordered systems, similar signals are present in isotropic 2d systems with magnetic polarons. Therefore, this spin signature is only a necessary but not a sufficient condition for spin density wave ordering.

4.5.2 String correlators

To expand the discussion beyond observables used in 2d systems, we introduce the notion of string correlators and 'squeezed space'. Introduced in 1d chains [295], the idea is to correct the spin order for every dopant between the two spins of interest. Due to the presence of spin-charge separation in 1d chains [296], this allows for the observation of hidden AFM ordering [297]. Here, we can use these kinds of correlators in mixD systems to extract the sign change across dopants, similar to the three-point correlations shown above. We therefore define the spin-string correlator in a given

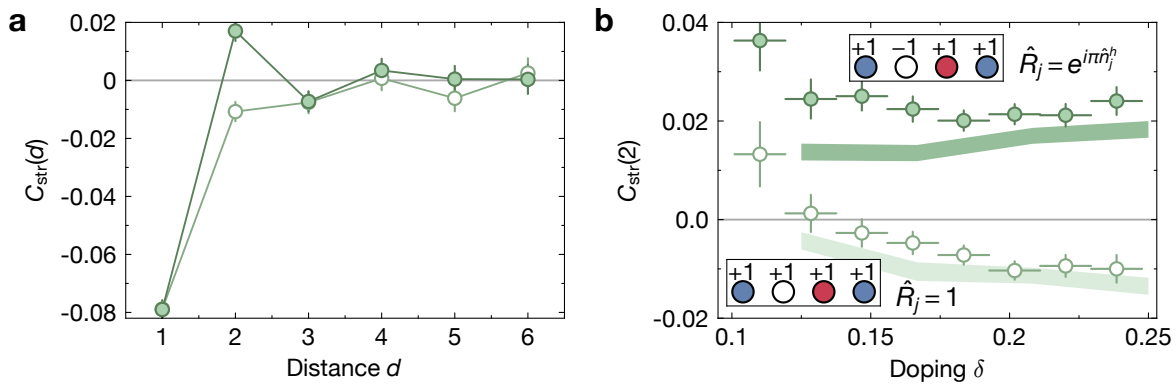

Figure 4.28: String correlator. **a**, Spin-string (dark green) and spin-spin correlator as function of distance d for $\delta = 0.18$. The string correlator recovers the pattern expected from undoped systems for small enough distances. **b**, Both correlators at distance $d = 2$ as a function of doping, showing a change of sign when adding the string between the spins. Shaded regions are theory results for $k_B T/t_x = 0.3$. Error bars are estimated using bootstrapping and are smaller than the marker size if not visible.

chain as

$$C_{\mathrm{str}}(d) = \frac{1}{\mathcal{N}_d} \sum_i \frac{\left\langle \hat{S}^z_i \left(\prod_{j=1}^{d-1} \hat{R}_{i+j} \right) \hat{S}^z_{i+d} \right\rangle - \left\langle \hat{S}^z_i \right\rangle \left\langle \hat{S}^z_{i+d} \right\rangle}{\sigma(\hat{S}^z_i)\sigma(\hat{S}^z_{i+d})}, \tag{4.16}$$

where $\hat{R}_i = e^{i\pi \hat{n}^h_i}$. Note that for $\hat{R}_i = \mathbb{1}$ the common spin-spin correlator of Eq. (3.6) is recovered. This correlator is only well-defined in 1d or 1d-like systems where the string between the two endpoints is uniquely defined. We show the results for both the spin-string and spin-spin correlator as function of distance d at a doping of $\delta = 0.18$ in Fig. 4.28a, where the string correlator recovers the alternating pattern expected from undoped systems. In Fig. 4.28b we study these correlators at distance $d = 2$ as a function of doping. We observe a change in sign when adding the string operators. Furthermore, the signal is mostly independent of doping. This is consistent within the interpretation of dopants forming stripe-like structures that act as domain walls within the local AFM pattern, even without long-range spin ordering. Meanwhile, the normal spin-spin correlator has a significant dependence on doping. We compare this to theory at $k_B T/t_x = 0.3$ and find good agreement with our measurement.

A similar yet slightly different observable is the 'squeezed space' operator. For this operator, all holes are removed from the system in post-analysis. This is very similar to the string correlator introduced above, except that distances are changed as by removing a hole between two spins, a distance of 2 is reduced to a distance of 1. We apply this correlator to our data in Fig. 4.29. We find results very similar to the results obtained by using the string correlator.

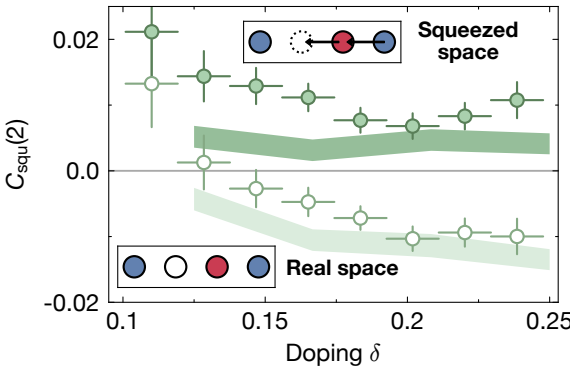

Figure 4.29: Squeezed space analysis. Squeezed space (dark green) and real space spin-spin correlator (light green) at distance $d = 2$ as a function of doping with similar results as for the string correlator shown in Fig. 4.28. Shaded regions are DMRG results ($L_x \times L_y = 8 \times 3$) for $k_B T/t_x = 0.3$. Error bars are estimated using bootstrapping and are smaller than the marker size if not visible.

4.6 Discussion

We have shown experimental results on features of the stripe phase in a mixed-dimensional Fermi-Hubbard system using ultracold atoms in optical lattices. Using multi-point correlation functions, clear indications of extended charge ordering at temperatures around the superexchange energy have been provided. By exploiting our microscopic resolution, we were able to identify stripe-like structures in individual realisations for further evidence of stripe formation. Finally, the spin environment around stripe-like structures is consistent with a change in phase in the local antiferromagnetic pattern across dopants. These prominent features in a system with otherwise only short-ranged correlations may provide new insights into the intertwined relationship between spin and charge ordering in doped antiferromagnets. Meanwhile, the current study does not provide clear evidence of spin stripes or large-scale AFM domain phase changes. Despite mostly being limited to charge order within individual stripes, it already points towards interaction between stripes. So far, these signatures are rather weak and thus require further studies to unravel.

While the current study showed the first signatures of stripe order in a cold atomic system, it holds the potential for a wide range of further, more detailed studies. First and most obviously, realising lower temperatures will significantly improve the currently observed signals as well as uncover new regimes. The longer spin correlation lengths hold the potential to manifest in splitting of peaks at (π, π) in the spin structure factor due to incommensurate magnetism. Similarly, signals in the charge structure factor may appear as multiple stripes forming at specific distances. Past observation of spin stripes, the intriguing question of differences in the transition temperatures of charge and spin stripe ordering will become available. The well-controlled parameter settings of ultracold systems allow for the variation of t/J as well as t_x/t_y to determine more favourable regimes. The aforementioned effect of next-nearest-neighbour hopping also lends itself to further studies. Furthermore, the investigation of the breakdown of stripe order due to diagonal tunnel couplings provides an interesting challenge, as these couplings are more difficult to realise in optical lattices. Lastly, the numerically unresolved issue of the precise periodicity of stripes is a compelling open question for cold atomic systems. Despite current temperature mostly limiting these studies to mixed-dimensional systems, the energy scales of dopant pairing in normal 2d systems may also already be within reach [287].

Mixed-dimensional systems may also provide further insights into related phases of matter. It has been shown that via the mapping from the repulsive to the attractive side of the Fermi-Hubbard model [127], the stripe phase relates to the Fulde-Ferrell-Larkin-Ovchinnikov state [298, 299] in attractive, undoped, spin-polarised systems [300]. Finally, the connection to the recently discovered nickelate family of super-

conductors is highly striking. Their mixed-dimensional, bilayer structure is in direct correspondence to the capabilities of our unique experimental platform, promising the possibility to study this new class of materials from a complementary point of view.

Chapter 5

Conclusion

In this thesis, new achievements on improvements in the microscopic understanding of the Fermi-Hubbard model using a quantum gas microscope have been presented. The first observation of stripes in a cold atomic system was shown by increasing energy scales in a mixed-dimensional approach. As a complementary study to solid-state measurements, we were able to focus on multi-point correlations, pointing towards favourable conditions for stripe formations. Signatures in both spin and charge sector reveal the presence of stripes at temperatures around the superexchange coupling. This measurement was enabled by the technical advancements achieved in this thesis. Implementing a bichromatic superlattice with superior phase stability opens up access to new parameter regimes for quantum simulation. Adding additional on-site detunings can remove unwanted tunnel couplings as well as change the magnitude and sign of spin-exchange couplings. Furthermore, it presents a alternative approach for quantum computation using neutral atoms by preparing isolated double-wells.

From this starting point, future endeavours in quantum simulation promise possible improvements in temperature. With the exceptional phase stability achieved here, we have laid the technical groundwork for the implementation of cooling methods for the high-fidelity preparation of low-entropy quantum systems [198, 250, 251]. These may now be implemented without any required additional changes to the experimental setup. Lowering the temperature even further – compared to the already state-of-the-art values of $0.25\,t$ – pushes the frontier of quantum simulation of the Fermi-Hubbard model, where a multitude of incompletely understood phases await further investigation. Already at the present temperatures, pseudogap phenomena may be revealed [66, 111, 301], while theoretical calculations also predict direct pairing of holes [287]. Modest improvements in temperature below $0.1\,t$ may then unveil stripe order in pure 2d systems without modified couplings, and thus adding complementary information to the discussion on the relationship between superconductivity and stripe phases in the Fermi-Hubbard model.

On the other hand, the promising results for single-qubit gates obtained in the course of characterising the superlattice are essential building blocks for future stud-

ies on quantum computation. Despite no significant gate optimisation, the obtained error rates have been encouraging. With the implementation of optimised control theory [302] for the precise gate sequence, the so-far comparably slow speed may be vastly improved [303]. Simple proposals for multi-qubit gates are also within reach of this experiment, where the actual gate fidelities remain to be investigated. Finally, future experiments may combine the advantages of collisional gates [227] with the connectivity obtained in optical tweezer arrays to realise functional fermionic processors [228, 231].

Bibliography

[1] I. L. Chuang and M. A. Nielsen. *Quantum Computation and Quantum Information: 10th Anniversary Edition*. Cambridge University Press (2010). (Cited on page **1**)

[2] P. W. Shor. *Algorithms for quantum computation: discrete logarithms and factoring*. Proceedings 35th Annual Symposium on Foundations of Computer Science pages 124–134 (1994). (Cited on page **1**)

[3] L. K. Grover. *A fast quantum mechanical algorithm for database search*. Proceedings of the Twenty-Eighth Annual ACM Symposium on Theory of Computing pages 212–219 (1996). (Cited on page **1**)

[4] S. Lloyd. *Universal Quantum Simulators*. Science **273**, 1073–1078 (1996). (Cited on page **1**)

[5] J. Bermejo-Vega, D. Hangleiter, M. Schwarz, R. Raussendorf, and J. Eisert. *Architectures for Quantum Simulation Showing a Quantum Speedup*. Phys. Rev. X **8**, 021010 (2018). (Cited on page **1**)

[6] J. Liu, M. Liu, J.-P. Liu, Z. Ye, Y. Wang, Y. Alexeev, J. Eisert, and L. Jiang. *Towards provably efficient quantum algorithms for large-scale machine-learning models*. Nat. Commun. **15**, 434 (2024). (Cited on page **1**)

[7] D. P. DiVincenzo. *The Physical Implementation of Quantum Computation*. Fortschr. Phys. **48**, 771–783 (2000). (Cited on page **1**)

[8] J. I. Cirac and P. Zoller. *A scalable quantum computer with ions in an array of microtraps*. Nature **404**, 579–581 (2000). (Cited on page **1**)

[9] J. P. Gaebler, T. R. Tan, Y. Lin, Y. Wan, R. Bowler, A. C. Keith, S. Glancy, K. Coakley, E. Knill, D. Leibfried, and D. J. Wineland. *High-Fidelity Universal Gate Set for* $^{9}\mathrm{Be}^{+}$ *Ion Qubits*. Phys. Rev. Lett. **117**, 060505 (2016). (Cited on page **1**)

[10] C. J. Ballance, T. P. Harty, N. M. Linke, M. A. Sepiol, and D. M. Lucas. *High-Fidelity Quantum Logic Gates Using Trapped-Ion Hyperfine Qubits*. Phys. Rev. Lett. **117**, 060504 (2016). (Cited on page **1**)

[11] J. Clarke and F. K. Wilhelm. *Superconducting quantum bits*. Nature **453**, 1031–1042

(2008). (Cited on page 1)

[12] Y. Nakamura, Y. A. Pashkin, and J. S. Tsai. *Coherent control of macroscopic quantum states in a single-Cooper-pair box*. Nature **398**, 786–788 (1999). (Cited on page 1)

[13] J. E. Mooij, T. P. Orlando, L. Levitov, L. Tian, C. H. van der Wal, and S. Lloyd. *Josephson Persistent-Current Qubit*. Science **285**, 1036–1039 (1999). (Cited on page 1)

[14] J. M. Martinis. *Superconducting phase qubits*. Quantum Inf. Process. **8**, 81–103 (2009). (Cited on page 1)

[15] D. Loss and D. P. DiVincenzo. *Quantum computation with quantum dots*. Phys. Rev. A **57**, 120–126 (1998). (Cited on page 1)

[16] A. Imamoglu, D. D. Awschalom, G. Burkard, D. P. DiVincenzo, D. Loss, M. Sherwin, and A. Small. *Quantum Information Processing Using Quantum Dot Spins and Cavity QED*. Phys. Rev. Lett. **83**, 4204–4207 (1999). (Cited on page 1)

[17] B. Trauzettel, D. V. Bulaev, D. Loss, and G. Burkard. *Spin qubits in graphene quantum dots*. Nat. Phys. **3**, 192–196 (2007). (Cited on page 1)

[18] J. R. Petta, A. C. Johnson, J. M. Taylor, E. A. Laird, A. Yacoby, M. D. Lukin, C. M. Marcus, M. P. Hanson, and A. C. Gossard. *Coherent Manipulation of Coupled Electron Spins in Semiconductor Quantum Dots*. Science **309**, 2180–2184 (2005). (Cited on page 1)

[19] E. Knill, R. Laflamme, and G. J. Milburn. *A scheme for efficient quantum computation with linear optics*. Nature **409**, 46–52 (2001). (Cited on page 1)

[20] S. Aaronson and A. Arkhipov. *The Computational Complexity of Linear Optics*. Theory of Computing **9**, 143–252 (2013). (Cited on page 1)

[21] H.-S. Zhong, H. Wang, Y.-H. Deng, M.-C. Chen, L.-C. Peng, Y.-H. Luo, J. Qin, D. Wu, X. Ding, Y. Hu, P. Hu, X.-Y. Yang, W.-J. Zhang, H. Li, Y. Li, X. Jiang, L. Gan, G. Yang, L. You, Z. Wang, L. Li, N.-L. Liu, C.-Y. Lu, and J.-W. Pan. *Quantum computational advantage using photons*. Science **370**, 1460–1463 (2020). (Cited on page 1)

[22] M. V. G. Dutt, L. Childress, L. Jiang, E. Togan, J. Maze, F. Jelezko, A. S. Zibrov, P. R. Hemmer, and M. D. Lukin. *Quantum Register Based on Individual Electronic and Nuclear Spin Qubits in Diamond*. Science **316**, 1312–1316 (2007). (Cited on page 1)

[23] S. Boixo, S. V. Isakov, V. N. Smelyanskiy, R. Babbush, N. Ding, Z. Jiang, M. J. Bremner, J. M. Martinis, and H. Neven. *Characterizing quantum supremacy in near-term devices*. Nat. Phys. **14**, 595–600 (2018). (Cited on page **1**)

[24] F. Arute, K. Arya, R. Babbush, D. Bacon, J. C. Bardin, R. Barends, R. Biswas, S. Boixo, F. G. S. L. Brandao, D. A. Buell, B. Burkett, Y. Chen, Z. Chen, B. Chiaro, R. Collins, W. Courtney, A. Dunsworth, E. Farhi, B. Foxen, A. Fowler, C. Gidney, M. Giustina, R. Graff, K. Guerin, S. Habegger, M. P. Harrigan, M. J. Hartmann, A. Ho, M. Hoffmann, T. Huang, T. S. Humble, S. V. Isakov, E. Jeffrey, Z. Jiang, D. Kafri, K. Kechedzhi, J. Kelly, P. V. Klimov, S. Knysh, A. Korotkov, F. Kostritsa, D. Landhuis, M. Lindmark, E. Lucero, D. Lyakh, S. Mandrà, J. R. McClean, M. McEwen, A. Megrant, X. Mi, K. Michielsen, M. Mohseni, J. Mutus, O. Naaman, M. Neeley, C. Neill, M. Y. Niu, E. Ostby, A. Petukhov, J. C. Platt, C. Quintana, E. G. Rieffel, P. Roushan, N. C. Rubin, D. Sank, K. J. Satzinger, V. Smelyanskiy, K. J. Sung, M. D. Trevithick, A. Vainsencher, B. Villalonga, T. White, Z. J. Yao, P. Yeh, A. Zalcman, H. Neven, and J. M. Martinis. *Quantum supremacy using a programmable superconducting processor*. Nature **574**, 505–510 (2019). (Cited on page **1**)

[25] D. Bluvstein, S. J. Evered, A. A. Geim, S. H. Li, H. Zhou, T. Manovitz, S. Ebadi, M. Cain, M. Kalinowski, D. Hangleiter, J. P. B. Ataides, N. Maskara, I. Cong, X. Gao, P. S. Rodriguez, T. Karolyshyn, G. Semeghini, M. J. Gullans, M. Greiner, V. Vuletić, and M. D. Lukin. *Logical quantum processor based on reconfigurable atom arrays*. Nature **626**, 58–65 (2024). (Cited on pages **1** and **63**)

[26] J. Preskill. *Quantum Computing in the NISQ era and beyond*. Quantum **2**, 79 (2018). (Cited on page **1**)

[27] M. Brooks. *Quantum computers: what are they good for?* Nature **617**, S1–S3 (2023). (Cited on page **1**)

[28] E. Dagotto. *Complexity in Strongly Correlated Electronic Systems*. Science **309**, 257–262 (2005). (Cited on page **1**)

[29] E. Y. Loh, J. E. Gubernatis, R. T. Scalettar, S. R. White, D. J. Scalapino, and R. L. Sugar. *Sign problem in the numerical simulation of many-electron systems*. Phys. Rev. B **41**, 9301–9307 (1990). (Cited on page **1**)

[30] J. M. Tranquada. *Spins, stripes, and superconductivity in hole-doped cuprates*. AIP Conf. **1550**, 114–187 (2013). (Cited on pages **1**, **2**, **7**, and **73**)

[31] I. Bloch, J. Dalibard, and S. Nascimbène. *Quantum simulations with ultracold quantum gases*. Nat. Phys. **8**, 267–276 (2012). (Cited on page **1**)

[32] T. H. Johnson, S. R. Clark, and D. Jaksch. *What is a quantum simulator?* EPJ Quantum Technol. **1**, 10 (2014). (Cited on page **1**)

[33] R. P. Feynman. *Simulating physics with computers*. Int. J. Theor. Phys. **21**, 467–488 (1982). (Cited on page **1**)

[34] A. J. Daley, I. Bloch, C. Kokail, S. Flannigan, N. Pearson, M. Troyer, and P. Zoller. *Practical quantum advantage in quantum simulation*. Nature **607**, 667–676 (2022). (Cited on page **1**)

[35] T. Hänsch and A. Schawlow. *Cooling of gases by laser radiation*. Opt. Commun. **13**, 68–69 (1975). (Cited on page **1**)

[36] A. Ashkin. *Trapping of Atoms by Resonance Radiation Pressure*. Phys. Rev. Lett. **40**, 729–732 (1978). (Cited on page **1**)

[37] D. J. Wineland, R. E. Drullinger, and F. L. Walls. *Radiation-Pressure Cooling of Bound Resonant Absorbers*. Phys. Rev. Lett. **40**, 1639–1642 (1978). (Cited on page **1**)

[38] W. D. Phillips and H. Metcalf. *Laser Deceleration of an Atomic Beam*. Phys. Rev. Lett. **48**, 596–599 (1982). (Cited on page **1**)

[39] M. H. Anderson, J. R. Ensher, M. R. Matthews, C. E. Wieman, and E. A. Cornell. *Observation of Bose-Einstein Condensation in a Dilute Atomic Vapor*. Science **269**, 198–201 (1995). (Cited on page **1**)

[40] K. B. Davis, M. O. Mewes, M. R. Andrews, N. J. van Druten, D. S. Durfee, D. M. Kurn, and W. Ketterle. *Bose-Einstein Condensation in a Gas of Sodium Atoms*. Phys. Rev. Lett. **75**, 3969–3973 (1995). (Cited on page **1**)

[41] C. C. Bradley, C. A. Sackett, J. J. Tollett, and R. G. Hulet. *Evidence of Bose-Einstein Condensation in an Atomic Gas with Attractive Interactions*. Phys. Rev. Lett. **75**, 1687–1690 (1995). (Cited on page **1**)

[42] B. DeMarco and D. S. Jin. *Onset of Fermi Degeneracy in a Trapped Atomic Gas*. Science **285**, 1703–1706 (1999). (Cited on page **1**)

[43] W. Ketterle and N. J. V. Druten. *Evaporative Cooling of Trapped Atoms*. Adv. At. Mol. Opt. Phy. **37**, 181–236 (1996). (Cited on page **1**)

[44] A. J. Kerman, V. Vuletić, C. Chin, and S. Chu. *Beyond Optical Molasses: 3D Raman Sideband Cooling of Atomic Cesium to High Phase-Space Density*. Phys. Rev. Lett. **84**, 439–442 (2000). (Cited on page **1**)

[45] V. S. Letokhov. *Narrowing of the Doppler Width in a Standing Wave*. Pis'ma Zh. Eksp. Teor. Fiz **7**, 348 (1968). (Cited on page **1**)

[46] C. Salomon, J. Dalibard, A. Aspect, H. Metcalf, and C. Cohen-Tannoudji. *Channeling atoms in a laser standing wave*. Phys. Rev. Lett. **59**, 1659–1662 (1987). (Cited on page **1**)

[47] M. Lewenstein, A. Sanpera, V. Ahufinger, B. Damski, A. Sen(De), and U. Sen. *Ultracold atomic gases in optical lattices: mimicking condensed matter physics and beyond*. Adv. Phys. **56**, 243–379 (2007). (Cited on pages **1** and **7**)

[48] M. Greiner, O. Mandel, T. Esslinger, T. W. Hänsch, and I. Bloch. *Quantum phase transition from a superfluid to a Mott insulator in a gas of ultracold atoms*. Nature **415**, 39–44 (2002). (Cited on page **2**)

[49] R. Jördens, N. Strohmaier, K. Günter, H. Moritz, and T. Esslinger. *A Mott insulator of fermionic atoms in an optical lattice*. Nature **455**, 204–207 (2008). (Cited on page **2**)

[50] U. Schneider, L. Hackermüller, S. Will, T. Best, I. Bloch, T. A. Costi, R. W. Helmes, D. Rasch, and A. Rosch. *Metallic and Insulating Phases of Repulsively Interacting Fermions in a 3D Optical Lattice*. Science **322**, 1520–1525 (2008). (Cited on page **2**)

[51] D. Greif, T. Uehlinger, G. Jotzu, L. Tarruell, and T. Esslinger. *Short-Range Quantum Magnetism of Ultracold Fermions in an Optical Lattice*. Science **340**, 1307–1310 (2013). (Cited on pages **2** and **32**)

[52] N. Goldman, G. Juzeliunas, P. Öhberg, and I. B. Spielman. *Light-induced gauge fields for ultracold atoms*. Rep. Prog. Phys. **77**, 126401 (2014). (Cited on page **2**)

[53] M. Aidelsburger, M. Atala, S. Nascimbène, S. Trotzky, Y.-A. Chen, and I. Bloch. *Experimental Realization of Strong Effective Magnetic Fields in an Optical Lattice*. Phys. Rev. Lett. **107**, 255301 (2011). (Cited on pages **2** and **7**)

[54] M. Srednicki. *Chaos and quantum thermalization*. Phys. Rev. E **50**, 888–901 (1994). (Cited on page **2**)

[55] A. M. Kaufman, M. E. Tai, A. Lukin, M. Rispoli, R. Schittko, P. M. Preiss, and M. Greiner. *Quantum thermalization through entanglement in an isolated many-body system*. Science **353**, 794–800 (2016). (Cited on page **2**)

[56] W. S. Bakr, I. Gillen, Jonathon, A. Peng, S. Fölling, and M. Greiner. *A quantum gas microscope for detecting single atoms in a Hubbard-regime optical lattice*. Nature **462**, 74–77 (2009). (Cited on pages **2** and **8**)

[57] W. S. Bakr, A. Peng, M. E. Tai, R. Ma, J. Simon, J. I. Gillen, S. Fölling, L. Pollet, and M. Greiner. *Probing the Superfluid-to-Mott Insulator Transition at the Single-Atom Level*. Science **329**, 547–550 (2010). (Cited on pages **2** and **22**)

[58] M. Endres, M. Cheneau, T. Fukuhara, C. Weitenberg, P. Schauß, C. Gross, L. Mazza, M. C. Bañuls, L. Pollet, I. Bloch, and S. Kuhr. *Observation of Correlated Particle-Hole Pairs and String Order in Low-Dimensional Mott Insulators*. Science **334**, 200–203 (2011). (Cited on page **2**)

[59] D. Wei, D. Adler, K. Srakaew, S. Agrawal, P. Weckesser, I. Bloch, and J. Zeiher. *Observation of Brane Parity Order in Programmable Optical Lattices*. Phys. Rev. X **13**, 021042 (2023). (Cited on pages **2**, **7**, and **30**)

[60] A. Omran, M. Boll, T. A. Hilker, K. Kleinlein, G. Salomon, I. Bloch, and C. Gross. *Microscopic Observation of Pauli Blocking in Degenerate Fermionic Lattice Gases*. Phys. Rev. Lett. **115**, 263001 (2015). (Cited on pages **2**, **8**, **21**, and **25**)

[61] E. Haller, J. Hudson, A. Kelly, D. A. Cotta, B. Peaudecerf, G. D. Bruce, and S. Kuhr. *Single-atom imaging of fermions in a quantum-gas microscope*. Nat. Phys. **11**, 738–742 (2015). (Cited on pages **2** and **8**)

[62] M. F. Parsons, F. Huber, A. Mazurenko, C. S. Chiu, W. Setiawan, K. Wooley-Brown, S. Blatt, and M. Greiner. *Site-Resolved Imaging of Fermionic* ^{6}Li *in an Optical Lattice*. Phys. Rev. Lett. **114**, 213002 (2015). (Cited on pages **2** and **8**)

[63] L. W. Cheuk, M. A. Nichols, M. Okan, T. Gersdorf, V. V. Ramasesh, W. S. Bakr, T. Lompe, and M. W. Zwierlein. *Quantum-Gas Microscope for Fermionic Atoms*. Phys. Rev. Lett. **114**, 193001 (2015). (Cited on pages **2** and **8**)

[64] A. Mazurenko, C. Chiu, G. Ji, M. F. Parsons, M. Kanász-Nagy, R. Schmidt, F. Grusdt, E. Demler, D. Greif, and M. Greiner. *A cold-atom Fermi-Hubbard antiferromagnet*. Nature **545**, 462–466 (2017). (Cited on pages **2**, **20**, **48**, and **79**)

[65] M. Boll, T. A. Hilker, G. Salomon, A. Omran, J. Nespolo, L. Pollet, I. Bloch, and C. Gross. *Spin- and density-resolved microscopy of antiferromagnetic correlations in Fermi-Hubbard chains*. Science **353**, 1257–1260 (2016). (Cited on pages **2**, **8**, **22**, **25**, and **32**)

[66] J. Koepsell, D. Bourgund, P. Sompet, S. Hirthe, A. Bohrdt, Y. Wang, F. Grusdt, E. Demler, G. Salomon, C. Gross, and I. Bloch. *Microscopic evolution of doped Mott insulators from polaronic metal to Fermi liquid*. Science **374**, 82–86 (2021). (Cited on pages **2**, **8**, **25**, **78**, and **107**)

[67] P. T. Brown, E. Guardado-Sanchez, B. M. Spar, E. W. Huang, T. P. Devereaux, and

W. S. Bakr. *Angle-resolved photoemission spectroscopy of a Fermi-Hubbard system*. Nat. Phys. **16**, 16–31 (2020). (Cited on page **2**)

[68] P. T. Brown, D. Mitra, E. Guardado-Sanchez, P. Schauß, S. S. Kondov, E. Khatami, T. Paiva, N. Trivedi, D. A. Huse, and W. S. Bakr. *Spin-imbalance in a 2D Fermi-Hubbard system*. Science **357**, 1385–1388 (2017). (Cited on pages **2** and **8**)

[69] M. A. Nichols, L. W. Cheuk, M. Okan, T. R. Hartke, E. Mendez, T. Senthil, E. Khatami, H. Zhang, and M. W. Zwierlein. *Spin transport in a Mott insulator of ultracold fermions*. Science **363**, 383–387 (2019). (Cited on page **2**)

[70] T. Hartke, B. Oreg, N. Jia, and M. Zwierlein. *Quantum register of fermion pairs*. Nature **601**, 537–541 (2022). (Cited on page **2**)

[71] S. Hirthe, T. Chalopin, D. Bourgund, P. Bojović, A. Bohrdt, E. Demler, F. Grusdt, I. Bloch, and T. A. Hilker. *Magnetically mediated hole pairing in fermionic ladders of ultracold atoms*. Nature **613**, 463–467 (2023). (Cited on pages **2**, **81**, and **82**)

[72] T. Hartke, B. Oreg, C. Turnbaugh, N. Jia, and M. Zwierlein. *Direct observation of nonlocal fermion pairing in an attractive Fermi-Hubbard gas*. Science **381**, 82–86 (2023). (Cited on pages **2** and **78**)

[73] J. Bednorz and K. Müller. *Possible high-Tc superconductivity in the Ba-La-Cu-O system*. Z. Physik. B **64**, 189 (1986). (Cited on pages **2** and **69**)

[74] S. A. Kivelson, I. P. Bindloss, E. Fradkin, V. Oganesyan, J. M. Tranquada, A. Kapitulnik, and C. Howald. *How to detect fluctuating stripes in the high-temperature superconductors*. Rev. Mod. Phys. **75**, 1201–1241 (2003). (Cited on pages **2**, **71**, and **73**)

[75] D. S. Marshall, D. S. Dessau, A. G. Loeser, C.-H. Park, A. Y. Matsuura, J. N. Eckstein, I. Bozovic, P. Fournier, A. Kapitulnik, W. E. Spicer, and Z.-X. Shen. *Unconventional Electronic Structure Evolution with Hole Doping in* $Bi_2Sr_2CaCu_2O_{8+\delta}$*: Angle-Resolved Photoemission Results*. Phys. Rev. Lett. **76**, 4841–4844 (1996). (Cited on page **2**)

[76] R. Preuss, W. Hanke, C. Gröber, and H. G. Evertz. *Pseudogaps and Their Interplay with Magnetic Excitations in the Doped 2D Hubbard Model*. Phys. Rev. Lett. **79**, 1122–1125 (1997). (Cited on page **2**)

[77] D. J. Scalapino. *A common thread: The pairing interaction for unconventional superconductors*. Rev. Mod. Phys. **84**, 1383–1417 (2012). (Cited on page **2**)

[78] P. A. Lee, N. Nagaosa, and X.-G. Wen. *Doping a Mott insulator: Physics of high-temperature superconductivity*. Rev. Mod. Phys. **78**, 17–85 (2006). (Cited on pages **2** and **73**)

[79] C. M. Varma. *Colloquium: Linear in temperature resistivity and associated mysteries including high temperature superconductivity*. Rev. Mod. Phys. **92**, 031001 (2020). (Cited on page **2**)

[80] J. Hubbard. *Electron Correlations in Narrow Energy Bands*. Proc. R. Soc. **276**, 238–257 (1963). (Cited on pages **2**, **9**, and **69**)

[81] M. Qin, C.-M. Chung, H. Shi, E. Vitali, C. Hubig, U. Schollwöck, S. R. White, and S. Zhang. *Absence of Superconductivity in the Pure Two-Dimensional Hubbard Model*. Phys. Rev. X **10**, 031016 (2020). (Cited on pages **2**, **71**, **75**, and **77**)

[82] J. D. Axe and M. K. Crawford. *Structural Instabilities in Lanthanum Cuprate Superconductors*. J. Low. Temp. Phys. **95**, 271–284 (1995). (Cited on pages **2** and **71**)

[83] J. M. Tranquada, B. J. Sternlieb, J. D. Axe, Y. Nakamura, and S. Uchida. *Evidence for stripe correlations of spins and holes in copper oxide superconductors*. Nature **375**, 561–563 (1995). (Cited on pages **2**, **71**, **74**, **76**, **77**, and **89**)

[84] S. R. White and D. J. Scalapino. *Competition between stripes and pairing in a $t - t' - J$ model*. Phys. Rev. B **60**, R753–R756 (1999). (Cited on pages **2** and **76**)

[85] E. W. Huang, C. B. Mendl, H.-C. Jian, B. Moritz, and T. Deveraux. *Stripe order from the perspective of the Hubbard model*. npj Quant. Mater. **3**, 22 (2018). (Cited on pages **2**, **71**, **76**, and **77**)

[86] H.-C. Jiang and T. P. Devereaux. *Superconductivity in the doped Hubbard model and its interplay with next-nearest hopping t'*. Science **365**, 1424–1428 (2019). (Cited on page **2**)

[87] B.-X. Zheng, C.-M. Chung, P. Corboz, G. Ehlers, M.-P. Qin, R. M. Noack, H. Shi, S. R. White, S. Zhang, and G. K.-L. Chan. *Stripe order in the underdoped region of the two-dimensional Hubbard model*. Science **358**, 1155–1160 (2017). (Cited on pages **2**, **71**, **72**, **75**, and **76**)

[88] I. Bloch, J. Dalibard, and W. Zwerger. *Many-body physics with ultracold gases*. Rev. Mod. Phys. **80**, 885–964 (2008). (Cited on pages **7** and **14**)

[89] T. Esslinger. *Fermi-Hubbard Physics with Atoms in an Optical Lattice*. Annu. Rev. Condens. Matter Phys. **1**, 129–152 (2010). (Cited on pages **7** and **12**)

[90] C. Gross and I. Bloch. *Quantum simulations with ultracold atoms in optical lattices*. Science **357**, 995–1001 (2017). (Cited on page 7)

[91] L. Tarruell and L. Sanchez-Palencia. *Quantum simulation of the Hubbard model with ultracold fermions in optical lattices*. C. R. Phys. **19**, 365 (2018). (Cited on pages 7, 11, 12, and 70)

[92] D. M. Ginsberg. *Physical Properties of High Temperature Superconductors I*. World Scientific (1998). (Cited on page 7)

[93] R. Grimm, M. Weidemüller, and Y. B. Ovchinnikov. *Optical Dipole Traps for Neutral Atoms*. Adv. At. Mol. Opt. Phys. **42**, 95–170 (2000). (Cited on pages 7 and 12)

[94] C. Kittel. *Introduction to Solid State Physics*. Wiley (2004). (Cited on page 7)

[95] R. Staudt, M. Dzierzawa, and A. Muramatsu. *Phase diagram of the three-dimensional Hubbard model at half filling*. Eur. Phys. J. B **17**, 411–415 (2000). (Cited on page 7)

[96] L. Tarruell, D. Greif, T. Uehlinger, G. Jotzu, and T. Esslinger. *Creating, moving and merging Dirac points with a Fermi gas in a tunable honeycomb lattice*. Nature **483**, 302–305 (2012). (Cited on page 7)

[97] C. Becker, P. Soltan-Panahi, J. Kronjäger, S. Dörscher, K. Bongs, and K. Sengstock. *Ultracold quantum gases in triangular optical lattices*. New J. Phys. **12**, 065025 (2010). (Cited on pages 7 and 29)

[98] J. Yang, L. Liu, J. Mongkolkiattichai, and P. Schauss. *Site-Resolved Imaging of Ultracold Fermions in a Triangular-Lattice Quantum Gas Microscope*. PRX Quantum **2**, 020344 (2021). (Cited on pages 7 and 8)

[99] C. Gross and W. S. Bakr. *Quantum gas microscopy for single atom and spin detection*. Nat. Phys. **17**, 1316–1323 (2021). (Cited on page 8)

[100] J. F. Sherson, C. Weitenberg, M. Endres, M. Cheneau, I. Bloch, and S. Kuhr. *Single-atom-resolved fluorescence imaging of an atomic Mott insulator*. Nature **467**, 68–72 (2010). (Cited on page 8)

[101] J. Koepsell, S. Hirthe, D. Bourgund, P. Sompet, J. Vijayan, G. Salomon, C. Gross, and I. Bloch. *Robust Bilayer Charge Pumping for Spin- and Density-Resolved Quantum Gas Microscopy*. Phys. Rev. Lett. **125**, 010403 (2020). (Cited on pages 8, 19, 22, 24, 25, 29, and 34)

[102] T. Hartke, B. Oreg, N. Jia, and M. Zwierlein. *Doublon-Hole Correlations and Fluc-*

tuation Thermometry in a Fermi-Hubbard Gas. Phys. Rev. Lett. **125**, 113601 (2020). (Cited on page **8**)

[103] M. F. Parsons, A. Mazurenko, C. Chiu, G. Ji, D. Greif, and M. Greiner. *Site-resolved measurement of the spin-correlation function in the Fermi-Hubbard model*. Science **353**, 1253–1256 (2016). (Cited on pages **8** and **22**)

[104] L. W. Cheuk, M. A. Nichols, L. K. R., O. Melih, H. Zhang, E. Khatami, T. Nandini, T. Paiva, M. Rigol, and M. Zwierlein. *Observation of spatial charge and spin correlations in the 2D Fermi-Hubbard model*. Science **353**, 1260–1264 (2016). (Cited on page **8**)

[105] Z. Z. Yan, B. M. Spar, M. L. Prichard, S. Chi, H.-T. Wei, E. Ibarra-García-Padilla, K. R. A. Hazzard, and W. S. Bakr. *Two-Dimensional Programmable Tweezer Arrays of Fermions*. Phys. Rev. Lett. **129**, 123201 (2022). (Cited on pages **8**, **22**, and **63**)

[106] J. Koepsell, J. Vijayan, P. Sompet, F. Grusdt, T. A. Hilker, E. Demler, G. Salomon, I. Bloch, and C. Gross. *Imaging magnetic polarons in the doped Fermi-Hubbard model*. Nature **572**, 358–362 (2019). (Cited on pages **8**, **25**, **32**, **73**, and **78**)

[107] A. Bohrdt, Y. Wang, J. Koepsell, M. Kánasz-Nagy, E. Demler, and F. Grusdt. *Dominant Fifth-Order Correlations in Doped Quantum Antiferromagnets*. Phys. Rev. Lett. **126**, 026401 (2021). (Cited on page **8**)

[108] C. Miles, A. Bohrdt, R. Wu, C. Chiu, M. Xu, G. Ji, M. Greiner, K. Q. Weinberger, E. Demler, and E.-A. Kim. *Correlator convolutional neural networks as an interpretable architecture for image-like quantum matter data*. Nat. Commun. **12**, 3905 (2021). (Cited on page **8**)

[109] M. L. Prichard, B. M. Spar, I. Morera, E. Demler, Z. Z. Yan, and W. S. Bakr. *Directly imaging spin polarons in a kinetically frustrated Hubbard system*. Nature **629**, 323–328 (2024). (Cited on pages **8** and **30**)

[110] M. Lebrat, M. Xu, L. H. Kendrick, A. Kale, Y. Gang, P. Seetharaman, I. Morera, E. Khatami, E. Demler, and M. Greiner. *Observation of Nagaoka Polarons in a Fermi-Hubbard Quantum Simulator*. Nature **629**, 317–322 (2024). (Cited on page **8**)

[111] T. Chalopin and et al. In preparation (2024). (Cited on pages **8**, **78**, **79**, and **107**)

[112] G. A. Phelps, A. Hébert, A. Krahn, S. Dickerson, F. Öztürk, S. Ebadi, L. Su, and M. Greiner. *Sub-second production of a quantum degenerate gas*. arXiv.2007.10807 (2020). (Cited on page **8**)

[113] L. Su, A. Douglas, M. Szurek, R. Groth, S. F. Ozturk, A. Krahn, A. H. Hébert,

G. A. Phelps, S. Ebadi, S. Dickerson, F. Ferlaino, O. Marković, and M. Greiner. *Dipolar quantum solids emerging in a Hubbard quantum simulator*. Nature **622**, 724–729 (2023). (Cited on pages **8** and **30**)

[114] M. Miranda, R. Inoue, Y. Okuyama, A. Nakamoto, and M. Kozuma. *Site-resolved imaging of ytterbium atoms in a two-dimensional optical lattice*. Phys. Rev. A **91**, 063414 (2015). (Cited on page **8**)

[115] R. Yamamoto, J. Kobayashi, T. Kuno, K. Kato, and Y. Takahashi. *An ytterbium quantum gas microscope with narrow-line laser cooling*. New J. Phys. **18**, 023016 (2016). (Cited on page **8**)

[116] A. Alberti, C. Robens, W. Alt, S. Brakhane, M. Karski, R. Reimann, A. Widera, and D. Meschede. *Super-resolution microscopy of single atoms in optical lattices*. New J. Phys. **18**, 053010 (2016). (Cited on page **8**)

[117] K. Kwon, K. Kim, J. Hur, S. Huh, and J.-y. Choi. *Site-resolved imaging of a bosonic Mott insulator of* ^{7}Li *atoms*. Phys. Rev. A **105**, 033323 (2022). (Cited on page **8**)

[118] A. W. Young, W. J. Eckner, N. Schine, A. M. Childs, and A. M. Kaufman. *Tweezer-programmable 2D quantum walks in a Hubbard-regime lattice*. Science **377**, 885–889 (2022). (Cited on page **8**)

[119] W.-Y. Zhang, M.-G. He, H. Sun, Y.-G. Zheng, Y. Liu, A. Luo, H.-Y. Wang, Z.-H. Zhu, P.-Y. Qiu, Y.-C. Shen, X.-K. Wang, W. Lin, S.-T. Yu, B.-C. Li, B. Xiao, M.-D. Li, Y.-M. Yang, X. Jiang, H.-N. Dai, Y. Zhou, X. Ma, Z.-S. Yuan, and J.-W. Pan. *Scalable Multipartite Entanglement Created by Spin Exchange in an Optical Lattice*. Phys. Rev. Lett. **131**, 073401 (2023). (Cited on pages **8** and **63**)

[120] S. Buob, J. Höschele, V. Makhalov, A. Rubio-Abadal, and L. Tarruell. *A Strontium Quantum-Gas Microscope*. PRX Quantum **5**, 020316 (2024). (Cited on page **8**)

[121] A. Impertro, J. Wienand, S. Häfele, H. von Raven, S. Hubele, T. Klostermann, C. R. Cabrera, I. Bloch, and M. Aidelsburger. *An unsupervised deep learning algorithm for single-site reconstruction in quantum gas microscopes*. Commun. Phys. **6** (2023). (Cited on pages **8** and **32**)

[122] G. J. A. Edge, R. Anderson, D. Jervis, D. C. McKay, R. Day, S. Trotzky, and J. H. Thywissen. *Imaging and addressing of individual fermionic atoms in an optical lattice*. Phys. Rev. A **92**, 063406 (2015). (Cited on page **8**)

[123] M. C. Gutzwiller. *Effect of Correlation on the Ferromagnetism of Transition Metals*. Phys. Rev. Lett. **10**, 159–162 (1963). (Cited on page **9**)

[124] J. Kanamori. *Electron Correlation and Ferromagnetism of Transition Metals*. Prog. Theor. Phys. **30**, 275–289 (1963). (Cited on page **9**)

[125] J. M. Tranquada. *Cuprate superconductors as viewed through a striped lens*. Adv. in Phys. **69**, 437–509 (2020). (Cited on pages **10**, **72**, **76**, and **77**)

[126] V. J. Emery. *Theory of the quasi-one-dimensional electron gas with strong "on-site" interactions*. Phys. Rev. B **14**, 2989–2994 (1976). (Cited on page **10**)

[127] A. F. Ho, M. A. Cazalilla, and T. Giamarchi. *Quantum simulation of the Hubbard model: The attractive route*. Phys. Rev. A **79**, 033620 (2009). (Cited on pages **10** and **104**)

[128] D. P. Arovas, E. Berg, S. A. Kivelson, and S. Raghu. *The Hubbard Model*. Annu. Rev. Condens. Matter Phys. **13**, 239–274 (2022). (Cited on page **10**)

[129] A. Auerbach. *Interacting Electrons and Quantum Magnetism*. Springer New York, NY (1994). (Cited on page **10**)

[130] *90 - THE THEORY OF A FERMI LIQUID*. In *Collected Papers of L.D. Landau*, pages 723–730. Pergamon (1965). (Cited on page **11**)

[131] M. L. Néel. *Propriétés magnétiques des ferrites ; ferrimagnétisme et antiferromagnétisme*. Ann. Phys. **12**, 137–198 (1948). (Cited on page **12**)

[132] N. D. Mermin and H. Wagner. *Absence of Ferromagnetism or Antiferromagnetism in One- or Two-Dimensional Isotropic Heisenberg Models*. Phys. Rev. Lett. **17**, 1133–1136 (1966). (Cited on pages **12** and **70**)

[133] H. J. Metcalf and P. v. d. Straten. *Laser Cooling and Trapping*. Springer New York, NY (1999). (Cited on page **12**)

[134] W. Zwerger. *Mott-Hubbard transition of cold atoms in optical lattices*. J. Opt. B Quantum Semiclass. Opt. **5**, S9 (2003). (Cited on page **14**)

[135] J. Weiner, V. S. Bagnato, S. Zilio, and P. S. Julienne. *Experiments and theory in cold and ultracold collisions*. Rev. Mod. Phys. **71**, 1–85 (1999). (Cited on page **14**)

[136] H. Feshbach. *Unified theory of nuclear reactions*. Ann. Phys. **5**, 357–390 (1958). (Cited on page **15**)

[137] H. Feshbach. *A unified theory of nuclear reactions. II*. Ann. Phys. **19**, 287–313 (1962). (Cited on page **15**)

[138] U. Fano. *Effects of Configuration Interaction on Intensities and Phase Shifts*. Phys. Rev. **124**, 1866–1878 (1961). (Cited on page **15**)

[139] C. Chin, R. Grimm, P. Julienne, and E. Tiesinga. *Feshbach resonances in ultracold gases*. Rev. Mod. Phys. **82**, 1225–1286 (2010). (Cited on pages **15**, **16**, and **17**)

[140] A. Omran. *A microscope for Fermi Gases*. PhD thesis, Ludwig-Maximilians-Universität München (2016). (Cited on pages **16** and **18**)

[141] M. Boll. *Spin and Density Resolved Microscopy of Hubbard chains*. PhD thesis, Ludwig-Maximilians-Universität München (2016). (Cited on pages **16**, **20**, and **51**)

[142] J. Koepsell. *Quantum simulation of doped two-dimensional Mott insulators*. PhD thesis, Ludwig-Maximilians-Universität München (2021). (Cited on pages **16**, **17**, **19**, **22**, and **36**)

[143] M. E. Gehm. *Preparation of an optically-trapped degenerate Fermi gas of 6Li: Finding the route to degeneracy*. PhD thesis, Duke University (2003). (Cited on pages **16** and **33**)

[144] P. M. Duarte, R. A. Hart, J. M. Hitchcock, T. A. Corcovilos, T.-L. Yang, A. Reed, and R. G. Hulet. *All-optical production of a lithium quantum gas using narrow-line laser cooling*. Phys. Rev. A **84**, 061406 (2011). (Cited on page **16**)

[145] G. Zürn, T. Lompe, A. N. Wenz, S. Jochim, P. S. Julienne, and J. M. Hutson. *Precise Characterization of* ^{6}Li *Feshbach Resonances Using Trap-Sideband-Resolved RF Spectroscopy of Weakly Bound Molecules*. Phys. Rev. Lett. **110**, 135301 (2013). (Cited on page **17**)

[146] A. T. Grier, I. Ferrier-Barbut, B. S. Rem, M. Delehaye, L. Khaykovich, F. Chevy, and C. Salomon. *Λ-enhanced sub-Doppler cooling of lithium atoms in* D_1 *gray molasses*. Phys. Rev. A **87**, 063411 (2013). (Cited on page **18**)

[147] F. Sievers, N. Kretzschmar, D. R. Fernandes, D. Suchet, M. Rabinovic, S. Wu, C. V. Parker, L. Khaykovich, C. Salomon, and F. Chevy. *Simultaneous sub-Doppler laser cooling of fermionic* ^{6}Li *and* ^{40}K *on the* D_1 *line: Theory and experiment*. Phys. Rev. A **91**, 023426 (2015). (Cited on page **18**)

[148] A. Burchianti, J. A. Seman, G. Valtolina, A. Morales, M. Inguscio, M. Zaccanti, and G. Roati. *All-optical production of* ^{6}Li *quantum gases*. J. Phys.: Conf. Ser. **594**, 012042 (2015). (Cited on page **18**)

[149] K. N. Blodgett, D. Peana, S. S. Phatak, L. M. Terry, M. P. Montes, and J. D. Hood. *Imaging a* ^{6}Li *Atom in an Optical Tweezer 2000 Times with Λ-Enhanced Gray Molasses*. Phys. Rev. Lett. **131**, 083001 (2023). (Cited on page **18**)

[150] D. Bourgund. *High-Stability, Tunable, Bichromatic Superlattice*. Master thesis, Ludwig-Maximilians-Universität München (2019). (Cited on pages **19**, **34**, **36**, **39**, and **44**)

[151] S. Hirthe. *Quantum gas microscopy of Fermi-Hubbard ladders*. PhD thesis, Ludwig-Maximilians-Universität München (2023). (Cited on pages **19** and **25**)

[152] D. Wei. *Development of a Spatially Incoherent Laser Source*. Master thesis, Technische Universität München (2019). (Cited on page **19**)

[153] R. W. Floyd and L. Steinberg. *An Adaptive Algorithm for Spatial Greyscale*. Proc. Soc. Inf. Disp. **17**, 75–77 (1976). (Cited on page **20**)

[154] A. Mazurenko. *Probing Long Range Antiferromagnetism and Dynamics in the Fermi-Hubbard Model*. PhD thesis, Harvard University (2017). (Cited on page **20**)

[155] C. S. Chiu, G. Ji, A. Mazurenko, D. Greif, and M. Greiner. *Quantum State Engineering of a Hubbard System with Ultracold Fermions*. Phys. Rev. Lett. **120**, 243201 (2018). (Cited on pages **20** and **84**)

[156] M. Prentiss, A. Cable, J. E. Bjorkholm, S. Chu, E. L. Raab, and D. E. Pritchard. *Atomic-density-dependent losses in an optical trap*. Opt. Lett. **13**, 452–454 (1988). (Cited on page **22**)

[157] M. T. DePue, C. McCormick, S. L. Winoto, S. Oliver, and D. S. Weiss. *Unity Occupation of Sites in a 3D Optical Lattice*. Phys. Rev. Lett. **82**, 2262–2265 (1999). (Cited on page **22**)

[158] N. Schlosser, G. Reymond, I. Protsenko, and P. Grangier. *Sub-poissonian loading of single atoms in a microscopic dipole trap*. Nature **411**, 1024–1027 (2001). (Cited on page **22**)

[159] M. Lohse, C. Schweizer, O. Zilberberg, M. Aidelsburger, and I. Bloch. *A Thouless quantum pump with ultracold bosonic atoms in an optical superlattice*. Nat. Phys. **12**, 350–354 (2016). (Cited on pages **23** and **32**)

[160] S. Nakajima, T. Tomita, S. Taie, T. Ichinose, I. Ozawa, L. Wang, M. Troyer, and Y. Takahashi. *Topological Thouless pumping of ultracold fermions*. Nat. Phys. **12**, 296–300 (2016). (Cited on page **23**)

[161] D. J. Thouless. *Quantization of particle transport*. Phys. Rev. B **27**, 6083–6087 (1983). (Cited on page **23**)

[162] O. Romero-Isart and J. J. García-Ripoll. *Quantum ratchets for quantum communication with optical superlattices*. Phys. Rev. A **76**, 052304 (2007). (Cited on page **23**)

[163] N. Cantale, F. Courbin, M. Tewes, P. Jablonka, and G. Meylan. *Firedec: a two-channel finite-resolution image deconvolution algorithm*. A&A **589**, A81 (2016). (Cited on page **24**)

[164] P. Sompet, S. Hirthe, B. D., T. Chalopin, J. Bibo, J. Koepsell, P. Bojović, R. Verresen, F. Pollmann, G. Salomon, C. Gross, T. A. Hilker, and I. Bloch. *Realizing the symmetry-protected Haldane phase in Fermi-Hubbard ladders*. Nature **606**, 484–488 (2022). (Cited on pages **25** and **65**)

[165] F. D. M. Haldane. *Nonlinear Field Theory of Large-Spin Heisenberg Antiferromagnets: Semiclassically Quantized Solitons of the One-Dimensional Easy-Axis Néel State*. Phys. Rev. Lett. **50**, 1153 (1983). (Cited on page **25**)

[166] F. D. M. Haldane. *Topological Quantum Matter*. Int. Journ. Mod. Phys. B **32**, 1830004 (2018). (Cited on page **25**)

[167] M. den Nijs and K. Rommelse. *Preroughening transitions in crystal surfaces and valence-bond phases in quantum spin chains*. Phys. Rev. B **40**, 4709–4734 (1989). (Cited on pages **25** and **26**)

[168] T. Kennedy and H. Tasaki. *Hidden $Z_2 \times Z_2$ symmetry breaking in Haldane-gap antiferromagnets*. Phys. Rev. B **45**, 304–307 (1992). (Cited on page **25**)

[169] W. J. L. Buyers, R. M. Morra, R. L. Armstrong, M. J. Hogan, P. Gerlach, and K. Hirakawa. *Experimental evidence for the Haldane gap in a spin-1 nearly isotropic, antiferromagnetic chain*. Phys. Rev. Lett. **56**, 371–374 (1986). (Cited on page **25**)

[170] J. P. Renard, M. Verdaguer, L. P. Regnault, W. A. C. Erkelens, J. Rossat-Mignod, and W. G. Stirling. *Presumption for a Quantum Energy Gap in the Quasi-One-Dimensional $S = 1$ Heisenberg Antiferromagnet* $Ni(C_2H_8N_2)_2NO_2(ClO_4)$. Europhys. Lett. **3**, 945 (1987). (Cited on page **25**)

[171] M. Hagiwara, K. Katsumata, I. Affleck, B. I. Halperin, and J. P. Renard. *Observation of S=1/2 degrees of freedom in an S=1 linear-chain Heisenberg antiferromagnet*. Phys. Rev. Lett. **65**, 3181–3184 (1990). (Cited on page **25**)

[172] S. H. Glarum, S. Geschwind, K. M. Lee, M. L. Kaplan, and J. Michel. *Observation of fractional spin S=1/2 on open ends of S=1 linear antiferromagnetic chains: Nonmagnetic doping*. Phys. Rev. Lett. **67**, 1614–1617 (1991). (Cited on page **25**)

[173] I. Affleck, T. Kennedy, E. H. Lieb, and H. Tasaki. *Rigorous results on valence-bond ground states in antiferromagnets*. Phys. Rev. Lett. **59**, 799–802 (1987). (Cited on page **25**)

[174] K. Hida. *Crossover between the Haldane-gap phase and the dimer phase in the spin-1/2 alternating Heisenberg chain*. Phys. Rev. B **45**, 2207–2212 (1992). (Cited on page **25**)

[175] S. R. White. *Equivalence of the antiferromagnetic Heisenberg ladder to a single S=1 chain*. Phys. Rev. B **53**, 52–55 (1996). (Cited on page **25**)

[176] F. Pollmann and A. M. Turner. *Detection of symmetry-protected topological phases in one dimension*. Phys. Rev. B **86**, 125441 (2012). (Cited on page **26**)

[177] F. Anfuso and A. Rosch. *Fragility of string orders*. Phys. Rev. B **76**, 085124 (2007). (Cited on page **27**)

[178] S. Moudgalya and F. Pollmann. *Fragility of symmetry-protected topological order on a Hubbard ladder*. Phys. Rev. B **91**, 155128 (2015). (Cited on page **27**)

[179] R. Verresen, J. Bibo, and F. Pollmann. *Quotient symmetry protected topological phenomena*. arXiv.2102.08967 (2021). (Cited on page **27**)

[180] T. Chalopin, P. Bojović, D. Bourgund, S. Wang, T. Franz, I. Bloch, and T. A. Hilker. *Optical superlattice for engineering Hubbard couplings in quantum simulation*. arXiv.2405.19322 (2024). (Cited on page **29**)

[181] B. P. Anderson, T. L. Gustavson, and M. A. Kasevich. *Atom trapping in nondissipative optical lattices*. Phys. Rev. A **53**, R3727–R3730 (1996). (Cited on page **29**)

[182] P. Soltan-Panahi, J. Struck, P. Hauke, A. Bick, W. Plenkers, G. Meineke, C. Becker, P. Windpassinger, M. Lewenstein, and K. Sengstock. *Multi-component quantum gases in spin-dependent hexagonal lattices*. Nat. Phys. **7**, 434–440 (2011). (Cited on page **29**)

[183] G.-B. Jo, J. Guzman, C. K. Thomas, P. Hosur, A. Vishwanath, and D. M. Stamper-Kurn. *Ultracold Atoms in a Tunable Optical Kagome Lattice*. Phys. Rev. Lett. **108**, 045305 (2012). (Cited on page **29**)

[184] S. Taie, H. Ozawa, T. Ichinose, T. Nishio, S. Nakajima, and Y. Takahashi. *Coherent driving and freezing of bosonic matter wave in an optical Lieb lattice*. Sci. Adv. **1**, e1500854 (2015). (Cited on page **29**)

[185] G. D. Domenico, N. Castagna, M. D. Plimmer, P. Thomann, A. V. Taichenachev, and V. I. Yudin. *On the stability of optical lattices*. arXiv.physics/0412072 (2004). (Cited on page **29**)

[186] M. N. Kosch, L. Asteria, H. P. Zahn, K. Sengstock, and C. Weitenberg. *Multifre-*

quency optical lattice for dynamic lattice-geometry control. Phys. Rev. Res. **4**, 043083 (2022). (Cited on pages **30**, **31**, and **51**)

[187] D.-S. Lühmann, O. Jürgensen, M. Weinberg, J. Simonet, P. Soltan-Panahi, and K. Sengstock. *Quantum phases in tunable state-dependent hexagonal optical lattices*. Phys. Rev. A **90**, 013614 (2014). (Cited on pages **30** and **31**)

[188] D. Wei. *Microscopy of spin hydrodynamics and cooperative light scattering in atomic Hubbard systems*. PhD thesis, Ludwig-Maximilians-Universität München (2023). (Cited on pages **30**, **31**, and **51**)

[189] R. A. Williams, J. D. Pillet, S. Al-Assam, B. Fletcher, M. Shotter, and C. J. Foot. *Dynamic optical lattices: two-dimensional rotating and accordion lattices for ultracold atoms*. Opt. Express **16**, 16977–16983 (2008). (Cited on pages **30** and **31**)

[190] T. C. Li, H. Kelkar, D. Medellin, and M. G. Raizen. *Real-time control of the periodicity of a standing wave: an optical accordion*. Opt. Express **16**, 5465–5470 (2008). (Cited on page **30**)

[191] J. Tao, Y. Wang, Y. He, and S. Wu. *Wavelength-limited optical accordion*. Opt. Express **26**, 14346–14355 (2018). (Cited on page **30**)

[192] D. Greif, M. F. Parsons, A. Mazurenko, C. S. Chiu, S. Blatt, F. Huber, G. Ji, and M. Greiner. *Site-resolved imaging of a fermionic Mott insulator*. Science **351**, 953–957 (2016). (Cited on page **30**)

[193] J. Mongkolkiattichai, L. Liu, D. Garwood, J. Yang, and P. Schauss. *Quantum gas microscopy of fermionic triangular-lattice Mott insulators*. Phys. Rev. A **108**, L061301 (2023). (Cited on page **30**)

[194] J. Sebby-Strabley, M. Anderlini, P. S. Jessen, and J. V. Porto. *Lattice of double wells for manipulating pairs of cold atoms*. Phys. Rev. A **73**, 033605 (2006). (Cited on page **32**)

[195] J. Sebby-Strabley, B. L. Brown, M. Anderlini, P. J. Lee, W. D. Phillips, J. V. Porto, and P. R. Johnson. *Preparing and Probing Atomic Number States with an Atom Interferometer*. Phys. Rev. Lett. **98**, 200405 (2007). (Cited on page **32**)

[196] S. Fölling, S. Trotzky, P. Cheinet, M. Feld, R. Saers, A. Widera, T. Müller, and I. Bloch. *Direct observation of second-order atom tunnelling*. Nature **448**, 1029–1032 (2007). (Cited on page **32**)

[197] S. Trotzky, P. Cheinet, S. Fölling, M. Feld, U. Schnorrberger, A. M. Rey, A. Polkovnikov, E. A. Demler, M. D. Lukin, and I. Bloch. *Time-Resolved Ob-*

servation and Control of Superexchange Interactions with Ultracold Atoms in Optical Lattices. Science **319**, 295–299 (2008). (Cited on pages **32** and **65**)

[198] B. Yang, H. Sun, C.-J. Huang, H.-Y. Wang, Y. Deng, H.-N. Dai, Z.-S. Yuan, and J.-W. Pan. *Cooling and entangling ultracold atoms in optical lattices*. Science **369**, 550–553 (2020). (Cited on pages **32**, **78**, and **107**)

[199] L. Asteria, H. P. Zahn, M. N. Kosch, K. Sengstock, and C. Weitenberg. *Quantum gas magnifier for sub-lattice-resolved imaging of 3D quantum systems*. Nature **599**, 571–575 (2021). (Cited on page **32**)

[200] T. Tiecke. *Feshbach resonances in ultracold mixtures of the fermionic quantum gases 6Li and 40K*. PhD thesis, University of Amsterdam (2009). (Cited on page **33**)

[201] D. A. Steck. *Rubidium 87 D Line Data* (2001). http://steck.us/alkalidata. (Cited on page **33**)

[202] A. Heinz, J. Trautmann, N. Šantić, A. J. Park, I. Bloch, and S. Blatt. *Crossed optical cavities with large mode diameters*. Opt. Lett. **46**, 250–253 (2021). (Cited on page **33**)

[203] A. J. Park, J. Trautmann, N. Šantić, V. Klüsener, A. Heinz, I. Bloch, and S. Blatt. *Cavity-Enhanced Optical Lattices for Scaling Neutral Atom Quantum Technologies to Higher Qubit Numbers*. PRX Quantum **3**, 030314 (2022). (Cited on page **33**)

[204] B. Edlén. *The Refractive Index of Air*. Metrologia **2** (1966). (Cited on page **35**)

[205] K. P. Birch and M. J. Downs. *Correction to the Updated Edlén Equation for the Refractive Index of Air*. Metrologia **31** (1994). (Cited on page **35**)

[206] D. Bourgund, T. Chalopin, P. Bojović, H. Schlömer, S. Wang, T. Franz, S. Hirthe, A. Bohrdt, F. Grusdt, I. Bloch, and T. A. Hilker. *Formation of stripes in a mixed-dimensional cold-atom Fermi-Hubbard system*. arXiv.2312.14156 (2023). (Cited on pages **37**, **69**, and **98**)

[207] D. S. Hum, R. K. Route, G. D. Miller, V. Kondilenko, A. Alexandrovski, J. Huang, K. Urbanek, R. L. Byer, and M. M. Fejer. *Optical properties and ferroelectric engineering of vapor-transport-equilibrated, near-stoichiometric lithium tantalate for frequency conversion*. J. Appl. Phys. **101**, 093108 (2007). (Cited on page **38**)

[208] S. Tovstonog, S. Kurimura, I. Suzuki, K. Takeno, S. Moriwaki, N. Ohmae, N. Mio, and T. Katagai. *Thermal effects in high-power CW second harmonic generation in Mg-doped stoichiometric lithium tantalate*. Opt. express **16**, 11294–9 (2008). (Cited on page **38**)

[209] S. C. Kumar, G. K. Samanta, and M. Ebrahim-Zadeh. *High-power, single-frequency, continuous-wave second-harmonic-generation of ytterbium fiber laser in PPKTP and MgO:sPPLT*. Opt. express. **17**, 13711–26 (2009). (Cited on page **38**)

[210] S. G. Sabouri, S. C. Kumar, A. Khorsandi, and M. Ebrahim-Zadeh. *Thermal Effects in High-Power Continuous-Wave Single-Pass Second Harmonic Generation*. IEEE J. Quantum Electron. **20**, 563–572 (2014). (Cited on page **39**)

[211] S. G. Sabouri and A. Khorsandi. *Active Control of Thermal Dephasing Effect in High Power Continuous Wave Single-Pass Second Harmonic Generation*. IEEE J. Quantum Electron. **51**, 1–8 (2015). (Cited on page **39**)

[212] M. Stappel, D. Kolbe, and J. Walz. *Continuous-wave, double-pass second-harmonic generation with 60% efficiency in a single MgO:PPSLT crystal*. Opt. Lett. **39**, 2951–2954 (2014). (Cited on page **39**)

[213] M.-D. Li, Y.-G. Zheng, W.-Y. Zhang, X.-K. Wang, B. Xiao, Z.-Y. Zhou, L. Jiang, M.-Z. Lian, Z.-S. Yuan, and J.-W. Pan. *A high-power and low-noise 532-nm continuous-wave laser for quantum gas microscopy*. Rev. Sci. Instrum. **92**, 083202 (2021). (Cited on page **39**)

[214] *Linear thermal expansion coefficient for metals* (2024). https://amesweb.info/Materials/Linear-Thermal-Expansion-Coefficient-Metals.aspx. (Cited on page **41**)

[215] *Macor® properties* (2024). https://www.morgantechnicalceramics.com/en-gb/products/macor-machinable-glass-ceramic/macor-properties/. (Cited on page **41**)

[216] *36 ALLOY Invar Properties & Low Coefficient of Thermal Expansion* (2024). https://www.nealloys.com/invar_invar.php. (Cited on page **41**)

[217] *Zerodur®* (2024). https://www.schott.com/en-cz/products/zerodur-p1000269/technical-details. (Cited on page **41**)

[218] T. Döhring, P. Hartmann, R. Jedamzik, A. Thomas, and F.-T. Lentes. *Properties of Zerodur mirror blanks for extremely large telescopes*. SPIE **6148**, 61480G (2006). (Cited on page **41**)

[219] M. Mihm, J. P. Marburger, A. Wenzlawski, O. Hellmig, O. Anton, K. Döringshoff, M. Krutzik, A. Peters, P. Windpassinger, and the MAIUS Team. *ZERODUR based optical systems for quantum gas experiments in space*. Acta Astronaut. **159**, 166–169 (2019). (Cited on page **41**)

[220] M. Mihm. *Laser System Technology for Quantum Experiments in Space and beyond*. PhD thesis, Johannes Gutenberg-Universität Mainz (2020). (Cited on pages **41** and **42**)

[221] J. Li, W. Huang, B. Shteynas, S. Burchesky, F. C. Top, E. Su, J. Lee, A. O. Jamison, and W. Ketterle. *Spin-Orbit Coupling and Spin Textures in Optical Superlattices*. Phys. Rev. Lett. **117**, 185301 (2016). (Cited on page **45**)

[222] M. Lohse. *Topological charge pumping with ultracold bosonic atoms in optical superlattices*. PhD thesis, Ludwig-Maximilians-Universität München (2018). (Cited on page **51**)

[223] S. Scherg. *Probing nonequilibrium dynamics in Fermi-Hubbard chains - from extensively-many to few conserved quantities*. PhD thesis, Ludwig-Maximilians-Universität München (2021). (Cited on page **51**)

[224] Z. Li, P. Liu, P. Zhao, M. Z., H. Xu, X. Liang, T. Su, W. Sun, G. Xue, J.-N. Zhang, W. Liu, Y. Jin, and H. Yu. *Error per single-qubit gate below* 10^{-4} *in a superconducting qubit*. npj Quantum Inf **9**, 111 (2023). (Cited on pages **51** and **64**)

[225] P. W. Anderson. *Absence of Diffusion in Certain Random Lattices*. Phys. Rev. **109**, 1492–1505 (1958). (Cited on page **53**)

[226] P. M. Preiss, R. Ma, M. E. Tai, A. Lukin, M. Rispoli, P. Zupancic, Y. Lahini, R. Islam, and M. Greiner. *Strongly correlated quantum walks in optical lattices*. Science **347**, 1229–1233 (2015). (Cited on page **57**)

[227] D. Jaksch, H.-J. Briegel, J. I. Cirac, C. W. Gardiner, and P. Zoller. *Entanglement of Atoms via Cold Controlled Collisions*. Phys. Rev. Lett. **82**, 1975–1978 (1999). (Cited on pages **63** and **108**)

[228] S. B. Bravyi and A. Y. Kitaev. *Fermionic Quantum Computation*. Ann. Phys. **298**, 210–226 (2002). (Cited on pages **63**, **67**, and **108**)

[229] S. Murmann, A. Bergschneider, V. M. Klinkhamer, G. Zürn, T. Lompe, and S. Jochim. *Two Fermions in a Double Well: Exploring a Fundamental Building Block of the Hubbard Model*. Phys. Rev. Lett. **114**, 080402 (2015). (Cited on pages **63** and **67**)

[230] A. Bergschneider, V. Klinkhammer, J. Becher, R. Klemt, L. Palm, G. Zürn, S. Jochim, and P. M. Preiss. *Experimental characterization of two-particle entanglement through position and momentum correlations*. Nat. Phys. **15**, 640–644 (2019). (Cited on page **63**)

[231] D. González-Cuadra, D. Bluvstein, M. Kalinowski, R. Kaubruegger,

N. Maskara, P. Naldesi, T. V. Zache, A. M. Kaufman, M. D. Lukin, H. Pichler, B. Vermersch, J. Ye, and P. Zoller. *Fermionic quantum processing with programmable neutral atom arrays*. PNAS **120**, e2304294120 (2023). (Cited on pages **63** and **108**)

[232] B. M. Spar, E. Guardado-Sanchez, S. Chi, Z. Z. Yan, and W. S. Bakr. *Realization of a Fermi-Hubbard Optical Tweezer Array*. Phys. Rev. Lett. **128**, 223202 (2022). (Cited on page **63**)

[233] D. Jaksch, J. I. Cirac, P. Zoller, S. L. Rolston, R. Côté, and M. D. Lukin. *Fast Quantum Gates for Neutral Atoms*. Phys. Rev. Lett. **85**, 2208–2211 (2000). (Cited on page **63**)

[234] D. Bluvstein, H. Levine, G. Semeghini, T. T. Wang, S. Ebadi, M. Kalinowski, A. Keesling, N. Maskara, H. Pichler, M. Greiner, V. Vuletić, and M. D. Lukin. *A quantum processor based on coherent transport of entangled atom arrays*. Nature **604**, 451–456 (2022). (Cited on page **63**)

[235] S. J. Evered, M. Kalinowski, T. Manovitz, H. Zhou, S. H. Li, A. A. Geim, T. T. Wang, N. Maskara, H. Levine, G. Semeghini, M. Greiner, V. Vuletić, and M. D. Lukin. *High-fidelity parallel entangling gates on a neutral-atom quantum computer*. Nature **622**, 268–272 (2023). (Cited on page **63**)

[236] T. Xia, M. Lichtman, K. Maller, A. W. Carr, M. J. Piotrowicz, L. Isenhower, and M. Saffman. *Randomized Benchmarking of Single-Qubit Gates in a 2D Array of Neutral-Atom Qubits*. Phys. Rev. Lett. **114**, 100503 (2015). (Cited on page **63**)

[237] Y. Wang, A. Kumar, T.-Y. Wu, and D. S. Weiss. *Single-qubit gates based on targeted phase shifts in a 3D neutral atom array*. Science **352**, 1562–1565 (2016). (Cited on page **63**)

[238] T. M. Graham, M. Kwon, B. Grinkemeyer, Z. Marra, X. Jiang, M. T. Lichtman, Y. Sun, M. Ebert, and M. Saffman. *Rydberg-Mediated Entanglement in a Two-Dimensional Neutral Atom Qubit Array*. Phys. Rev. Lett. **123**, 230501 (2019). (Cited on page **63**)

[239] I. Madjarov, J. Covey, A. Shaw, J. Choi, A. Kale, A. Cooper, H. Pichler, V. Schkolnik, J. Williams, and M. Endres. *High-fidelity entanglement and detection of alkaline-earth Rydberg atoms*. Nat. Phys. **16**, 857–861 (2020). (Cited on page **63**)

[240] H. Levine, D. Bluvstein, A. Keesling, T. T. Wang, S. Ebadi, G. Semeghini, A. Omran, M. Greiner, V. Vuletić, and M. D. Lukin. *Dispersive optical systems for scalable Raman driving of hyperfine qubits*. Phys. Rev. A **105**, 032618 (2022). (Cited on page **63**)

[241] A. Jenkins, J. W. Lis, A. Senoo, W. F. McGrew, and A. M. Kaufman. *Ytterbium Nuclear-Spin Qubits in an Optical Tweezer Array*. Phys. Rev. X **12**, 021027 (2022). (Cited on page **63**)

[242] S. Ma, A. P. Burgers, G. Liu, J. Wilson, B. Zhang, and J. D. Thompson. *Universal Gate Operations on Nuclear Spin Qubits in an Optical Tweezer Array of* ^{171}Yb *Atoms*. Phys. Rev. X **12**, 021028 (2022). (Cited on page **63**)

[243] C. Sheng, X. He, P. Xu, R. Guo, K. Wang, Z. Xiong, M. Liu, J. Wang, and M. Zhan. *High-Fidelity Single-Qubit Gates on Neutral Atoms in a Two-Dimensional Magic-Intensity Optical Dipole Trap Array*. Phys. Rev. Lett. **121**, 240501 (2018). (Cited on page **64**)

[244] R. Guo, X. He, C. Sheng, J. Yang, P. Xu, K. Wang, J. Zhong, M. Liu, J. Wang, and M. Zhan. *Balanced Coherence Times of Atomic Qubits of Different Species in a Dual* 3×3 *Magic-Intensity Optical Dipole Trap Array*. Phys. Rev. Lett. **124**, 153201 (2020). (Cited on page **64**)

[245] A. Mills, C. Guinn, M. Feldman, A. Sigillito, M. Gullans, M. Rakher, J. Kerckhoff, C. Jackson, and J. Petta. *High-Fidelity State Preparation, Quantum Control, and Readout of an Isotopically Enriched Silicon Spin Qubit*. Phys. Rev. Appl. **18**, 064028 (2022). (Cited on page **64**)

[246] X. Rong, J. Geng, F. Shi, Y. Liu, K. Xu, W. Ma, F. Kong, Z. Jiang, Y. Wu, and J. Du. *Experimental fault-tolerant universal quantum gates with solid-state spins under ambient conditions*. Nat. Commun. **6**, 8748 (2015). (Cited on page **64**)

[247] T. P. Harty, D. T. C. Allcock, C. J. Ballance, L. Guidoni, H. A. Janacek, N. M. Linke, D. N. Stacey, and D. M. Lucas. *High-Fidelity Preparation, Gates, Memory, and Readout of a Trapped-Ion Quantum Bit*. Phys. Rev. Lett. **113**, 220501 (2014). (Cited on page **64**)

[248] A. D. Leu, M. F. Gely, M. A. Weber, M. C. Smith, D. P. Nadlinger, and D. M. Lucas. *Fast, High-Fidelity Addressed Single-Qubit Gates Using Efficient Composite Pulse Sequences*. Phys. Rev. Lett. **131**, 120601 (2023). (Cited on page **64**)

[249] L.-M. Duan, E. Demler, and M. D. Lukin. *Controlling Spin Exchange Interactions of Ultracold Atoms in Optical Lattices*. Phys. Rev. Lett. **91**, 090402 (2003). (Cited on page **65**)

[250] A. Kantian, S. Langer, and A. J. Daley. *Dynamical Disentangling and Cooling of Atoms in Bilayer Optical Lattices*. Phys. Rev. Lett. **120**, 060401 (2018). (Cited on pages **67**, **78**, and **107**)

[251] M. Lubasch, V. Murg, U. Schneider, J. I. Cirac, and M.-C. Bañuls. *Adiabatic Preparation of a Heisenberg Antiferromagnet Using an Optical Superlattice*. Phys. Rev. Lett. **107**, 165301 (2011). (Cited on pages **67**, **78**, and **107**)

[252] F. Miao, H., R. G., Koch, D. Mazzone, C. Nelson, R. Acevedo-Esteves, G. Gu, T. Yilimaz, K. Kaznatcheev, E. Vescovo, M. Oda, T. Kurosawa, N. Momono, T. Assefa, I. Robinson, E. Bozin, J. Tranquada, P. Johnson, and M. Dean. *Charge density waves in cuprate superconductors beyond the critical doping*. npj Quantum Mater. **6** (2021). (Cited on page **70**)

[253] M. Hücker, M. v. Zimmermann, G. D. Gu, Z. J. Xu, J. S. Wen, G. Xu, H. J. Kang, A. Zheludev, and J. M. Tranquada. *Stripe order in superconducting* $La_{2-x}Ba_xCuO_4(0.095 \leqslant x \leqslant 0.155)$. Phys. Rev. B **83**, 104506 (2011). (Cited on page **70**)

[254] P. W. Anderson. *The Resonating Valence Bond State in* La_2CuO_4 *and Superconductivity*. Science **235**, 1196 (1987). (Cited on page **69**)

[255] J. M. Tranquada, D. J. Buttrey, V. Sachan, and J. E. Lorenzo. *Simultaneous Ordering of Holes and Spins in* $La_2NiO_{4.125}$. Phys. Rev. Lett. **73**, 1003–1006 (1994). (Cited on page **71**)

[256] V. Sachan, D. J. Buttrey, J. M. Tranquada, J. E. Lorenzo, and G. Shirane. *Charge and spin ordering in* $La_{2-x}Sr_xNiO_{4.00}$ *with x=0.135 and 0.20*. Phys. Rev. B **51**, 12742–12746 (1995). (Cited on page **71**)

[257] J. M. Tranquada, A. H. Moudden, A. I. Goldman, P. Zolliker, D. E. Cox, G. Shirane, S. K. Sinha, D. Vaknin, D. C. Johnston, M. S. Alvarez, A. J. Jacobson, J. T. Lewandowski, and J. M. Newsam. *Antiferromagnetism in* $YBa_2Cu_3O_{6+x}$. Phys. Rev. B **38**, 2477–2485 (1988). (Cited on page **71**)

[258] R. J. Birgeneau, D. R. Gabbe, H. P. Jenssen, M. A. Kastner, P. J. Picone, T. R. Thurston, G. Shirane, Y. Endoh, M. Sato, K. Yamada, Y. Hidaka, M. Oda, Y. Enomoto, M. Suzuki, and T. Murakami. *Antiferromagnetic spin correlations in insulating, metallic, and superconducting* $La_{2-x}Sr_xCuO_4$. Phys. Rev. B **38**, 6614–6623 (1988). (Cited on page **71**)

[259] H. Yoshizawa, S. Mitsuda, H. Kitazawa, and K. Katsumata. *An Incommensurate Magnetic Diffuse Scattering in Superconducting* $La_{1.92}Sr_{0.08}CuO_{4-\delta}$. J. Phys. Soc. Jpn. **57**, 3686–3689 (1988). (Cited on page **71**)

[260] R. J. Birgeneau, Y. Endoh, K. Kakurai, Y. Hidaka, T. Murakami, M. A. Kastner, T. R. Thurston, G. Shirane, and K. Yamada. *Static and dynamic spin fluctuations*

in superconducting $La_{2-x}Sr_xCuO_4$. Phys. Rev. B **39**, 2868–2871 (1989). (Cited on page **71**)

[261] S.-W. Cheong, G. Aeppli, T. E. Mason, H. Mook, S. M. Hayden, P. C. Canfield, Z. Fisk, K. N. Clausen, and J. L. Martinez. *Incommensurate magnetic fluctuations in* $La_{2-x}Sr_xCuO_4$. Phys. Rev. Lett. **67**, 1791–1794 (1991). (Cited on page **71**)

[262] T. R. Thurston, P. M. Gehring, G. Shirane, R. J. Birgeneau, M. A. Kastner, Y. Endoh, M. Matsuda, K. Yamada, H. Kojima, and I. Tanaka. *Low-energy incommensurate spin excitations in superconducting* $La_{1.85}Sr_{0.15}CuO_4$. Phys. Rev. B **46**, 9128–9131 (1992). (Cited on page **71**)

[263] T. E. Mason, G. Aeppli, and H. A. Mook. *Magnetic dynamics of superconducting* $La_{1.86}Sr_{0.14}CuO_4$. Phys. Rev. Lett. **68**, 1414–1417 (1992). (Cited on page **71**)

[264] O. Zachar, S. A. Kivelson, and V. J. Emery. *Landau theory of stripe phases in cuprates and nickelates*. Phys. Rev. B **57**, 1422–1426 (1998). (Cited on page **71**)

[265] M. K. Crawford, R. L. Harlow, E. M. McCarron, W. E. Farneth, J. D. Axe, H. Chou, and Q. Huang. *Lattice instabilities and the effect of copper-oxygen-sheet distortions on superconductivity in doped* La_2CuO_4. Phys. Rev. B **44**, 7749–7752 (1991). (Cited on page **71**)

[266] B. Büchner, M. Breuer, M. Cramm, A. Freimuth, H. Micklitz, W. Schlabitz, and A. Kampf. *Superconducting/non-superconducting phase boundary in the low temperature tetragonal phase of (La,RE)-Sr-Cu-O*. J. Low. Temp. Phys. **95**, 285–291 (1994). (Cited on page **71**)

[267] H. J. Schulz. *Domain walls in a doped antiferromagnet*. J. Phys. France **50**, 2833–2849 (1989). (Cited on pages **72** and **74**)

[268] R. Birgeneau, C. Stock, J. Tranquada, and K. Yamada. *Magnetic Neutron Scattering in Hole-Doped Cuprate Superconductors*. J. Phys. Soc. Jpn. **75**, 111003 (2006). (Cited on page **72**)

[269] M. S. D. A. Hussein, E. Dagotto, and A. Moreo. *Half-filled stripes in a hole-doped three-orbital spin-fermion model for cuprates*. Phys. Rev. B **99**, 115108 (2019). (Cited on page **72**)

[270] A. Wietek, Y.-Y. He, S. R. White, A. Georges, and E. M. Stoudenmire. *Stripes, Antiferromagnetism, and the Pseudogap in the Doped Hubbard Model at Finite Temperature*. Phys. Rev. X **11**, 031007 (2021). (Cited on page **72**)

[271] H. Ulbrich and M. Braden. *Neutron scattering studies on stripe phases in non-cuprate materials*. Phys. C: Supercond. Appl. **481**, 31–45 (2012). (Cited on page **72**)

[272] J. R. Schrieffer, X.-G. Wen, and S.-C. Zhang. *Spin-bag mechanism of high-temperature superconductivity*. Phys. Rev. Lett. **60**, 944–947 (1988). (Cited on page **73**)

[273] J. M. Tranquada, J. D. Axe, N. Ichikawa, Y. Nakamura, S. Uchida, and B. Nachumi. *Neutron-scattering study of stripe-phase order of holes and spins in* $La_{1.48}Nd_{0.4}Sr_{0.12}CuO_4$. Phys. Rev. B **54**, 7489–7499 (1996). (Cited on page **73**)

[274] N. Ichikawa, S. Uchida, J. M. Tranquada, T. Niemöller, P. M. Gehring, S.-H. Lee, and J. R. Schneider. *Local Magnetic Order vs Superconductivity in a Layered Cuprate*. Phys. Rev. Lett. **85**, 1738–1741 (2000). (Cited on page **73**)

[275] J. E. Hoffman, E. W. Hudson, K. M. Lang, V. Madhavan, H. Eisaki, S. Uchida, and J. C. Davis. *A Four Unit Cell Periodic Pattern of Quasi-Particle States Surrounding Vortex Cores in* $Bi_2Sr_2CaCu_2O_{8+\delta}$. Science **295**, 466–469 (2002). (Cited on pages **73** and **74**)

[276] C. V. Parker, P. Aynajian, E. H. da Silva Neto, A. Pushp, S. Ono, J. Wen, Z. Xu, G. Gu, and A. Yazdani. *Fluctuating stripes at the onset of the pseudogap in the high-*T_c *superconductor* $Bi_2Sr_2CaCu_2O_{8+x}$. Nature **468**, 677–680 (2010). (Cited on page **73**)

[277] P. Cai, Y. Peng, C. Ye, X. Li, Z. Hao, X. Zhou, D.-H. Lee, and Y. Wang. *Visualizing the evolution from the Mott insulator to a charge-ordered insulator in lightly doped cuprates*. Nat. Phys. **12**, 1047–1051 (2016). (Cited on page **73**)

[278] T. Valla, A. V. Fedorov, J. Lee, J. C. Davis, and G. D. Gu. *The Ground State of the Pseudogap in Cuprate Superconductors*. Science **314**, 1914–1916 (2006). (Cited on page **73**)

[279] M. Jurkutat, A. Erb, and J. Haase. T_c *and Other Cuprate Properties in Relation to Planar Charges as Measured by NMR*. Condens. Matter **4** (2019). (Cited on page **73**)

[280] T. Mizokawa, A. Ino, T. Yoshida, A. Fujimori, C. Kim, H. Eisaki, S. Z.-X., S. Horii, T. Kakeshita, S. Uchida, K. Tomimoto, S. Tajima, and Y. Yamada. *ARPES study of LSCO and PBCO: Electronic structure of the stripe phase and the 1/4-filled Cu-O chains*. Int. J. Mod. Phys. B **14** (2000). (Cited on page **73**)

[281] C. H. Chen, S.-W. Cheong, and A. S. Cooper. *Charge modulations in* $La_{2-x}Sr_xNiO_{4+y}$*: Ordering of polarons*. Phys. Rev. Lett. **71**, 2461–2464 (1993). (Cited on page **73**)

[282] J. Li, Y. Zhu, J. M. Tranquada, K. Yamada, and D. J. Buttrey. *Transmission-*

electron-microscopy study of charge-stripe order in $La_{1.725}Sr_{0.275}NiO_4$. Phys. Rev. B **67**, 012404 (2003). (Cited on page **73**)

[283] D. Poilblanc and T. M. Rice. *Charged solitons in the Hartree-Fock approximation to the large-U Hubbard model*. Phys. Rev. B **39**, 9749–9752 (1989). (Cited on page **74**)

[284] J. Zaanen and O. Gunnarsson. *Charged magnetic domain lines and the magnetism of high-T_c oxides*. Phys. Rev. B **40**, 7391–7394 (1989). (Cited on page **74**)

[285] V. Thampy, X. M. Chen, Y. Cao, C. Mazzoli, A. M. Barbour, W. Hu, H. Miao, G. Fabbris, R. D. Zhong, G. D. Gu, J. M. Tranquada, I. K. Robinson, S. B. Wilkins, and M. P. M. Dean. *Static charge-density-wave order in the superconducting state of* $La_{2-x}Ba_xCuO_4$. Phys. Rev. B **95**, 241111 (2017). (Cited on page **76**)

[286] G. Ji, M. Xu, L. H. Kendrick, C. S. Chiu, J. C. Brüggenjürgen, D. Greif, A. Bohrdt, F. Grusdt, E. Demler, M. Lebrat, and M. Greiner. *Coupling a Mobile Hole to an Antiferromagnetic Spin Background: Transient Dynamics of a Magnetic Polaron*. Phys. Rev. X **11**, 021022 (2021). (Cited on page **78**)

[287] E. Blomquist and J. Carlström. *Evidence of attraction between charge carriers in a doped Mott insulator*. Phys. Rev. Res. **3**, 013272 (2021). (Cited on pages **78**, **104**, and **107**)

[288] A. Bohrdt, L. Homeier, I. Bloch, E. Demler, and F. Grusdt. *Strong pairing in mixed-dimensional bilayer antiferromagnetic Mott insulators*. Nat. Phys. **18**, 651–656 (2022). (Cited on pages **80** and **83**)

[289] H. Schlömer, A. Bohrdt, L. Pollet, U. Schollwöck, and F. Grusdt. *Robust stripes in the mixed-dimensional $t-J$ model*. Phys. Rev. Res. **5**, L022027 (2023). (Cited on page **81**)

[290] H. Sun, M. Huo, X. Hu, J. Li, Z. Liu, Y. Han, L. Tang, Z. Mao, P. Yang, B. Wang, J. Cheng, D.-X. Yao, G.-M. Zhang, and M. Wang. *Signatures of superconductivity near 80 K in a nickelate under high pressure*. Nature **621**, 493–498 (2023). (Cited on page **82**)

[291] X.-Z. Qu, D.-W. Qu, J. Chen, C. Wu, F. Yang, W. Li, and G. Su. *Bilayer $t-J-J_\perp$ Model and Magnetically Mediated Pairing in the Pressurized Nickelate* $La_3Ni_2O_7$. Phys. Rev. Lett. **132**, 036502 (2024). (Cited on page **82**)

[292] H. Schlömer, U. Schollwöck, F. Grusdt, and A. Bohrdt. *Superconductivity in the pressurized nickelate* $La_3Ni_2O_7$ *in the vicinity of a BEC-BCS crossover*. arXiv.2311.03349 (2023). (Cited on page **82**)

[293] A. Bohrdt, L. Homeier, C. Reinmoser, E. Demler, and F. Grusdt. *Exploration of doped quantum magnets with ultracold atoms*. Ann. Phys. **435**, 168651 (2021). (Cited on page **83**)

[294] T. Wu, H. Mayaffre, S. Krämer, M. Horvatić, C. Berthier, W. Hardy, R. Liang, D. A. Bonn, and M.-H. Julien. *Magnetic-field-induced charge-stripe order in the high-temperature superconductor* $YBa_2Cu_3O_y$. Nature **477**, 191–194 (2011). (Cited on page **100**)

[295] H. V. Kruis, I. P. McCulloch, Z. Nussinov, and J. Zaanen. *Geometry and the hidden order of Luttinger liquids: The universality of squeezed space*. Phys. Rev. B **70** (2004). (Cited on page **102**)

[296] J. M. Luttinger. *An Exactly Soluble Model of a Many-Fermion System*. J. Math. Phys. **4**, 1154–1162 (2004). (Cited on page **102**)

[297] T. A. Hilker, G. Salomon, F. Grusdt, A. Omran, M. Boll, E. Demler, I. Bloch, and C. Gross. *Revealing hidden antiferromagnetic correlations in doped Hubbard chains via string correlators*. Science **357**, 484–487 (2017). (Cited on page **102**)

[298] P. Fulde and R. A. Ferrell. *Superconductivity in a Strong Spin-Exchange Field*. Phys. Rev. **135**, A550–A563 (1964). (Cited on page **104**)

[299] A. I. Larkin and Y. N. Ovchinnikov. *Nonuniform state of superconductors*. Zh. Eksperim. i Teor. Fiz. **47** (1964). (Cited on page **104**)

[300] A. Moreo and D. J. Scalapino. *Cold Attractive Spin Polarized Fermi Lattice Gases and the Doped Positive U Hubbard Model*. Phys. Rev. Lett. **98**, 216402 (2007). (Cited on page **104**)

[301] A. Moreo. *Magnetic susceptibility of the two-dimensional Hubbard model*. Phys. Rev. B **48**, 3380–3382 (1993). (Cited on page **107**)

[302] M. Rossignolo, T. Reisser, A. Marshall, P. Rembold, A. Pagano, P. J. Vetter, R. S. Said, M. M. Müller, F. Motzoi, T. Calarco, F. Jelezko, and S. Montangero. *QuOCS: The quantum optimal control suite*. Comput. Phys. Commun. **291**, 108782 (2023). (Cited on page **108**)

[303] J. H. M. Jensen, J. J. Sørensen, K. Mølmer, and J. F. Sherson. *Time-optimal control of collisional* $\sqrt{\text{SWAP}}$ *gates in ultracold atomic systems*. Phys. Rev. A **100**, 052314 (2019). (Cited on page **108**)

Acknowledgments

This thesis would not have been possible without the aid of numerous people, who kept assisting and encouraging me through all these years.

First and foremost, I would like to thank Immanuel Bloch for his great supervision. I was brought into this field of research thanks to his enthusiasm. The continuous stream of novel, exciting ideas, as well as proposals from theorists he encountered, were invaluable in discovering new directions for future projects.

I am equally thankful to our lab supervisor Timon Hilker. He always found time to discuss both our daily challenges as well as new, interesting ideas in depth. His invaluable insights have proven crucial again and again in overcoming problems.

I am also grateful to Christian Gross, who supervised my first years in the Lithium lab. He helped shape my approach to any obstacles the lab might throw at us by finding reasonable, pragmatic solutions.

There is probably no one that I have spent more time with than Sarah Hirthe who I shared years in the lab with. We were always discussing fiercely and despairing together over whatever piece of equipment broke last; in the end, we always managed to figure it together. Thank you so, so much for making all the long days so enjoyable!

Joannis Koepsell, the former PhD student who taught me most of what I know about the lab. Thanks for teaching me all the intricacies of this mess of a setup and bringing enthusiasm to any task!

Thomas Chalopin, our postdoc, without whose help the upgrade to the machine would not have been possible. Thanks for all your insights and everything I learned from you!

Our former postdoc Pimonpan Sompet, who always managed to make any setup work, somehow, no matter how messed up it was initially.

Pascal Weckesser, for becoming a great friend over the last years! Thanks for managing to cheer me up, no matter how stressed I was!

A big thanks also to our perpetual theory collaborators, Fabian Grusdt and Annabelle Bohrdt as well as Henning Schlömer. Their excitement when presenting new experimental data was always encouraging! Without their valuable ideas, a lot of this would not have been possible!

Also a big thanks to the next lab generation, Petar Bojovic, Si Wang, Titus Franz and Johannes Obermeyer. Good luck with the machine, I am curious, what you will achieve in the coming years!

The great environment at MPQ is invaluable. The assistance between all the different labs is amazing as there is always someone around who might have had a similar problem. I cannot count all the numerous people over the years in all the labs who have helped me in one way or another!

Special thanks for the technical support of Anton Mayer without whose expertise I would have despaired in the planning of the new setups! I am very sorry for all my stupid questions you had to endure!

Further thanks to the rest of the support staff, Kristina Schuldt, Ildiko Kecskesi, Karsten Förster and Olivia Mödl, who were always a big help for any problems.

My friends have proven once again to be invaluable over these years. Sorry for all the times I arrived late for dinner and tired enough to just fall asleep! Thanks for sticking with me despite all this: Jonas, Henny, Keno, Jessy, Katrin, Miriam and of course all the others who supported me while I zoomed in late from the lab!

Finally, a big thanks to my family for helping me get where I am and always being a safe haven to come home to.

Thank you!